TERAHERTZ TIME-DOMAIN REFLECTOMETRY OF MULTILAYERED SYSTEMS

by

J Bianca Jackson

A dissertation submitted in partial fulfillment
of the requirements for the degree of
Doctor of Philosophy
(Applied Physics)
in The University of Michigan
2008

Doctoral Committee:

      Professor John F. Whitaker, Chair
      Emeritus Professor Gerard Mourou
      Professor Herbert G. Winful
      Professor Steven M. Yalisove
      Research Engineer Michel Menu, Research Laboratory of the French
            Museums

2008

ACKNOWLEDGEMENTS

I would like to place on record my deep sense of gratitude to Prof. Gerard Mourou for his generous guidance, help and useful suggestions that kept me inspired enough to continue this long journey and for instigating a project that actually excited my mother.

I express my sincere gratitude to Prof. John F. Whitaker for his continuous guidance, encouragement, flexibility, support and supervision going all the way back as to when I was his Research Experience for Undergraduates (REU) student in 1998.

I am extremely thankful to my fellow research group members: Jason Diebel, Matt Crites, Galen Chen and Dong-Joon Lee for lending me their ears, both personally and professionally when I needed it.

I also wish to extend my thanks to Drs. Tresa Pollack and Michel Menu, without whose support none of this work would have been possible, and Drs. Steve Yalisove and Herb Winful, for their gracious feedback.

Last, but not least, I owe a Grand Canyon of thanks to: my parents (Jay & Gwen), grandparents (Grandma Jackson, Pop-pop, & Grandma Connie), sister (Connie), as well as my niece, uncles & aunts, cousins, friends and cat (Dusty). They always believed in me, even if they didn't understand what I was doing.

TABLE OF CONTENTS

LIST OF FIGURES

LIST OF TABLES

LIST OF APPENDICES

ABSTRACT

Presented in this work are applications of terahertz pulse ranging, spectroscopy and imaging to the nondestructive evaluation of three disparate multilayer systems for the detection and measurement of hidden layers, as well as the extraction of system information that will aid in its maintenance, repair or replacement.

Thermal protection systems for turbine engine components were investigated. Thermal barrier coatings (TBC) and thermally-grown oxide (TGO) thicknesses were determined with 10 micron resolution using time-of-flight and refractive index calculations. Two alternative methods of monitoring TGO growth using reflection amplitudes and spectral shifts were proposed for the prediction of TBC failure. Laser-machined defects as narrow as 50 microns were resolved in one- and two-dimensional images.

The light and dark rings of trees, which reflect the changes in tree growth density over the course of a year, are measurable using pulsed terahertz beams. Tree-rings of bare and painted wood specimen were laterally and axially tomographically imaged in order to facilitate the dendrochronological cross-dating of artifacts. Comparisons were made between photographs and terahertz images to demonstrate the reliability of the technique.

Historically, numerous unique artworks have been lost through the act of being covered over time. Samples of paintings, drawings and mosaics were imaged beneath layers of paint and plaster using pulsed-terahertz techniques to demonstrate the efficacy of the technique for art history and restoration. Sketch materials and pigments were measured, between 0.05 and 1.0 THz, to help identify colors in spectroscopic images. Other computational and processing methods were used to optimize the distinction between color domains. Additional time-domain terahertz applications for the examination of artwork and other artifacts were proposed.

CHAPTER I: INTRODUCTION

Section 1.01 - Introduction

Nondestructive evaluation tools unite physics, applied physics and engineering in order to extract information about a material, component or a system of components that would result in its preservation, conservation, or replacement. Terahertz (THz) quasi-optical radiation—lying between the microwave and infrared (IR) bands—penetrates most non-polar, non-metallic media. Many dielectric materials that are opaque or highly scattering at optical frequencies are transparent at terahertz frequencies. THz radiation is considered non-destructive because its low photon energy is non-ionizing and molecular heating, due to absorption, is low. Therefore, it is relevant for scientists to develop THz measurement techniques in order to facilitate, qualify and quantify the nondestructive evaluation of components in ways in which other measurement techniques may not.

Over the last couple decades, means of producing and detecting sub-picosecond, broadband pulses of THz radiation have sparked many new forms of research—including time-domain terahertz spectroscopy and imaging [1,2,3]. In the reflection geometry, the transmission of at least part of the spectrum of a THz-pulse through materials of low electrical conductivity—with minimal scattering or absorption loss—and the change

in reflection of the pulses at the boundaries of different materials—due to differences in refractive indices—can be exploited to obtain spectral and spatial information about layers of materials or systems of components. This is called terahertz time-domain reflectometry (THz-TDR), which includes spectroscopy, imaging and ranging [1,4,5].

The research presented in this thesis seeks to advance the breadth of applications for the use of THz-TDR as a NDE tool by investigating disparate multilayer systems—from industrial coatings to artifacts of cultural heritage—and developing methods of extracting information about the content or conditions of the layers that will: 1) aid in assessment of the layers and lead to decision making about the preservation, restoration, or replacement of the system or 2) provide contextual knowledge about the system or other related systems.

This first chapter presents the overview of this dissertation according to the main chapter.

Section 1.02 - Scope of Thesis

A. Background

Chapter II will present background information on the principles and tools of nondestructive evaluation, general terahertz sources, sensors and applications. In addition, it will present the experimental methods of terahertz time-domain reflectometry that enable it to probe, measure and extract information about a material, a component or a system of

components. These methods were used extensively and will be relevant throughout the thesis.

Nondestructive Evaluation of Multilayered Systems
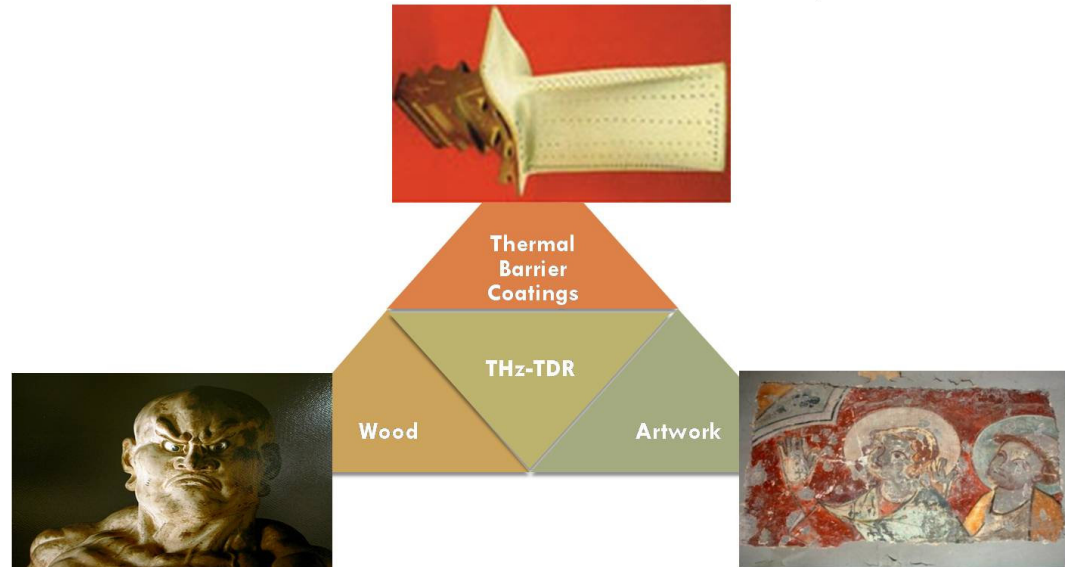
Figure I.1: **Pyramid diagram of three multilayered systems nondestructively studied using terahertz time-domain reflectometry: thermal barrier coatings, wood and paintings.**

B. THz-TDR of Thermal Barrier Coatings

Chapter III proposes using THz-pulse reflectometry as a pre-emptive NDE tool for the portable, in-field monitoring of layer thicknesses, growth and defect evolution. New metal superalloys push limits of the operational temperatures of equipment or machine components to temperatures greater than the melting points of conventional metals. As a result, multilayer thermal protection systems were developed using novel ceramic oxides—to serve as protective thermal barrier coatings (TBC)— thermally grown oxides (TGO) and intermixed, metallic bond coat (BC) layers. TBCs reduce oxidation and corrosion, thus they significantly improve component lifetimes for fuel cells, stationary power generators,

and propulsion turbine engines [6,7]. Damage or separation of the thermal protective layers can lead to premature component and system failure. Therefore inspection methods that can monitor faults before failure and predict the lifetime of a component are desirable, particularly if they are nondestructive, noninvasive, practical and cost-effective. THz-TDR was used to resolve surface defects and measure layer thicknesses, while THz-TDR measurement techniques for lifetime prediction properties are proposed.

C. THz-TDR of Wood

Chapter IV, demonstrates the feasibility of using time-domain terahertz pulse ranging and imaging in order to resolve tree-ring information—both parallel and perpendicular to ring growth, and through layers of paint—in order to facilitate the tree-ring dating of artifacts. Critical to the history of the use of wood in art and architecture is the discipline of dendrochronology, the scientific study of tree rings with respect to time. Used also by climatologists, archeologists, and others, dendrochronology is important because the patterns in which trees grow their annual rings are specific to their species, geographic provenance and environmental conditions experienced. Thus, thorough knowledge of ring patterns can result in precise calendar dating of segments of wood, and this in turn permits precision dating of art, such as wood panel paintings and architectural structures. The terahertz images will be statistically

4

compared to optical photographs in order to simulate dendrochronological crossdating methods and verify reproducibility.

D. THz-TDR of Artwork

Chapter V proposes the use of terahertz time-domain reflectometry for the evaluation of multilayer works of art and cultural artifacts, in order to contribute to their conservation and restoration. In terms of conservation, it is ideal that the method of evaluation for historical artifacts be non-destructive and non-invasive because of their uniqueness and rarity. While optical and x-ray imaging and spectroscopy are already well-established evaluation tools, they have their respective limitations that prohibit their use in reflection for thick, large and detailed multilayered artworks. Pigments and other artist's media were spectroscopically measured. The temporal delays and intensity signatures of terahertz pulses reflected from multilayer artwork were measured in order to identify and image hidden layers—including drawings, paint patterns and mosaics—through coats of paint and thick layers of plaster.

E. Conclusions

Finally, chapter VI will summarize the main results of the preceding chapters and present ideas for systematic improvements and future experiments.

CHAPTER II: BACKGROUND

Section 2.01 - Terahertz Radiation

A. The Electromagnetic Spectrum and Terahertz Radiation
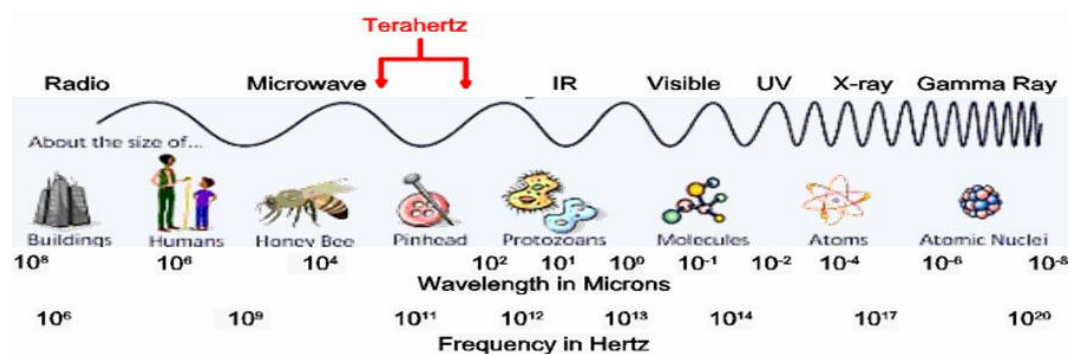
Figure II.1: The electromagnetic spectrum, with regions scaled by wavelength to common items (adapted from NASA source).

The terahertz (THz) region of the electromagnetic (EM) spectrum (Figure II.1) is possibly the least understood and most complicated. EM radiation is propagated by a sub-atomic particle called a photon—which travels at the "speed of light", 3×10^8 meters per second, and is defined by wavelength and frequency. The THz region has been arguably defined as being between 0.03 and 3 mm in wavelength, although its waves are sometimes referred to as "submillimeter." At frequencies between 0.1 and 30 trillion (10^{12}) cycles per second, the terahertz regime overlaps with both the microwave and far infrared regions of the spectrum. Since lower frequency microwave radiation has lower photon energy, the waves cannot be measured directly, only collectively by the electrical bias they

6

induce in a detector. Infrared radiation, on the other hand, is optical since its photon energy is large enough that individual photons can be measured. Thus, terahertz radiation uniquely straddles the worlds of electronics and optics.

B. A Brief History of Terahertz of Sources and Detectors

While terahertz radiation is naturally emitted by blackbody sources at temperatures between 14 and 140 Kelvin, the terahertz gap was not considered to be closed by scientists until 1923—when Hertzian oscillators made with Tungsten cylinders were first used to generate radiation between 0.8 mm and 4.8 mm and radiometer receivers were developed using platinum covered mica vanes [8,9]. However, it has only been in the last few decades that advances in ultrafast electronics and optics have enabled the development of coherent terahertz sources and detectors.

In 1964, one of the earliest man-made terahertz sources was a HCN continuous-wave (cw) laser operating at 1.12 THz [10]. In the early 1970s, tunable-cw and pulsed terahertz radiation were generated by non-linear electro-optical effects—such as frequency difference generation and optical rectification—using high power lasers [11,12]. By the mid-seventies, the Schottky diode harmonic mixer and the Auston photoconductive (PC) switch were first to utilize both optics and electronics to create terahertz signals [13,14]. The Auston switch was even more revolutionary since it used ultrafast laser pulses to generate

broadband, electrical, and free-space THz pulses. As a result, this technique of THz generation was further experimentally developed by others whose work is cornerstone to this thesis [15, 16].

Further advances in laser and semiconductor technologies spawned rapid development of additional terahertz sources in the following decades. THz-wave parametric oscillators [17,18], photonic crystals [19], and laser-induced gas filamentation [20] became new sources of terahertz radiation. Novel solid-state devices resulted in terahertz generation from resonant tunneling diodes [21], plasma-wave photomixers [22] and Bloch [23] and Zener oscillators [24]. Most recently, quantum-well cascade lasers (QCL) emitting continuous wave (cw) terahertz radiation have been developed [25]. With the recent demonstration of room temperature operation [26], THz-QCLs have the potential to take THz technology the farthest out of the laboratory.

Synchrotrons [27] and free electron lasers [28] can produce high power, coherent terahertz pulses on the order of picoseconds. Very different from the previously mentioned terahertz sources, they became prevalent with the pervasion of electron accelerator labs and storage ring facilities in the 1980s and 1990s. They are very useful with their broad tunablity, however their usage is limited by accessibility, availability and high operational cost.

The development of terahertz detectors has often mirrored the development of THz sources. The same physics that enables terahertz

generation using electro-optic crystals, photoconductive switches, or Schottky diodes, has facilitated their use as sensors. On the other hand, the use of bolometers, and other pyroelectric blackbody sensors, is possibly the oldest and most conventional method of detection [29,30]—as they have been used for measuring a significantly broader range of the electromagnetic spectrum.   However, their thermal sensitivity and response time can be less than desirable for THz applications, such as industrial time-domain imaging, where fast, portable terahertz pulse systems need to operate at room temperature.

C. A Brief Overview of Terahertz Applications

As the terahertz gap is filled, the number of THz applications constantly increases, with emphasis on spectroscopy and imaging. The breadth of fields includes astronomy, biology, chemistry, environmental science, industrial engineering, materials science, medical and pharmaceutical science, and physics.
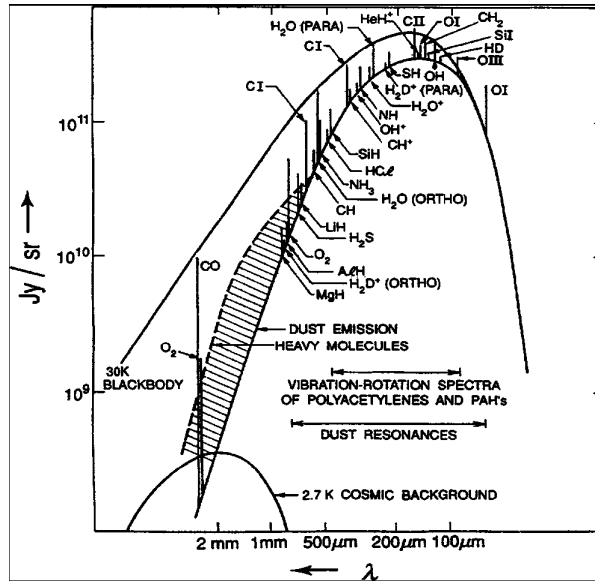
Figure II.2: Radiated energy versus wavelength showing 30 K blackbody, typical interstellar dust, and key molecular line emissions in the sub-millimeter (terahertz range) using heterodyne detection [31].

The earliest use of bolometers and heterodyne mixers was by astronomers to measure the "sub-millimeter" radiation emitted by the stars, planets and cosmic dust. Many of the same spectral signatures that are abundant in interstellar and intragalactic space are also present in planetary atmospheres. Particularly important are thermal emission lines from gases that appear in the Earth's stratosphere and upper troposphere; water, oxygen, chlorine and nitrogen compounds, etc. that serve as pointers to the abundances, distributions and reaction rates of species involved in ozone destruction, global warming, total radiation balance and pollution monitoring [31,32].
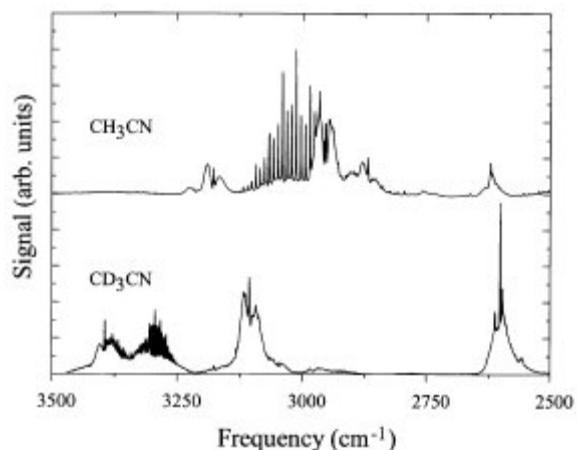
Figure II.3: Mid-infrared absorption spectra of CH3CN and CD3CN, measured with commercial FTIR spectrometer [33].

Gas sensing was an application of terahertz spectroscopy that was of early interest for industrial and homeland security monitoring. The identification of signature gases can be done in milliseconds through lookup tables once an exact determination of the spectral line frequency has been made. Also in the terahertz frequency range, many polar molecules were found to exhibit unique spectral signatures arising from transitions between rotational quantum levels [33]. Spectroscopic imaging is a two to three dimensional extension of terahertz spectroscopy. Targets composed of separated pure chemicals or a single mixture can be imaged at multiple terahertz frequencies. If absorption spectral information
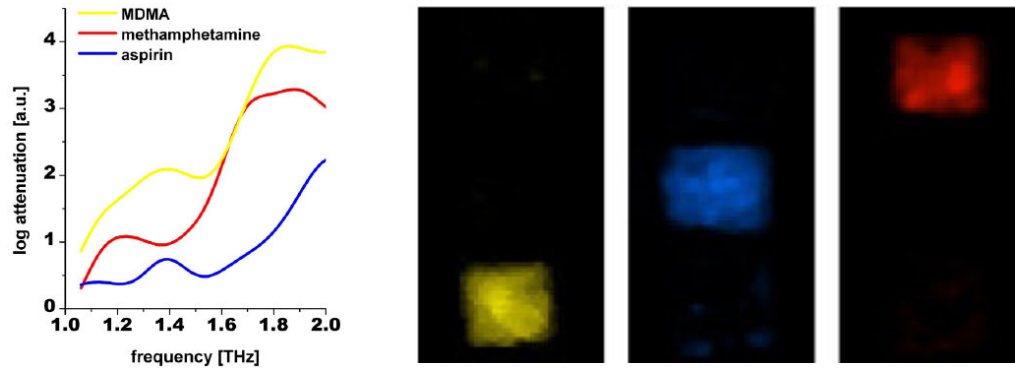
Figure II.4: (a) Absorption spectra of MDMA, methamphetamine, and aspirin; (b) Extracted spatial patterns of MDMA (yellow), aspirin (blue), and methamphetamine (red), using principal component analysis on THz images obtained using a THz wave parametric oscillator (TPO) spectrometer [34].

(Figure II.4a) for each chemical in the target under inspection is known, then the spatial patterns of each chemical as well as the components in the mixture can be extracted from the terahertz image (Figure II.4b).
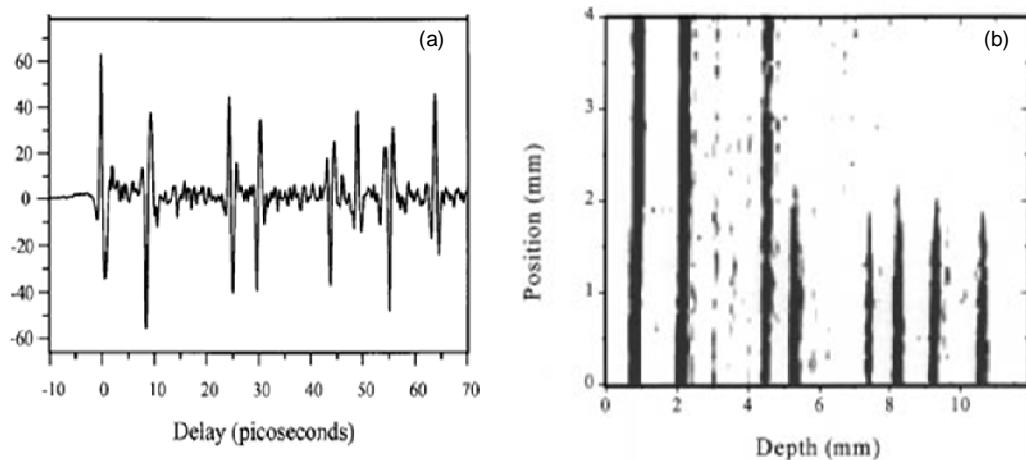
Figure II.5: (a) Terahertz waveforms reflected from a bic pen, where reflected pulses from each of the eight dielectric interfaces can be observed. (b) Terahertz tomographic image of a bic pen.

Terahertz impulse ranging and tomographic imaging were shown to have purpose in the areas of packaging and quality control [35]. Figure II.5a shows the results of a terahertz pulse propagating through a plastic pen, with portions of the pulse being reflected at the interfaces of each of the pen's components. The time window between each pulse reflection

12

and their polarity gives insight into differences in refractive index of the components. In Figure II.5b, the vertical axis of the tomographic image is parallel to the long (cylinder) axis of the pen, while the horizontal axis of the figure corresponds to depth into the pen. The terahertz pulse is incident from the left. The eight dark lines correspond to the eight dielectric interfaces (either from plastic-to-air or air-to-plastic) encountered by the pulse as it propagates through the pen. The upper right portion of the image is obscured, because these surfaces were shadowed by ink inside the inner plastic cylinder.

Section 2.02 - Nondestructive Evaluation

A. Introduction

The purpose of nondestructive evaluation is to prevent costly or destructive consequences from the failure of a material or system of components and to aid in its preservation, conservation, or replacement. It can encompass the characterization of a material, i.e. composition, electrical and optical properties, or structural characteristics. It can also involve the real-time monitoring or inspection of a system's composition or flaws during its manufacture or construction.

NDE techniques are often chosen by the quantity and quality of the data that can be extracted from a measurement, in addition to the financial cost and time required to make the measurement. Localized, or single point, measurements of components of interest can provide specific, often highly quantified details about a material or system. On the other hand,

13

large area measurements may provide fast, highly qualitative, but essential, information. Combining measurement techniques can make up for the limitations of a single method, however the ideal is a single cost-effective measurement system that is versatile and results in multiple kinds of system assessments. NDE methods that use terahertz pulses have the potential advantage of this kind of versatility.

B. Common NDE Techniques

Nondestructive evaluation techniques are generally divided into two categories, local and global [36,37]. Localized are high resolution and usually provide detailed information about a limited region of interest. They include:

Ultrasonic acoustic methods probe materials with high frequency sound waves to measure their properties and locate defects [38]. Pulses of ultrasonic energy are transmitted into the material and altered by absorption, reflection and scattering within the material and detected by transducers. Benefits of acoustic methods are fast data acquisition and excellent for crack detection. However, it requires direct contact between instrument and target, and often with an index-matching coupling fluid.

Radiography uses penetrating radiation—such as x-ray, gamma ray, neutrons, etc.—to inspect the internal structure and composition of a target by generating an image [36]. Quantitative image-processing allows for materials characterization and dimension measurement and x-ray

systems are portable. However safety issues with human operators and the lack of depth resolution can be limiting.

Infrared thermal imaging remotely senses surface temperatures and temperature gradients [37]. Materials that experience fatigue spots, imperfections, or damage may exhibit temperature gradients around the affected region, which can be measured. While this technique is noncontact and permits real time acquisition, its sensitivity to ambient room temperatures and surface emissivity variations can be problematic.

Coherence Tomography (CT) is an imaging technique utilizing a Michelson interferometer combined with a two- or three-dimensional scanner [39,40]. Light from a coherent optical source is split into two paths, a sample path and a reference path. Light in the reference path is reflected from a fixed-plane mirror, whereas light in the sample path is reflected from surface and subsurface features of the target. The reflected light from the sample path will only be detected if it travels a distance that closely matches the distance traveled by the light in the reference path; this constraint incorporates depth resolution into the technique. Thus, data can be obtained from a cross-sectional plane perpendicular or parallel to the surface of the target. CT has high dynamic range and depth resolution, however this technique is limited by material opacity and penetration-depth issues at visible and infrared wavelengths.

Computed tomography measures volume densities of materials and provides pictorial views of the internal structure of materials and fabricated

15

parts [41]. The target is translated and rotated in the path of target penetrating radiation, with transmission measurement made at each position. The data is then reconstructed into images using computer algorithms. Multiple slices through the object can be reconstructed to generate a three dimensional view of internal structure. It usually uses the same radiation sources as radiography, though it is also applicable with terahertz radiation. The spatial resolution is dependent on the wavelength of the source, therefore very detailed images are possible. However, the application is limited to circumstances in which a complete 360° target rotation is feasible.

Emissions, fluorescence and scattering spectroscopic methods measure the range of electromagnetic spectra in which a target radiates after absorbing energy from a source. The stimulating source determines the name of the type of emission: fluorescence spectroscopy uses higher energy photons—such X-rays (XRF) or UV (UVF) light—to excite a sample, while photoluminescence techniques use visible and infrared radiation. Scattering spectroscopic methods, such as Raman and elastic optical scattering spectroscopy, measure the amount of light that a substance scatters at certain wavelengths, incident angles, and polarization angles. The scattering process is much faster than the emission process. These techniques provide detailed information about target composition and local defect features, however it utilizes single spot

analysis which can ineffective for monitoring damage over significant areas.

Section 2.03 - Experimental Methods with THz-Pulses
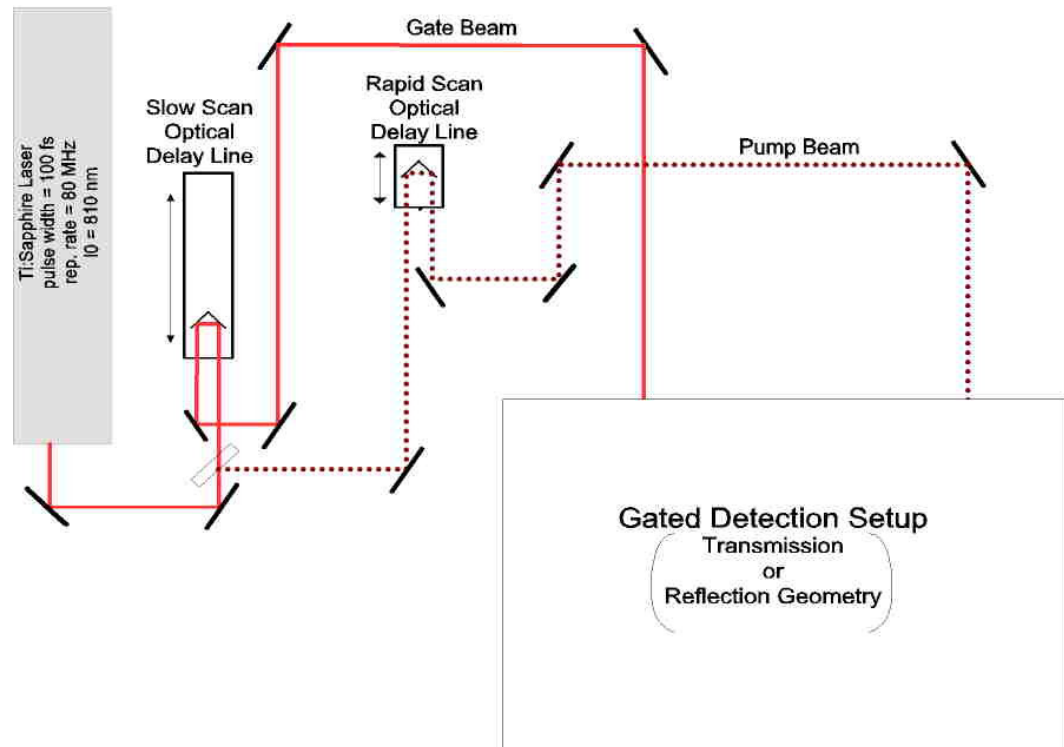
Figure II.6: Generalized terahertz generation and gated detection setup.

This section discusses the experimental methods of THz-pulse generation and detection used for the preparation of this thesis. Figure II.6 shows the generalized schematic of the time-domain terahertz pulse generation and gated-detection systems used with both free-space and fiber-coupled optical beam propagation [42,43]. The THz emitter and receiver were both photoconductive antennas and could be set up for transmission or reflection measurements. The laser source is centered about 800 nm wavelength with a 60-120 fs pulse width (6-14 nm spectral bandwidth) and an approximately 80 MHz repetition rate pulse train.

A. Terahertz Generation
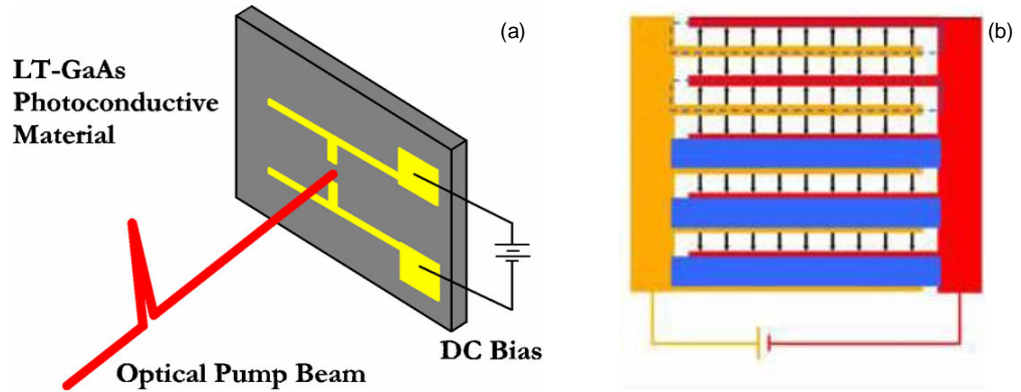
Figure II.7: **Large-aperture, biased photoconductive terahertz emitters with (a) Hertzian dipole and (b) interdigitated electrodes.**

THz-pulses were generated and then propagated through free-space using a biased, photoconductive switch antenna, (Figure II.7)—consisting of a photosensitive semi-insulating or low-temperature grown gallium arsenide (SI- or LT-GaAs) semiconductor [44] with two metalized electrodes deposited on its surface. At equilibrium, the conductivity, σ, of the semiconductor is define by its dark conductivity, σ_0:

$$\sigma_0 = e(\mu_n n_0 + \mu_p p_0) \tag{1}$$

where e is the electron charge, n_0 and p_0 are the respective intrinsic electron and hole densities, and μ_n and μ_p are their respective carrier mobilities. The antenna is illuminated at normal incidence by the ultrafast laser pulse with a photon energy above the GaAs bandgap, thus generating electron-hole pairs into the semiconductor at a rate, G(t), proportional to

$$G(t) \propto n_o e^{-(t/\delta t)^2} \tag{2}$$

where δt is the optical pulse width, and inducing a transient increase in conductivity, $\Delta\sigma(t)$, given by

$$\Delta\sigma(t) = e(\mu_n \delta n(t) + \mu_p \delta p(t)) \tag{3}$$

When the pulse duration ends, the excited photocarriers will relax and recombine or become trapped in mid-band gap states.
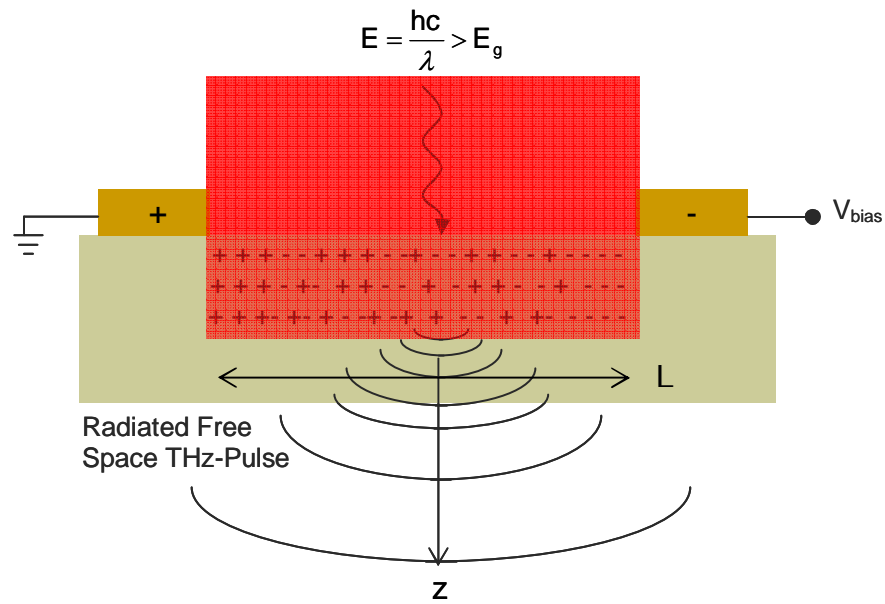
Figure II.8: **Optical generation of free-space terahertz pulse in large aperture emitter.**

According to Maxwell's equations and Hertzian-dipole theory, in the far-field ($z \gg L^2/8\lambda_c$), the free-space electromagnetic radiation emanating from such antennas as those commonly used for THz generation is proportional to the rapid change in the photocurrent within the electric field region [45,46]. Using the Drude-Lorentz model, the photocurrent is given by:

$$j = \sigma E = e(nv_e - pv_h), \tag{4}$$

where v_e and v_h are the respective electron and hole velocities. This change in photocurrent, to which the terahertz electric field is proportional, arises from two processes: 1) the rapid change in carrier density due to ultrafast photoexcitation or carrier trapping and 2) the acceleration of the photogenerated carriers in the presence of an electric field [47].

$$E_{THz} \propto \frac{dj}{dt} = e \left(\underbrace{v_e \frac{dn}{dt} - v_h \frac{dp}{dt}}_{Change\ in\ Carrier\ Density} + \underbrace{n \frac{dv_e}{dt} - p \frac{dv_h}{dt}}_{Carrier\ Acceleration} \right) \tag{5}$$

The change in carrier density is determined by the carrier population and generation rate, as well as the time it takes for the carriers to be trapped in bandgap or inter-bandgap states τ_c.

$$\frac{d(n,p)}{dt} = -\frac{(n,p)}{\tau_c} + G(t) \tag{6}$$

The accelerating (or decelerating) carriers produce a transient, radiated THz-pulse that propagates through the semiconductor (Figure II.8).

$$E_{loc}(x,t) = E_{bias} - \frac{P(x,t)}{3\varepsilon_0 \varepsilon_r} \tag{7}$$

$$\frac{dv_{e,h}}{dt} = \frac{\pm e}{m_{e,h}} E_{loc}(x,t) - \frac{v_{e,h}}{\tau_s} \tag{8}$$

After the photo-excited charge carriers separate, they produce an induced dipole moment within the bias field. The resulting space-charge distribution (due to both free and trapped carriers) serves to counter and screen E_{bias}, and the decelerating charge carriers radiate again. The THz radiation within the gap also has a transient polarization, P, that is due to the induced dipole moment and is opposite to the external bias. The E_{loc} further decelerates the photoexcited carriers drifting in the bias field and scattered by each other ($\varepsilon_0 \varepsilon_r$ is the material permittivity, $m_{e,h}$ is carrier

mass, and τ_s is the carrier momentum relaxation time). However, when the photoconductive gap is smaller than the center wavelength of the THz-pulse spectrum (L << λ_c), bias-field screening becomes less significant and carrier dynamics dominate. Therefore, carriers will be accelerated as long as the local electric field and free carrier density are not zero.

It is also interesting to note that with increasing carrier densities, n_s, the surface current within the photoconductive gap saturates,

$$j_s = \frac{A \cdot n_s(x,t) \cdot E_{loc}(x,t)}{1 + B \cdot n_s(x,t)} \tag{9}$$

where A and B are material dependent constants. Thus E_{THz} eventually saturates with higher optical fluences. However, the bias field can be increased up to the material's breakdown field strength, ($E_{BD} \sim 300$ kV/cm for GaAs), without saturating the current or E_{THz}. [45,46,48].

Two photoconductive antenna configurations were used in this thesis. The simplest is the Hertzian dipole (HD) in Figure II.7a, the dynamics of which are as described above [49]. From diffraction theory [50,51], the terahertz power scales with the square of the infrared pump power and beam spot size—if the laser beam spot size, r, is much smaller than the terahertz center wavelength—and linearly with the external bias field (by way of Equations 5 and 6).

$$P_{THz} \propto P_{NIR}{}^2 r^2 \tag{10}$$

For HD emitters, the power can be scaled up, while carrier saturation and material break down can be avoided by increasing the size of the photoconductive region. This, however, also shifts the spectral

energy of the terahertz pulse to lower frequencies. The interdigitated-finger electrode (IDF) design (Figure II.7b) minimizes this spectral shift, because the active region for a pair of electrodes is 5 μm [48,52]. Each photoconductive gap then becomes a source of a terahertz pulse. Since the polarity of the bias field alternates with each electrode pair, the net E_{THz} amplitude approaches zero when a large area of the antenna is illuminated. However, when every other gap is shielded by a metalized opaque layer, the temporally coherent electric fields become additive, thus yielding a wider-bandwidth, higher energy THz-pulse.
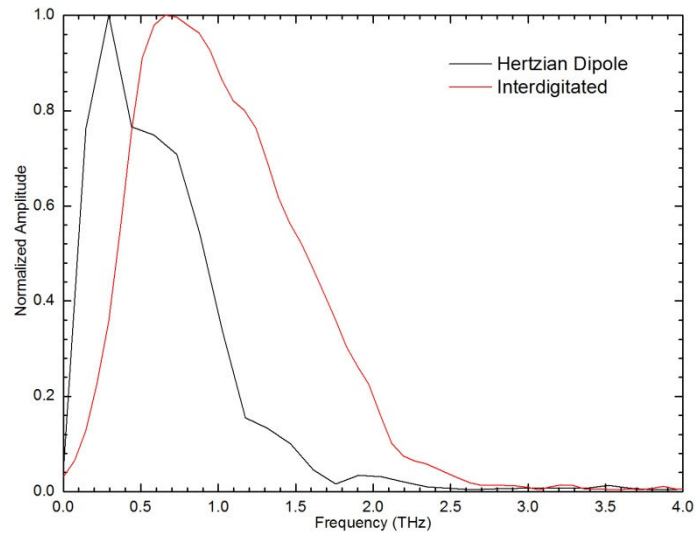
Figure II.9: Normalized comparison of Hertzian dipole and interdigitated electrode terahertz emitter spectra.

Figure II.9 compares the normalized amplitude spectra of the Hertzian dipole emitter and the interdigitated emitter used for several of the experiments presented in this thesis. Both used another Hertzian dipole antenna as a receiver. The HD emitter was limited to 80 mW average laser pump power focused into a 7 μm spot size and 25 VDC

applied bias, while the IDF antenna was excited with 250 mW average power (with a collimated spot size of approximately 300 μm) and ±5 V applied square-wave pulsed bias. The IDF has a 350 GHz blue shift of the peak frequency and a 1.8 times wider full width at half max (FWHM).

B. Terahertz Detection

PC detection utilizes a second terahertz antenna as a receiver. The gate beam generates photocarriers in the receiver by the same photoexcitation mechanism as when the pump beam does in illuminates the emitter [42,48,53]. Unlike for the emitter, the incident electric field of the THz-pulse causes a time-varying potential to develop across the receiver, thus serving as an applied voltage bias that induces a transient photocurrent, J_d, given by the convolution:

$$J_d(t) \propto \int_{-\infty}^{\infty} E_{THz}(t)n(t-\tau)dt \qquad (11)$$

where, $n(t-\tau)$ is the carrier response function of the semiconductor and is proportional to the laser pulse envelope. The shorter the carrier trapping time and narrower the laser pulse, the more accurate the measured terahertz signal will be, i.e., closer in appearance to the radiated THz-pulse. The generated photocurrent is then amplified and measured as an electrical signal using either an oscilloscope or a data acquisition board and computer.
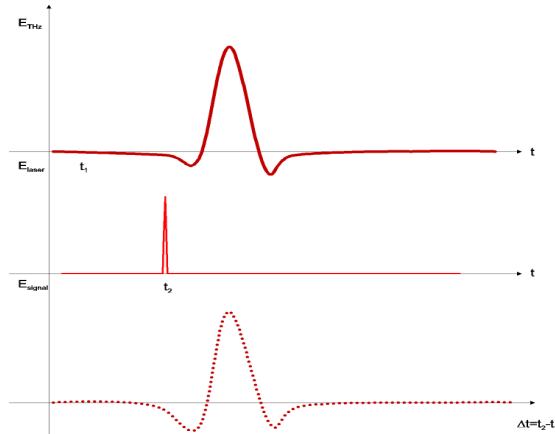
Figure II.10: Time-gated THz electric field sampling.

The use of a gated detection technique to measure the terahertz electric field compensates for the shortness short duration of the THz-pulse, which can be less than 1 ps [54]. The gating technique requires the pulsed laser beam to be split into two paths, pump and gate, as shown in Figure II.6. The THz-beam path becomes an extension of the optical pump beam path, which must be both spatially and temporally overlapped with the receiver. Both beam paths have a variable optical delay which enables the sampling of the temporal profile of the THz-pulse by changing the optical path length, $\Delta z = \Delta t \cdot c$, where z is in the direction along the optical delay path.

The peak THz electric field is measured as a voltage amplitude when the two beam path lengths are equal $\Delta z = \Delta t = 0$ at $z = z_0 \rightarrow t = t_0$.

$$E_{THz}(t_0) = E_{THz\text{-peak}} \qquad (12)$$

The laser pulse train generates identical THz-pulses approximately every 12.5 ns. Therefore, in order to obtain a THz-time signal, the path length must be changed such that the measured terahertz time signal is given by:

$$E_{signal}(t) = \sum_{-k}^{k} E_{THz}(z_j) \qquad (13)$$

for a signal centered about the peak, and where z_j is one mirror position in the optical delay path, $\delta t = c(z_k - z_{k-1})$ is the minimum temporal resolution of the time-domain electric field and $\sigma_t = c(z_k - z_{-k})$ is the temporal window of the terahertz signal.

The slow scan optical delay consists of a retro-reflective mirror mounted on a stepper motor that permits a maximum 866 ps time-signal window and minimum 6.6 fs temporal resolution. This is beneficial in time-domain spectroscopic applications where, by way of the Whittaker-Shannon sampling theorem [55], the spectral resolution δv and bandwidth σ_v are limited by $(2\sigma_t)^{-1}$ and $(2\delta t)^{-1}$, respectively. The rapid scan delay, on the other hand, is a retro-reflector oscillating up to 100 Hz, permitting a maximum 320 ps sampling window with a minimum 70 fs time resolution. This can be problematic when attempting to identify sharp spectral fingerprints of materials. However for imaging applications, this permits fast waveform data acquisition, thus enabling the acquisition of up to six thousand pixels per minute or the averaging of many waveforms to increase the signal to noise ratio of the terahertz signal.

Two terahertz systems were used with two different focal plane reflection geometries, off-axis and on-axis. For the off-axis or "pitch-catch" geometry (Figure II.11a), the optical beams propagated through free-space before exciting the terahertz antennas. The emitted terahertz beam

(TX) was collimated by a lens, focused by a parabolic mirror, and then guided to the sample plane by a flat mirror at an incidence angle between 30° and 45°. The reflected beam is subsequently guided to a collimating paraboloid and then focused onto the terahertz receiver (RX). For imaging applications with this geometry, the focal plane is rigidly fixed and the sample plane must be translated in the X, Y or Z direction.
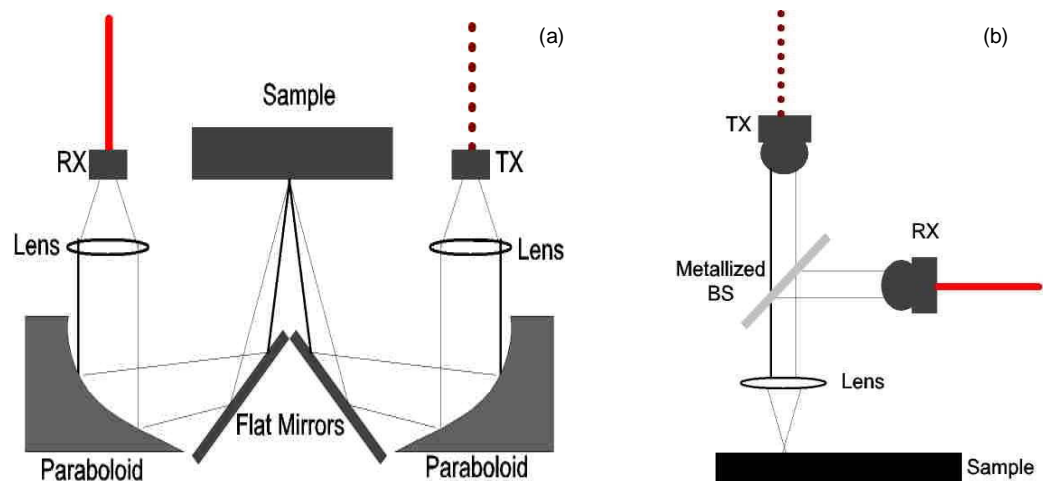
Figure II.11: (a) Off-axis, or "pitch-catch," and (b) On-axis, or "co-linear" reflection geometry terahertz generation and detection scheme.

For the on-axis or "co-linear" geometry (Figure II.11b), the optical beams are fiber-coupled to the terahertz antennas. The emitter and hyper-hemispheric silicon lens combination produces a collimated, free-space terahertz beam, which partially transmits through a metalized pellicle and is focused onto the sample plane at normal incidence. The reflected beam is partially reflected to the THz receiver, situated at 90° with respect to the THz emitter. This configuration is more flexible than the "pitch-catch" configuration because the fiber-coupled TX-RX pair can be fixed with respect to each other and translated in, out, and across the

26

sample plane. The focusing lens can also be exchanged easily without requiring system realignment. This fiber-coupled THz generation and detection system—combined with a compact optical system—contributes to the portability and scalability of this measurement technique [56].

C. Terahertz Time-Domain Applications

Of the many terahertz applications mentioned in Section 2.01, time-domain terahertz impulse ranging[57,58,59], spectroscopy [60,61,62,63] and pulse imaging [64,65,66,67] are the most valuable to the work presented in this thesis.

Terahertz impulse ranging measures the time-of-flight response of a terahertz pulse scattered by a target, or target, occurring at distinct times corresponding to the target's position to the terahertz pulse source and detector. Impulse ranging has advantages over continuous wave techniques because it enables the acquisition of multi-spectral information, in addition to, minimizing the interference of background signals by permitting the scattered electric field reflected only from the target of interest to be analyzed through temporal window selection. Figure II.12
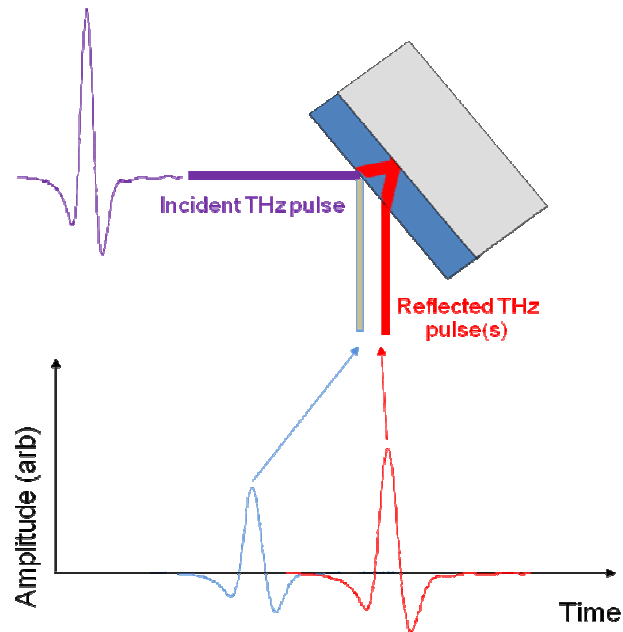
Figure II.12: Impulse ranging schematic of a terahertz pulse reflected from a multilayer system.

represents this principle, where the incident pulse (purple) is partially reflected at the surface of the target (blue) and measured at a point in time, while a partially transmitted pulse is reflected from another surface within the target (red) and is measured at a later time proportional to the distance between the two surfaces. If the pulse separation is sufficient, information about each respective surface may be resolved independently. Using Buxton's criterion [68], the axial resolution of a depth measurement is maximized if the distance between the central maxima of the main lobes of the pulses of interest is greater than or equal to the full width at half maximum (FWHM) of the narrowest pulse. This favors terahertz systems that are ultrafast and ultra-wide bandwidth.
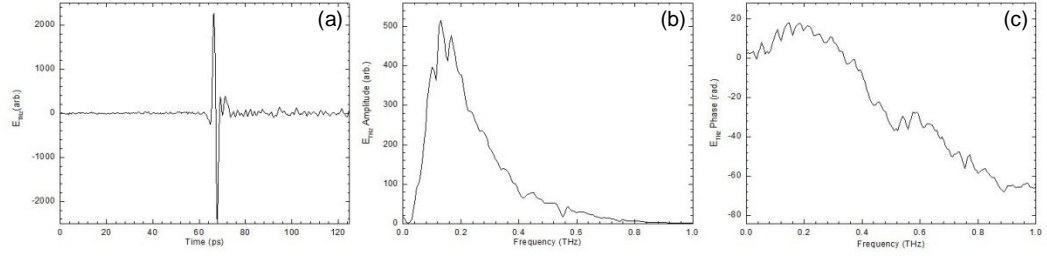
Figure II.13: Terahertz electric field (a) time-domain amplitude, (b) frequency-domain amplitude and (c) frequency domain phase.

With terahertz spectroscopy, unlike with optical measurements, the terahertz electric field is sampled in the time-domain, therefore the Fourier transform of the time-signal will produce both the amplitude and phase

$$E_{THz}(\nu) = \left|E_{THz}(\nu)\right|e^{i\phi} = \int E_{THz}(t)e^{-i2\pi\nu t}dt \qquad (14)$$

spectra of the electric field. With a single measurement, information about dielectric properties (reflectivity, transmissivity, refractive index and absorption) of the layers can be extracted from the spectroscopic information contained in the individual pulses themselves without the use of the Kramers-Kronig dispersion relations [69].

Resonance modes can be determined by sharp spectral absorption features in gases, while liquids and solids usually result in broader features. For example, water vapor has 16 sharp absorption lines (such as the one located at 0.56 THz in Figure II.13b) between 0.2 and 2.0 THz that are associated with the intramolecular rotational vibration resonance modes [70,71]. However, liquid water has broad absorption with a square root frequency dependence, in the same spectral range, which are attributed to the collective intermolecular oscillation resonance [72]. Solid

water, or ice, exhibits one-tenth the spectral absorption of liquid water with the sharp decrease occurring at the 0°C phase transition. Below freezing, its dielectric properties are instead dominated by defect-initiated molecular reorientation and are linear in the 0.2 - 2.0 THz range [73,74].

High spectral resolution is desirable for the observation of the narrow absorption resonances [75]. As mentioned in the previous section, the spectral resolution $\delta\nu$ is inversely proportional to the signal time window. In addition to the temporal window, spectral resolution is limited by the dynamic range of the terahertz signal, given by the ratio of the electric field amplitude and the probe beam noise. The dynamic range should be maximized, which can be done by increasing the THz-pulse power, using stable, current-limited laser sources and through signal averaging.

Terahertz images of objects can also be produced by acquiring many single-waveform measurements while the target area is scanned by the terahertz beam (or vice versa). The time signal, or its Fourier transform, can be computationally evaluated to construct a collection of pixels representing an image of the target. Ranging and spectroscopic techniques can be applied to produce informative series of two dimensional (2D) lateral and cross-sectional images. This includes, but is not limited to, evaluations of pulse peak amplitudes and separations, spectral energy loss and changes in phase. Multispectral image series may be produced from discrete values of the amplitude, reflectivity,

transmissivity, refractive index and absorption spectra. Special computations include field (15), amplitude (16), or power integrations (17) of either the temporal or spectral signal, E(s):

$$\int_s E(s)ds \qquad (15)$$

$$\int_s |E(s)|ds \qquad (16)$$

$$\int_s |E(s)|^2 ds \qquad (17)$$

When a reference signal $E_{ref}(s)$ is available, relative computations

$$\frac{|E(s)|}{\int_s |E(s)|\ ds} \qquad (18)$$

$$\frac{\int_s |E(s)|^2 ds}{\int_s |E_{ref}(s)|^2 ds} \qquad (19)$$

such as the power ratio (18) and relative power loss can produce revealing images. Images can also be calculated using the centroid,

$$\frac{\int_s |E(s)|^2 s\ ds}{\int_s |E(s)|^2 ds} \qquad (20)$$

which represents the weighted energy distribution of a part or whole terahertz (temporal or spectral) signal.

The spatial resolution of the acquired terahertz images is independent of the depth resolution and limited primarily by several system parameters[68,76]. The terahertz beam spot size and shape is

31

diffraction limited by the Rayleigh criterion, in the far field approximation, where the spot size is on the order of the center wavelength divided by the aperture size of the source. The signal-to-noise ratio (SNR) of the detected electric field signal is approximately given by the ratio of the signal power versus the system noise power. Data acquisition systems have limitations, such as acquisition rates, translation step size, et cetera.

Image processing and reconstruction methods can be used to improve spatial resolution in a calculated image [68,77,78]. Image math performs arithmetic computations on two or more calculated images of the same object and can be used to enhance features that may not be clear in either image. Image deconvolution divides out the spatial distribution of the terahertz beam, in order to obtain a more realistic image of the target. Fourier transform and wavelet spatial filters allow the removal of unwanted spatial frequencies from an image before it is reconstructed—low frequency filters smooth out the details and edges, while high frequency filters enhance them.

CHAPTER III: TERAHERTZ TIME-DOMAIN REFLECTOMETRY OF THERMAL BARRIER COATINGS

Section 3.01 - Background on Thermal Barrier Coatings

A. Use and Evaluation of Thermal Barrier Coatings

New metal superalloys push limits of the operational temperatures of equipment—such as turbine engine blades—to temperatures greater than the melting points of conventional metals. In turn, materials scientists have developed novel ceramic oxides—such as porous Yttria-stabilized Zirconia (YSZ)—to serve as protective thermal barrier coatings (TBC). TBCs enhance the temperature differential between the air and the alloy Thus they reduce the oxidation and corrosion of the alloy, protect the physical integrity of the turbine blade and increase the lifetime, efficiency and reliability of turbine engines [79,80,]. A typical thermal protection system (Figure III.1) consists of at least three layers: 1) a superalloy substrate, 2) an aluminum-containing bond coat (BC) with a zone intermixed with the alloy and 3) the TBC. With the exposure of the bond coat to heat, a thermally-grown oxide (TGO) layer —typically alumina—develops between the bond coat and TBC.
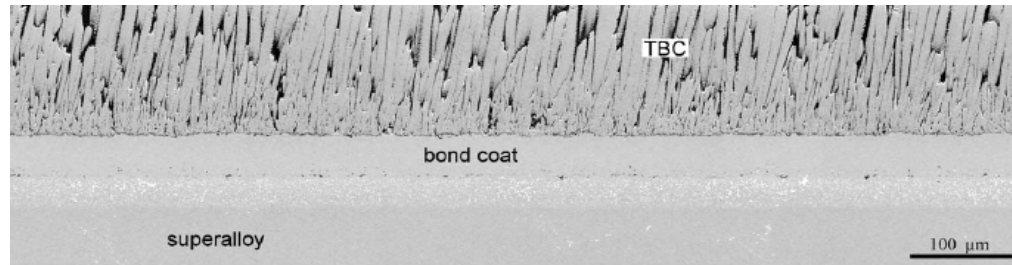
Figure III.1: Scanning electron micrograph of multilayered system consisting of superalloy substrate, a bond coat (with a zone intermixed with alloy), and a TBC layer.

There are two primary methods for thermal-barrier-coating deposition: electron beam physical vapor deposition (EBPVD) and air plasma spray (APS). These deposition techniques have been optimized to reduce strain and prevent delamination [81]. Because the thermal barrier coatings made by these two techniques differ somewhat in their microstructure, morphology—EBPVD coatings are columnar in structure, while APS coatings have a splat structure—and temperature dependent properties, different physical failure mechanisms apply [82].

However, it has been determined that any non-mechanical cause of failure of the thermal barrier coating during use is dominated by the thermal oxide growth induced by heating. The thickness of the TGO is known to increase as a function of time at operating temperature (i.e., number of thermal cycles) for both EBPVD and APS TBCs. The greater thickness of the TGO layer has been shown to increase stress levels at the TBC/bond coat interface to such levels that eventual spallation occurs. This stress is relieved by a "rumpling" or "rippling" of the TGO, which has been related to failure. Subsurface defects, such as cracks, within the TBC layer are also of concern as they can also lead to coating failure [81-

83]. Oxidation-related phenomena and failure mechanisms need to be studied individually because the behavior of the thermal protection system is dependent on growth conditions, with critical thicknesses being determined by the system preparation [84].

When TBC coated components are examined following field service, it would be desirable to evaluate the condition of the coating to determine whether it can be reliably used until the next inspection. It has been suggested that a life prediction methodology can be employed with the non-destructive measurement of three critical TBC properties: initial bond coat surface geometry, TGO stress, and TGO thickness [85]. NDE techniques used to evaluate one or more of these properties for damage assessment and lifetime determination of thermal barrier coatings include: "dry" impedance spectroscopy [86], electrochemical impedance spectroscopy [87], and electronically-induced acoustic emission [88]—which produce satisfactory results but require physical contact with the thermal protection system.
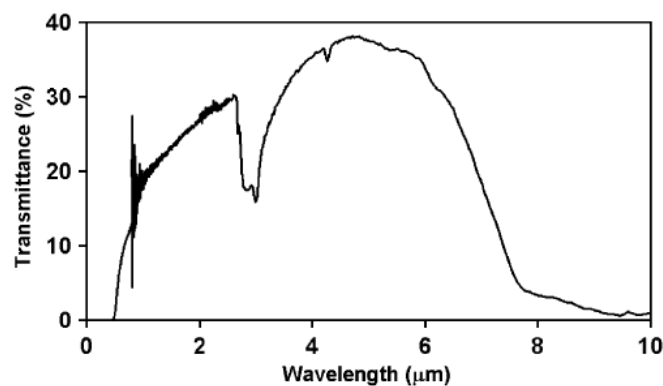
Figure III.2: Transmittance spectrum of freestanding APS YSZ coating in the visible through mid-infrared range obtained using Fourier transform spectroscopy [89].

Several optical NDE techniques take advantage of the limited transmission of visible and infrared light through ceramic coatings (Figure III.2) [89]. Infrared thermal imaging [90,91], optical coherence tomography (OCT), elastic optical scattering and photoluminescence piezospectroscopy (PLPS) [92, 93] are four of the most promising non-destructive and non-contact optical methods for coating diagnostics. For the infrared thermal imaging method, continuous wave or pulsed mid-infrared heating sources are placed on the TBC side of the target sample to stimulate the bond coat and TGO layers. The resulting back reflectance is captured by an IR camera with a 3 μm - 5 μm band pass and correlations were made between crack progressions, pre-spallation conditions and the intensity of the IR back reflectance affected by subtle changes in heat flow.

For OCT, coherent IR light is split into two paths, a sample path and a reference path. The reference path light is reflected from a fixed-plane mirror, whereas sample path light is reflected from the surface and subsurface features of the target. The depth of features can be resolved because the reflected light from the sample path will only be detected if its reflected path length closely matches that of the reference. Data can be obtained from a cross-sectional plane perpendicular or parallel to the surface of the sample.

PLPS uses an Argon cw-laser at 514 nm to excite the Chromium (III) impurity in the TGO layer. There is a distinct transition doublet that

occurs when the TGO is stress-free. However as the TGO increases in thickness, the doublet broadens and shifts proportionally to the stress gradient. PLPS shows a linear change in the peak shift with thermal cycling, which varies depending on the thermal protection system but is consistent with the damage mechanism.

Despite the transparency of TBCs in the near- and mid-infrared range, penetration depth are limited to less than 300 μm depending on the growth conditions of the coatings. Terahertz time-domain reflectometry is a potential method for non-destructively inspecting the condition of these oxide coatings, because TBCs are less absorbing in the far-infrared. Time-of-flight measurements can reveal changes in TBC and TGO layer thicknesses. Pulse imaging can reveal surface and subsurface film defects. In addition, similarly to photoluminescence measurements, spectroscopic information reveals spectral shifts with increasing oxidation, which may pre-indicate thermal protection system failure.

B. Historical Terahertz Experiments with Yttria-stablized Zirconia and Alumina

Preliminary transmission measurements were performed in the 1990's on free standing YSZ. In unpublished research, Frank Gao and John Whitaker determined that single crystal YSZ was moderately lossy below one THz and had an index of refraction of approximately 5.2 (Figure III.3).
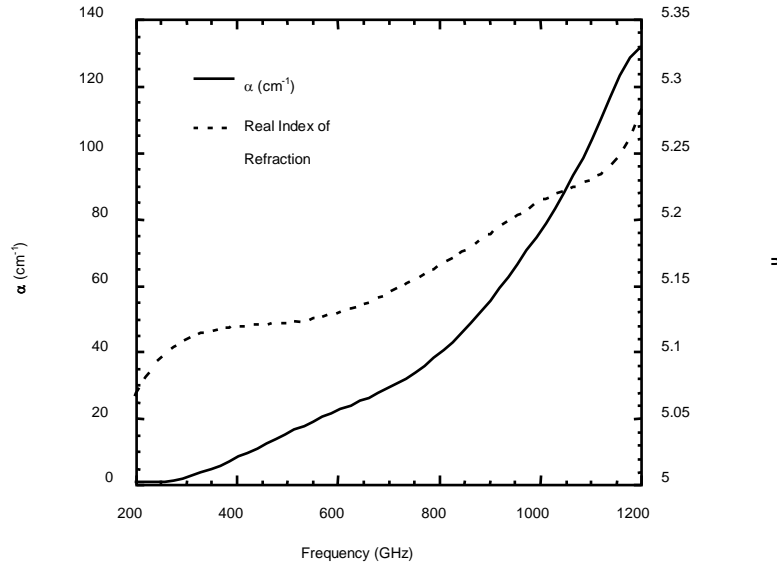
Figure III.3: **Absorption and refractive index spectra of single crystal yttria-stablized zirconia.**
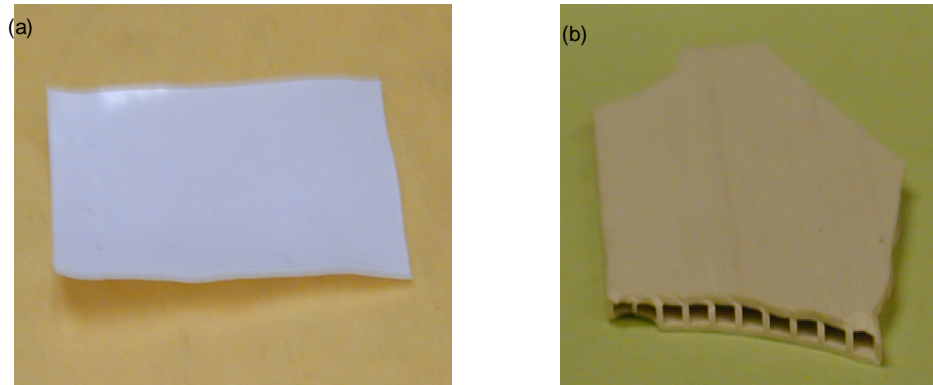
Figure III.4: Photographs of (a) polycrystalline YSZ film and (b) columnar, porous YSZ wafer.

However, transmission measurements performed by the author on free standing, polycrystalline YSZ film (Figure III.4a) and a columnar, porous YSZ wafer (Figure III.4b) revealed estimated bulk refractive indices of about 4.7 and 4.0, respectively, based on the transmission optical delay (Figure III.5) and given by:

$$n_{bulk} = n_{air} + \frac{c}{d}\Delta t \qquad (21)$$

where n_{air} is the refractive index of air, c is the speed of light, d is the thickness of the YSZ and Δt is the time delay of the YSZ with respect to air.
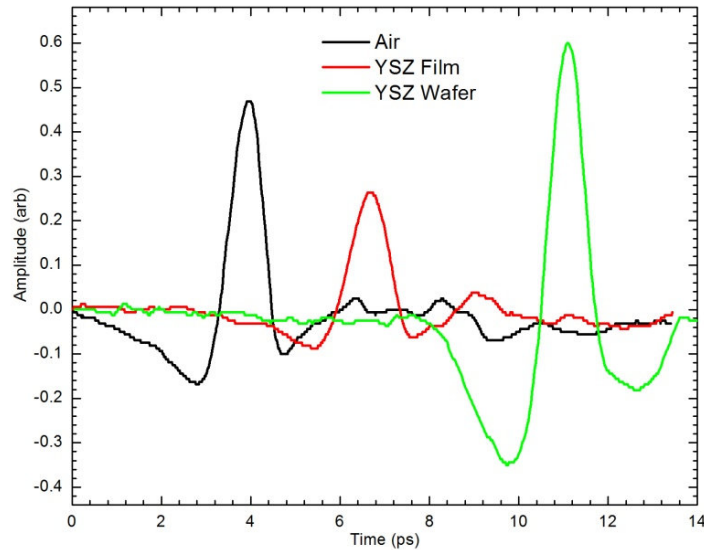
Figure III.5: Time-domain transmission waveforms through the polycrystalline YSZ film and porous YSZ wafer with respect to a reference through air.
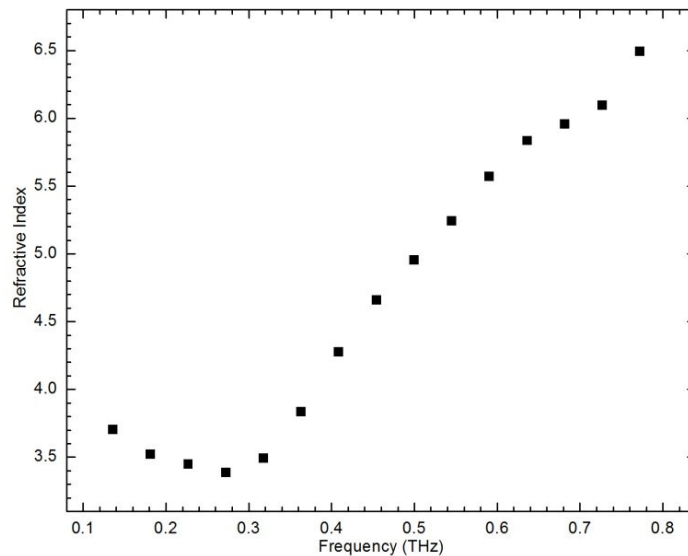
Figure III.6: Frequency-resolved index of refraction of polycrystalline YSZ film.

The real part of the refractive index spectra of the polycrystalline YSZ, $n_{YSZ}(\nu)$, in Figure III.6 is strongly frequency-dependent and determined by:

$$T(v) = \frac{E_{YSZ}(v)}{E_{air}(v)} = \frac{2n_{YSZ}(v)}{n_{air} + n_{YSZ}(v)} \tag{22}$$

$$n_{YSZ}(v) = \frac{n_{air}T(v)}{2 - T(v)} \tag{23}$$

where, $E_{YSZ}(v)$ and $E_{air}(v)$ are the amplitude spectra of the signals transmitted through YSZ and air, respectively and $T(v)$ is the transmission spectra of the YSZ. Thus, these results suggest that the index of the material is significantly dependent on the growth technique and molecular structure.

Terahertz measurements of alumina were previously published by Bolivar *et al* [94] and Rutz *et al* [95], estimating the frequency-resolved index of refraction of alumina to be between 3.07 and 3.15 below 2 THz.
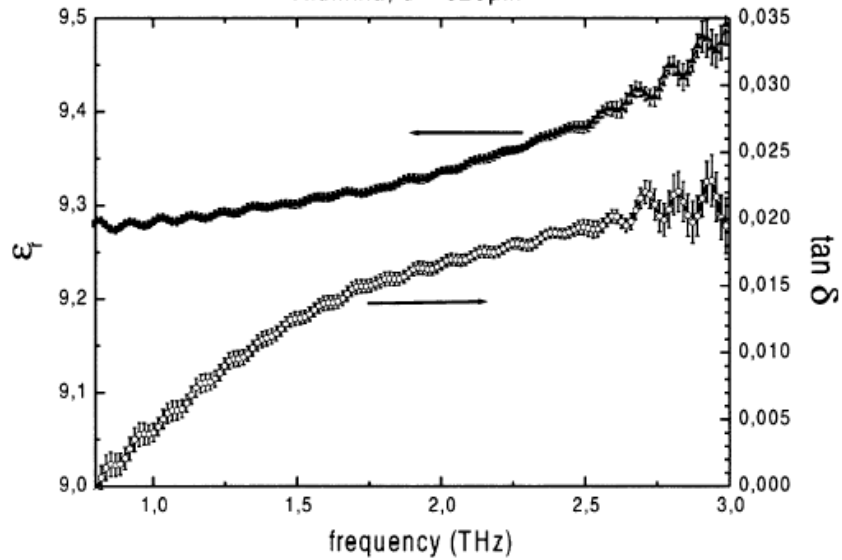
Figure III.7: Average and standard deviation of the real part of the dielectric constant and loss tangent for an alumina sample [94].

C. Description of YSZ Thermal Barrier Coating Samples

Depending on their respective sources, there were varying degrees of knowledge about the preparation of the YSZ samples studied herein. The first set of samples were obtained from the Howmet Corporation and consisted of three samples of YSZ films electron beam physical vapor deposited onto grit-blasted, Ni-based, single-crystal superalloy substrates with (Ni,Pt)Al bond coats—as designated by the commercial manufacturer Howmet Research Corporation [96]. The first three EBPVD samples were received as-deposited and were grown simultaneously in chamber with the YSZ film thicknesses empirically estimated to be 127, 178, and 229 micron.

The second set of thermal barrier coating samples was air plasma-sprayed YSZ on grit-blasted, Ni-based single-crystal superalloy coupon, also obtained from the University of California-Santa Barbara. Nothing else is known for certain about this sample, such as the bond coat material or preparation, the oxidation state, or thickness. The sample was yellow in color, unlike the white-grey-beige color of the EBPVD YSZ films. This suggests two possibilities: 1) that either their deposition (environment) conditions can affect the color, or 2) that the sample had been oxidized previously—as yellowing could be a mild side effect of the introduction of impurities during the combustion of air in the cycling oven.

The third set of thermal barrier coatings were plasma-sprayed YSZ onto grit-blasted Ni-based Hastelloy X coupons. They were commercially-

produced and laser-machined by Mound Laser & Photonics Center (MLPC), as seen in Figure III.19. The TBC film thicknesses were 293 ± 12 μm for sample (a) and 337 ± 6 μm for sample (b). These samples were not oxidized.
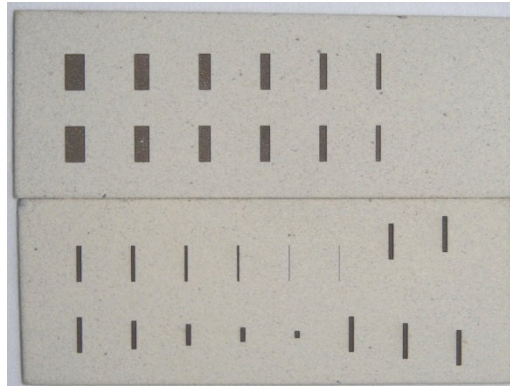
Figure III.8:   Optical photograph of two laser machined APS thermal barrier coatings.

Section 3.02 - Time-Domain Reflection Measurement of TBC Films

A. As-Grown Thermal Barrier Coatings
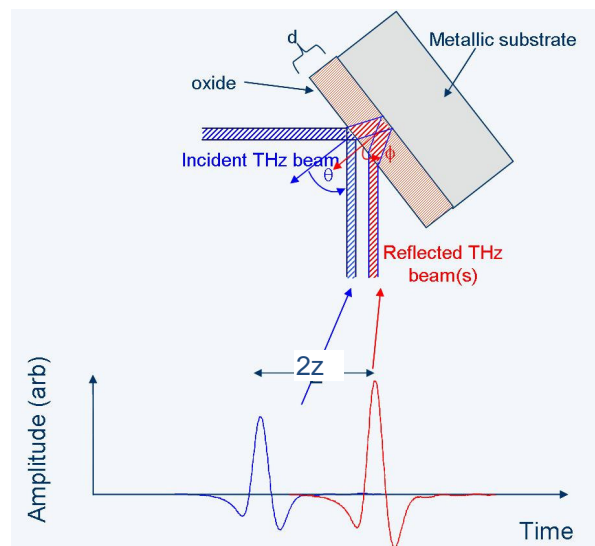
Figure III.9: Schematic of reflection measurement of film thickness.

All of the TBC Yttria-stablilized Zirconia films were measured using the off-axis, "pitch-catch" time-domain reflectometer described in Section 2.03B. The terahertz beam was focused onto the surface of the sample at a 30 - 45° incidence angle θ from the normal (Figure III.9). A fraction of the terahertz pulse is reflected at the interface between the air and YSZ coating with an amplitude proportional to the Fresnel coefficient r:

$$R(\nu) = \frac{E_{YSZ}(\nu)}{E_{air}(\nu)} = \frac{\tilde{n}_{YSZ}(\nu)\cos\phi - n_{air}\cos\theta}{\tilde{n}_{YSZ}(\nu)\cos\phi + n_{air}\cos\theta} \qquad (24)$$

where, n_{air} and n_{YSZ} are the refractive indices of porous YSZ and air, respectively, and ϕ is determined by Snell's law:

$$\phi = \sin^{-1}\left(\frac{n_{air}}{n_{YSZ}}\sin\theta\right) \qquad (25)$$

The rest of the THz-pulse propagates through the film a distance given by

$$z = \frac{d}{\cos\phi} = \frac{c}{n}\frac{t_2 - t_1}{2} \qquad (26)$$

where d is the YSZ film thickness and t_1 and t_2 are the peak times.
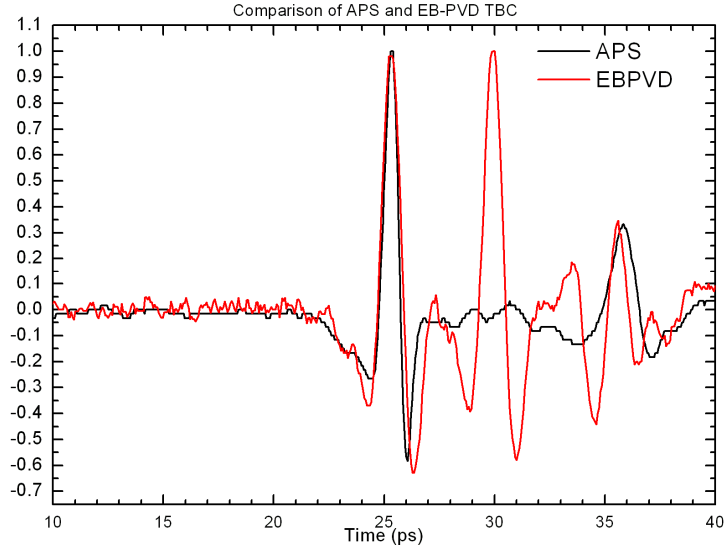
Figure III.10: Time-domain comparison of reflections from EBPVD and APS TBCs.

For as-grown TBC, the THz-pulse is reflected at the interface between the YSZ and the metallic bond coat. It is at this interface where the first differences between film preparation techniques become apparent. Figure III.10 shows a comparison of the time-domain reflections from APS and EBPVD coatings. The signals were normalized for a first peak amplitude of unity. The first pulse shapes are nearly identical, indicating neither film is more dispersive or absorbing (i.e., $\alpha_{APS} = \alpha_{EBPVD}$) than the other. However, the amplitudes of the 2nd reflections are significantly different. If the difference in amplitude were dependent on the film thickness or absorption, then the peak amplitudes would be linearly proportional to the time delay between reflections, since:

$$\frac{\log\left(\frac{I_{APS/BC}}{I_0}\right)}{\log\left(\frac{I_{EBPVD/BC}}{I_0}\right)} = \frac{\alpha_{APS}}{\alpha_{EBPVD}} \frac{\Delta t_{APS}}{\Delta t_{EBPVD}} \qquad (27)$$

44

therefore, the second peak amplitude would be expected to be closer to 45 - 50% of the first peak amplitude, instead of 30%. For reasons that will be elaborated on in Section 3.02B, it is plausible that this additional decrease in amplitude is related to one of two things: 1) scattering due the surface roughness of the grit-blasted bond coat or 2) the development of a thermally grown oxide layer—which has a lower reflectivity than the metal bond coat. Subsequent measurement of the MLPG APS thermal barrier coatings—which are also grit-blasted and have not been oxidized—and the diminished number of echoes to due internal reflection indicate that it is scattering that causes the reduced second peak amplitude.
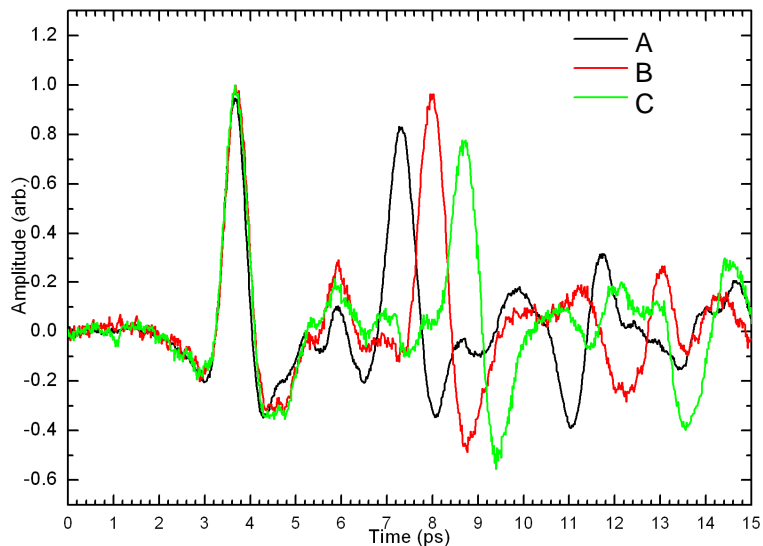
Figure III.11: Time-domain comparison of reflections from three EBPVD samples of different thickness.

For these coatings, thickness uniformity is an important parameter because temperature drop across the coating is dependent upon the thickness, especially if the thermal conductivity is uniform. The three

45

EBPVD coupons (called A, B, and C) estimated to be 127 μm, 178 μm and 229 μm thick, respectively, were also measured without knowing the refractive index of porous YSZ. The time delays between the first and second reflections (Table III.1) were determined to not be proportional to the thicknesses empirically determined by their position in the growth chamber.

Coupon A	Δt Stats (ps)	d Stats (micron)
Mean	3.6	136.4
Median	3.6	137.0
Standard Deviation	0.1	4.7
Coupon B	**Δt Stats (ps)**	**d Stats (micron)**
Mean	4.2	160.9
Median	4.3	163.1
Standard Deviation	0.1	5.0
Coupon C	**Δt Stats (ps)**	**d Stats (micron)**
Mean	4.9	186.2
Median	5.0	188.5
Standard Deviation	0.2	7.5

Table III.1: Statistical table of the average time delay between first and second reflections and the calculated thicknesses based on the determined refractive index of YSZ.
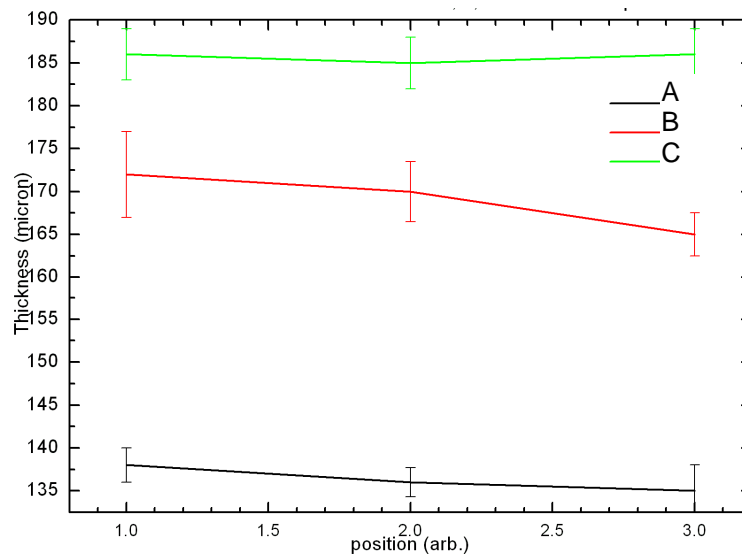
Figure III.12: Visual cross-sectional measurements of EBPVD YSZ thermal barrier coating.

The actual thicknesses of the films had to be verified by cutting the samples in half and visually measuring the cross-section (Figure III.12). coupons A and B were determined to have an average thickness within error of the estimation; however coupon C was determined to be 50 microns thinner than expected. It was also determined that the films were not uniformly thick across the samples, thus making it difficult to generalize refractive index calculations without knowing the precise thickness of the film at the time-domain measurement location.
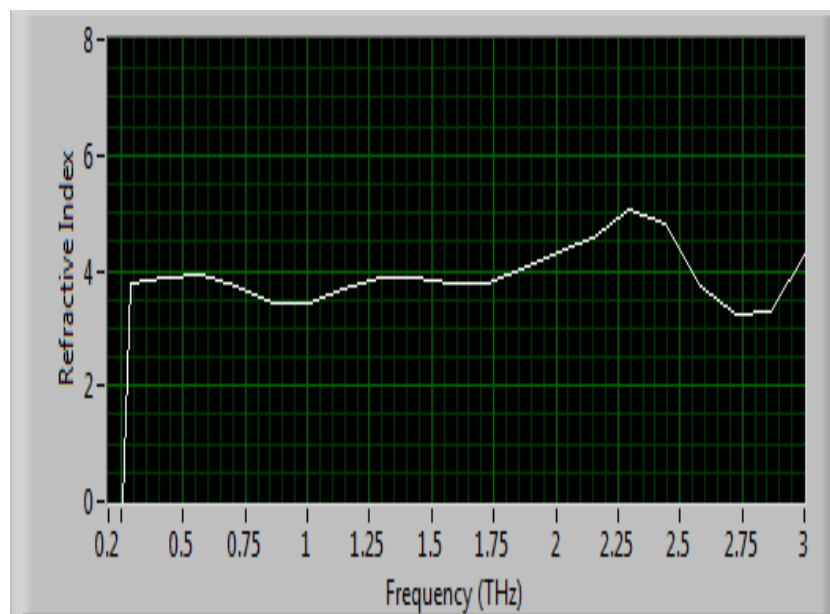
Figure III.13: Refractive index spectrum of APS YSZ thermal barrier coating.

The MLPG TBC samples had thicknesses and enough separation between the first and second reflections to permit the calculation of the index spectra of the APS-type YSZ by inverting Equation 21. Below 1.75 THz, the index is close to four, which corresponds to the index obtained for the YSZ wafer in Section 3.01B.

B. Oxidized Thermal Barrier Coatings

Since thermal oxide growth is the predominant non-mechanical source of TBC failure, coupons B and C were heated at 1100 degrees Celsius for two and three 100 hour-cycles, respectively, in order to grow TGO layers and was measured using scanning electron microscopy, to access thickness (Figure III.14b), and time-domain reflectometry (Figure III.15) after each heat .cycle.
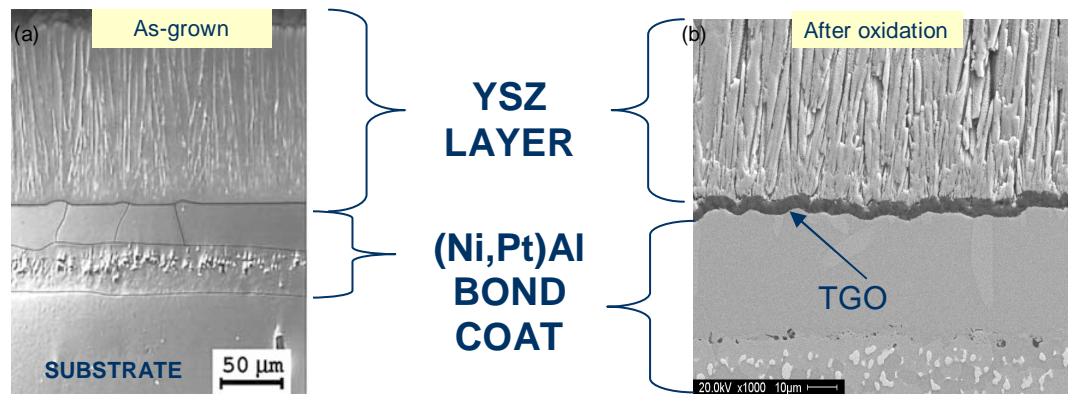
Figure III.14: Scanning electron micrograph of thermal protection system (a) as-grown and (b) after 300 hrs of cyclic heating.
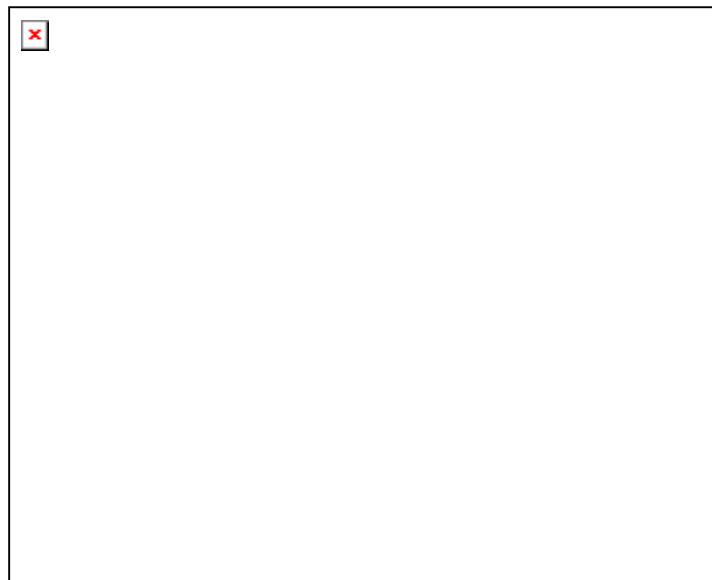
Figure III.15: Time-domain comparison of TBC coupon C as-grown and after three oxidation cycles.

The time delay between the air/YSZ and YSZ/BC or YSZ/TGO interface reflections were measured at three different positions on the sample to compensate for imprecise knowledge of the film thickness and the evolving shape of the sample after sections were cut for visual and cross-sectional SEM measurements. The peak time delays after each oxidation cycle are in Figure III.16. The SEM measurement of the TGO after a total of 300 hours of heat treatment indicated it was 4.1 ± 0.6 μm. Using 3.1 as the refractive index of alumina, that thickness would correspond to a delay time of 84 fs—which is within the thickness error of approximately 100 fs. Therefore the minimum measurable thickness, with the sensitivity of this THz system, would be approximately 5 μm.
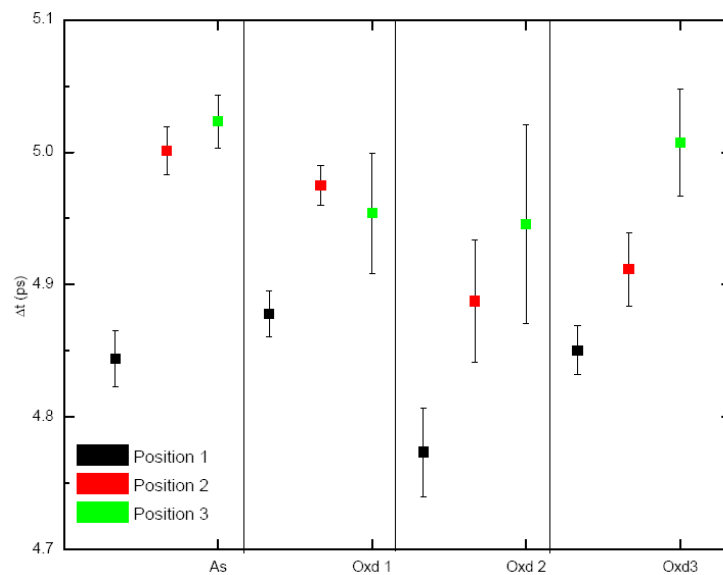
Figure III.16: Average time delay between first two reflections for TBC Coupon C as-grown and after three oxidation cycles, at different positions on sample.
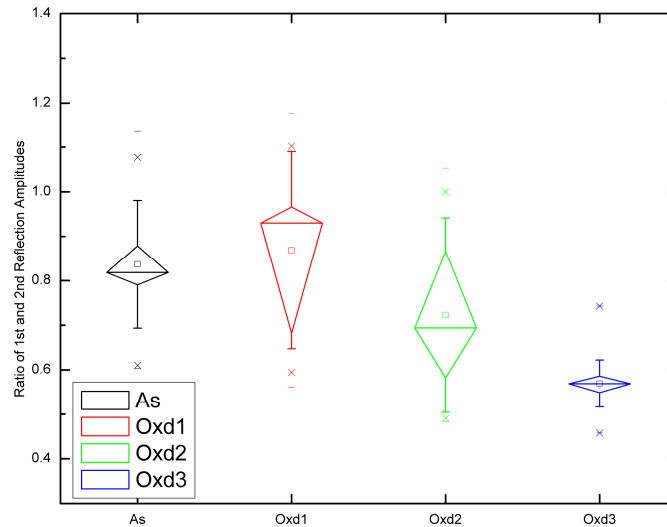
Figure III.17: Ratio of first and second reflection peak amplitudes for TBC coupon C, as-grown and after three oxidation cycles The diamond shape corresponds to the standard deviation, while the crosses are the outlying values.

An alternate method of monitoring TGO layer growth may be by comparing the relative amplitudes of the first and second reflections the for each oxidation cycle (Figure III.17). With increasing oxidation, the second peak amplitude becomes increasingly, and consistently, smaller than the first. This is related to the thickening of the thermally-grown alumina layer, which has a lower refractive index than the bond coat. At an index of approximately three, the thickness of the TGO is not significant enough for the superimposed reflected pulse to be resolved separately from the pulse reflected from the BC, while in addition to its smaller reflectivity. As the TGO becomes thicker, the amplitude of the composite pulse decreases (and the time delay increases) as the additive pulses gradually become further apart. With further oxidation then, it may be

possible to estimate TGO thickness and identify localized spallation with this method.

Section 3.03 - Profiling/Imaging of Films and Defects
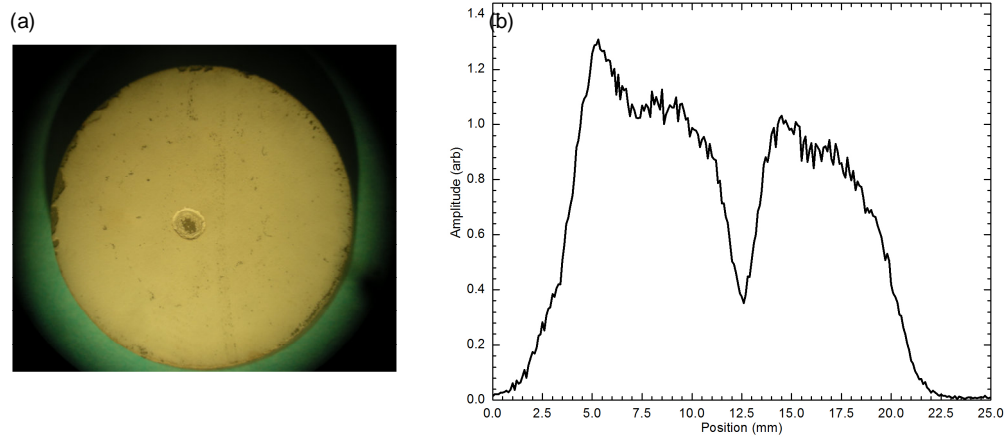
Figure III.18:   (a) Photographic image of laser-ablated EBPVD thermal barrier coating and (b) its cross-sectional profile between 1.25 and 2.0 THz.

Large-scale changes of TBC thicknesses may be measured by scanning across the sample and analyzing the reflected time-domain signal in real-time.   Figure III.18 shows a TBC with a 1.7 mm laser-damage spot which was measured using the "pitch-catch" reflectometer described in section 2.03B.   The sample was translated in 100 μm increments across the focal plane of an approximately 1.7 mm FWHM terahertz beam spot.   The spatial profile of the coating was calculated by integrating the spectrum of the air/TBC interface reflection between 1.25 and 2.0 THz.

$$\int_{\in\nu} \left| F\{E(t)\big|_{t_a}^{t_b}\} \right|^2 d\nu \tag{28}$$

This method of analysis can be beneficial when the THz-beam spot size is larger than the features of the film defect such that the local averaging of the reflected signal does not result in a detectable or significant time delay between air/TBC and air/BC reflections. By filtering out the lower spatial frequencies of the THz-beam spot, smaller spatial features can be resolved.
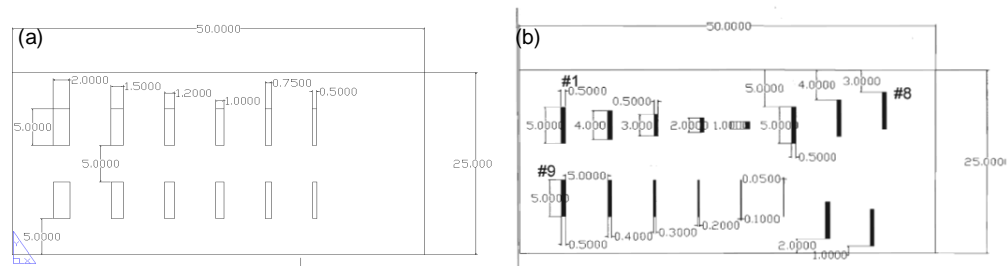
Figure III.19: Computer-assisted drawings of MLPG YSZ samples; (a) twelve laser-machined slots of equal depth and length, but decreasing width and (b) top row, laser-machined slots of equal depth and width, but varying length; bottom row, slots of equal length, but varying width and depth.

Figure III.19 shows the computer-assisted drawings of slots laser-machined into a 330 μm thick APS thermal barrier coatings. The line profile of three slots, measured using the reflectometer mentioned above, were also calculated by integrating the time window of the terahertz signal containing only the reflections from the air/TBC interface over the higher spatial frequencies between 1.25 and 2.5 THz. The peaks in Figure III.20a correspond to the slots, since the reflection from the air/BC interface was not included in the computation. The differences in the slot widths were not resolvable because the spatial distribution of the THz beam was comparable to the sizes of the features.

52
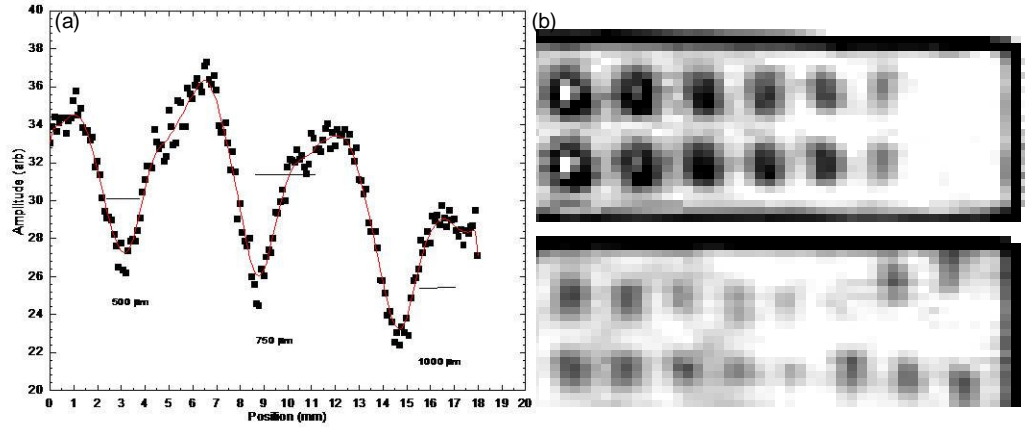
Figure III.20: (a) Cross-sectional profile of first three laser-machined slots in third row of TBC sample and (b) 2D terahertz image of all laser-machined slots (100 μm x 1000μm pixel size).

Both APS TBC samples were measured using a co-linear THz reflectometer (as discussed in section 2.03B). Figure III.20b shows a terahertz image produced by integrating the spectrum of the first reflection from 0.7 – 1.0 THz. This THz system had a smaller THz bandwidth and approximately 2 mm FWHM focal spot size. The light regions in the image correspond to areas covered by the TBC, while the dark regions correspond to the slots whose reflections were slightly out of the analyzed temporal window. The brightest white spots within the slots correspond to regions where most of the THz spot was completely within the BC exposed region. While the widths of the slots were not spatially resolved sharply, all of the slots (as narrow as 50μm) were identifiable.
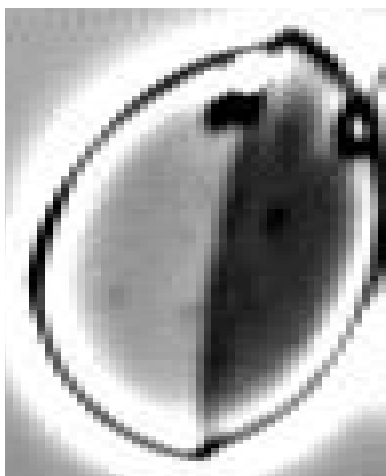
Figure III.21: Terahertz image 175 micron thick EBPVD thermal barrier coatings as-grown and after two oxidation cycles, using frequency centroid calculation (250 μm x 250 μm) pixel size.

Another plausible application of THz imaging for thermal barrier coatings, based on the principles of piezospectroscopy, is the monitoring of large-scale thermal oxide growth through a spectral shift that occurs proportionally to TGO thickness [92]. As the thermal oxide grows the stress between the thermal barrier coating and the bond coat increases, resulting in a shift in the spectrum—of the pulse reflected from the bond coat—to a lower spectral energy. For a fully calibrated terahertz system, it should be possible to monitor this energy redistribution by calculating the spectral centroid of the thermal protection system. Figure III.21 shows a terahertz image of two halves of coupon B, created using a frequency centroid calculation:

$$\nu_c = \frac{\int_{\Delta\nu} |E(\nu)|^2 \nu d\nu}{\int_{\Delta\nu} |E(\nu)|^2 d\nu} \tag{29}$$

where ν_c is the weighted peak frequency of the reflected signal. The left half of coupon B was as-grown, while the right half underwent two 100-hr

heat treatment cycles. The light grey regions of the coupon correspond to a higher spectral energy distribution, while darker grey regions correspond to a down shift. The white and black regions are artifacts due to the terahertz beam spot size and beam diffraction occurring at the edges of the sample. Another, independent measurement would have to be performed to determine if the localized dark spots are a result of coating spallation. As with the other techniques for measuring oxidation, this needs to be further evaluated after many more cycles.

Section 3.04 - Conclusion

Using terahertz time-domain reflectometry to nondestructively study multilayered thermal protection systems is novel and still under development. Inroads have been made by determining the refractive index of porous YSZ and by comparing the effects the EBPVD and APS growth techniques have on the terahertz measurements. Three methods of monitoring thermal oxide growth have been proposed, but need to be explored after further sample oxidation. Terahertz ranging was used to determine the thicknesses of TBCs, which were within 10 μm of the thicknesses determined using destructive methods. Changes in relative reflectivity and spectral energy shifts may also be used to monitor thermal oxide growth, with imaging techniques permitting large-area assessments of these conditions.

CHAPTER IV: TERAHERTZ TIME-DOMAIN REFLECTOMETRY OF WOOD FOR DENDROCHRONOLOGY

Section 4.01 - Introduction to Dendrochronology

Dendrochronology is the science of using tree-rings to create a time line for an object or place [97,98,99]. Trees are an excellent tool for dating because as a reflection of their environment, they are sensitive to both natural (i.e., weather) and man-made (i.e., pollution) events that affect tree growth. The volume and density of wood growth is not only dependent on the cyclic seasonal changes that produce earlywood and latewood (i.e., the light and dark rings as seen in Figure IV.1) in all trees, but also on localized climate, soil, and water conditions [100]. This results in the growth of tree-rings unique to a specific period of time and place, so that these patterns of wide and narrow ring growth accumulate over the years during the lifetime of the tree. Therefore trees growing in the same forest can be dated to each other (i.e., cross-dating) by comparing similar ring patterns. Sequences of the unique ring patterns, or series, can be combined into a reference chronology for any particular location, such that any tree-ring sample from that region can be compared to the reference and dated. Climate patterns—while seasonally cyclic—can progress both linearly and nonlinearly over extended periods of time [100]. Therefore, the longer the ring series is, the more precise the chronology.
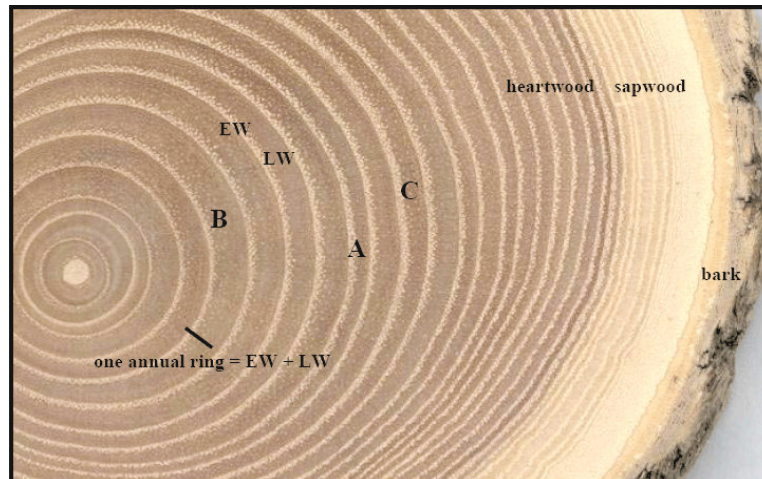
Figure IV.1: A sequence of tree rings from a red oak showing a tree ring that is narrower (A) than a tree ring that is average in width (C), and a tree ring that is wider (B) than average. EW = earlywood portion of ring, LW = latewood portion of the ring, heartwood shows up as the darker portion of the tree trunk, sapwood is consists of the lighter-colored wood[3].

In section 4.03, the methodology of measuring tree-ring widths and computational comparison of measured rings to a reference chronology will be further discussed.

Section 4.02 - Historical Terahertz Experiments on Wood

In 1998, Martin Koch, *et al* [101,102] were the first to suggest and demonstrate that the density mapping of wood would be an interesting application for terahertz transmission imaging, since wood is fairly transparent in the terahertz spectral range. Terahertz is non-destructive—in comparison to many of the mechanical measurement methods—and also provides the sub-millimeter spatial resolution that is desirable for sensing with sub-annual ring resolution. Using photoconductive switches in a transmission geometry, as described in ref. 103, they were able to sense the changes in density between the large-celled earlywood (light
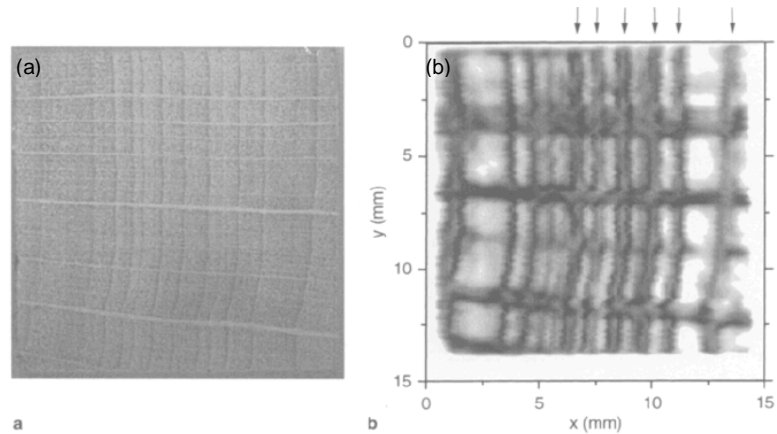
Figure IV.2: (a) Optical photograph and (b) terahertz image of a piece of beechwood [101].

grey) and the small, densely-packed cell latewood (vertical, dark grey lines), in Figure IV.2. The xylem rays (horizontal, dark grey lines) were also sensed, because its cell structures were designed to transport and retain moisture, therefore making its cells more absorbing at terahertz frequencies [104]. An absorption profile (Figure IV.3) across the specimen was extracted from the THz image and found to be comparable to the density profile of the specimen obtained using the field-standard gravitometric-volumetric method.
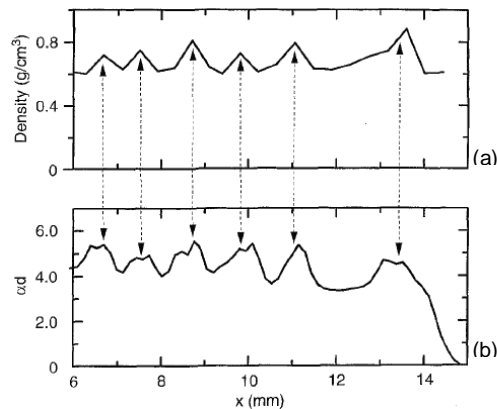
Figure IV.3: (a) Density profile obtained using gravitometric-volumetric method and (b) absorption profile extracted from the THz image of a defined section of the beech sample [101].

58

The next most significant study of wood using terahertz was not presented until Reid, *et al*, in 2006 [105] studied the terahertz birefringence and attenuation properties of wood in a transmission geometry. They were able to demonstrate that diattenuation and a frequency-independent time delay of the pulse occurs as it propagates through the wood (Figure IV.4 and Figure IV.5). These are attributable to wood having fast (perpendicular to grain) and slow (parallel to grain) complex index of refraction axes by rotating the specimen with respect to the polarization of the terahertz beam.
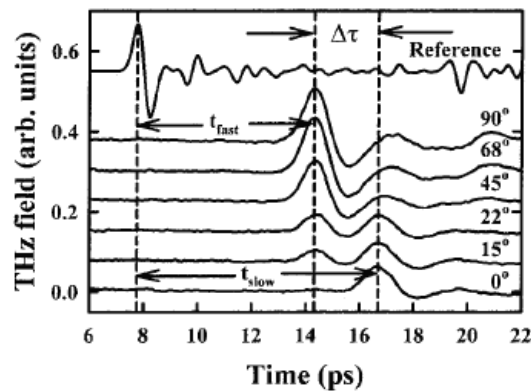
Figure IV.4: Reference and transmitted terahertz time-domain waveforms through a piece of spruce wood, measured with the THz polarization making an angle with respect to the visible grain direction [105].
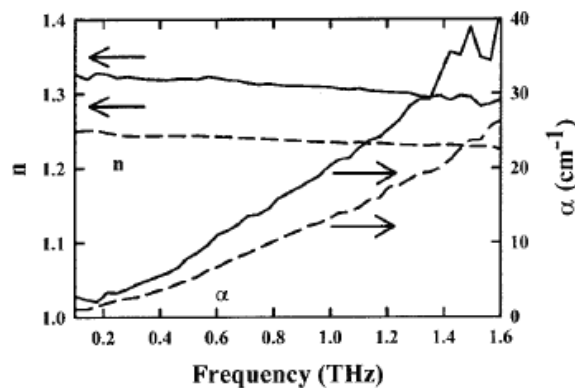
Figure IV.5: Frequency-resolved index of refraction and absorption coefficient obtained in transmission. Measurements were taken with the terahertz polarization parallel (solid) and perpendicular (dashed) to the wood grain [105].

The authors proposed that since dry wood is a very poor conductor, the grain orientation dependant absorption is due to stronger scattering of terahertz radiation from fiber cylinders of sizes on the order of a terahertz wavelength along the fiber cylinder axis.

Section 4.03 - Computational methods for Tree-ring Crossdating

Pattern recognition is an essential element of dendrochronology; therefore several conditions are required for tree-ring dating to work successfully [99]. First, the wood used to make the object must have distinct rings. Second, the object must have enough rings to provide a conclusive match with other samples. Third, a reference chronology must be available for the region from which the tree grew that was eventually crafted into an object or made into a structure. Without a reference chronology, the object cannot be dated. In the case of the experiments presented in this chapter, the terahertz images of the wooden sample will provide the "sample" ring series, while the optical photograph will provide the "reference" chronology.

Dendrochronologists commonly use software—such as COFECHA, Personal Analysis System for Tree-Ring Research (PAST), or WinDENDRO—to aid this measurement, analysis and crossdating of ring series patterns. The programs CooRecorder 7 and CDendro 7 by Cybis™ were selected for the purpose of comparing photographs of the wood samples to their terahertz images because of its low cost and user-friendly

simplicity. CooRecorder 7 allows the user to import a photograph of the wood sample and identify the ring positions, then export the normalized ring width series to be compared to another sample or a standardized reference from an established database.

Tree-ring series are crossdated both graphically (Figure IV.6) and statistically for precision. The crossdating tool, CDendro 7, enables the user to perform a ring-width transformation which detrends the series for individual tree growth rates. For hard woods such as oak, pine or walnut, the Hollstein transformation was recommended:

$$y(\text{Hollstein})_i = \log\left(\frac{y_i}{y_{i+1}}\right) \tag{30}$$

where y_i and y_{i+1} are sequential ring widths. The ring series can then be graphically represented and offset to visually match the reference chronology.
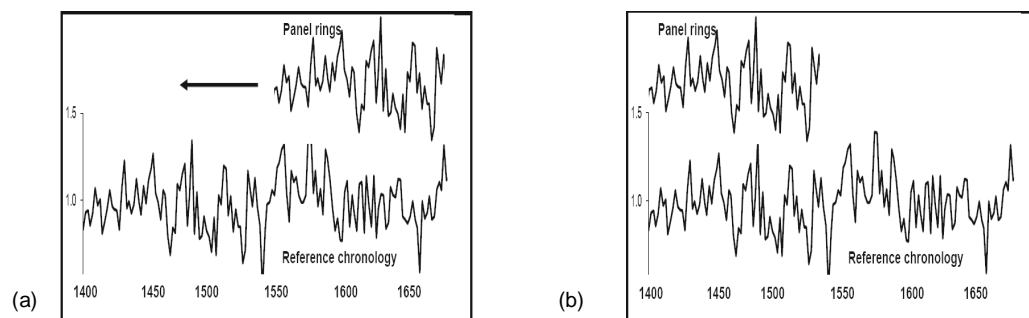
Figure IV.6: Sample tree-ring series compared with reference chronology, before and after graphical offset match [99].

For accuracy, the graphical chronology match should be statistically verified. The three most common statistical parameters used for crossdating are Gleichlaufigkeit (GLK), correlation coefficient (c_{coeff}), and an adapted student t-test [106]. The GLK represents the percentage

slope equivalence of a given sample and reference with the overlapping parts of the two series. The correlation coefficient is a percentage of overall similarity between the two series. It is given by:

$$c_{coeff} = \frac{\sum_i (s_i - \bar{s})(r_i - \bar{r})}{\sqrt{\sum_i (s_i - \bar{s})^2 (r_i - \bar{r})^2}} \tag{31}$$

where r_i and s_i are the respective Hollstein transformed ring values of the reference and sample, and $\bar{r}$ and $\bar{s}$ are the mean values of the transformed ring series. A perfect match would correspond to $c_{coeff} = 1$, while a perfect mismatch is $c_{coeff} = 0$. The correlation coefficient becomes more valuable when taking into account the length (N) of overlapping series, therefore a t-test is used where,

$$t = \frac{c_{coeff}\sqrt{N-2}}{1 - c_{coeff}^2} \tag{32}$$

The ring series were measured along several radii from the outer rings to the pith, for each wood specimen's photographic reference and terahertz image. The ring series for the photograph were averaged to produce a single reference chronology. Each ring series from the terahertz image was compared to that specimen's reference chronology to assess its equivalency, as well as to determine the threshold GLK, c_{coeff}, and t-test scores.

Sample	GLK	overlap	c_{coeff}	t-test
Pine 1	0.80 ± .09	22 ± 1	0.73 ± 0.16	6.5 ± 2.5
Pine 2	0.72 ± 0.16	24 ± 6	0.82 ± 0.11	5.7 ± 2.8
Walnut	0.86 ± 0.05	16 ± 1	0.78 ± 0.03	6.6 ± 1.7

Table IV.1: Mean statistical parameters of photographic reference time series with respect to the reference chronology.

In Hanaca, *et al*'s paper on the provenancing of Baltic timber [107], examples were given of t-test scores ranging between 4.96 and 7.47, resulting in an acceptable t-test threshold of 6.0 ± 25% for matching tree-ring series to a reference chronology. In their case, the time-series are longer with lower correlation coefficients. Here, the records are shorter, but the correlation is high, therefore both the t-test and c_{coeff} values will be considered relevant for judging good matches.   The ranges of acceptability for the median values of the specimen's cross-dating statistics are then determined by the 1/e standard deviation errors of the reference statistics.

Section 4.04 - Ranging measurements of tree ring widths

The ranging measurements were carried out using a Picometrix QA-1000 terahertz imaging system [108] consisting of a femtosecond laser fiber-coupled to an XYZ-translatable photoconductive, co-linear THz-transceiver with a 2 mm focal beam waist and ~1 cm depth of focus. The rings of the wood samples (Figure IV.7) were measured with the THz beam probing the wood parallel to the radial direction of ring growth (normal to the ring-plane of the specimen).
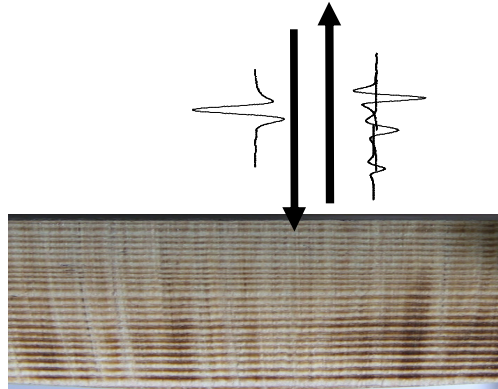
Figure IV.7: Optical photograph of pine 1 wood specimen cross-section.

Figure IV.8 shows the time-domain reflection signature of the terahertz probe pulses incident on the side of the dowel normal to the tree rings seen in Figure IV.7. The first reflection is from the air/pulp interface, while the subsequent reflections occur at the boundaries between the seasonal (early and late) wood growths, where there is a significant change in wood density, resulting in Fresnel reflections. Due to the short focal depth of the THz-beam with respect to the specimen thickness and Fresnel loss, only a limited number of rings produced reflections of significant amplitude.
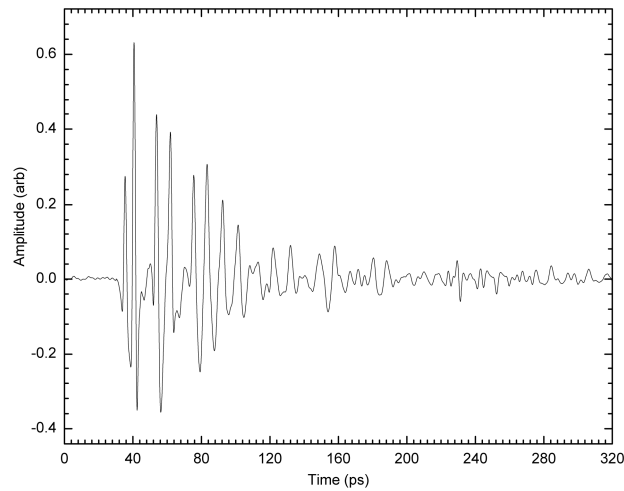
Figure IV.8: Time-domain waveform of terahertz signal reflected from the white pine wood sample of Fig. 2.
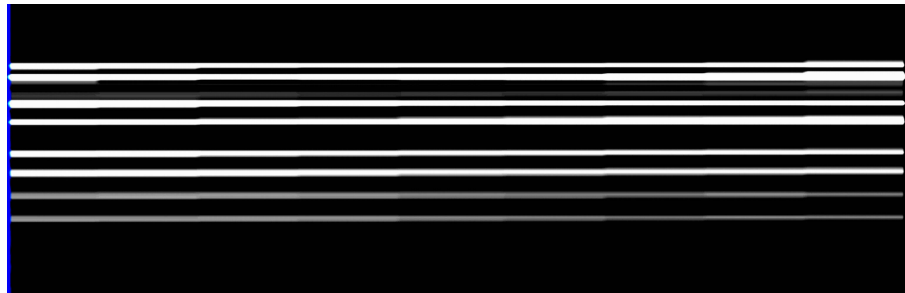
Figure IV.9: Terahertz B-scan image of signal reflected from the white pine wood specimen in Figure IV.7 (Dimensions: 20 mm x 320 ps with 2 mm x .0718 ps pixel size).

A b-scan image in Figure IV.9 is a time-domain based cross-sectional image of the specimen scanned across its width, where the vertical axis corresponds to time and horizontal axis corresponds to the amplitude of the time-domain signal along the x-position. The bright lines represent the strongly reflected THz-signal at the earlywood/latewood boundaries, thus the distance between the white lines are comparable to ring widths.

Table IV.2 shows the results of comparing the collection of b-scan ring widths with the pine 1 specimen's reference chronology. Since the

terahertz image of the pine 1 specimen was very uniform with respect to the scanned area, there was a significantly higher correlation between each series measurement within the collection than within the reference collection.

Parameter	Mean	Minimum	Median	Maximum
c_{coeff}	0.96 ± 0.005	0.96	0.96	0.97
t-test	6.95 ± 0.60	6.1	7.1	7.5
overlap	5.75 ± 0.5	5	5	6

Table IV.2: Statistical results of comparison between pine specimen b-scan and its reference chronology.

Nonetheless, there was a strong match between the terahertz-sampled ring widths and the reference chronology. Given the limited number of sampled rings, a median t-test score of 7.1 is very strong match, falling well within the threshold range of 4 – 8 and within 10% of the threshold value of 6.5.

There are, however, limitations to this method of measuring tree-rings. As discussed in section 4.02—wood is a birefringent material, therefore it is imperative to optimize the fiber alignment with the polarization of the terahertz beam in order to further reduce signal attenuation due to scattering and Fresnel losses. Figure IV.10 shows the
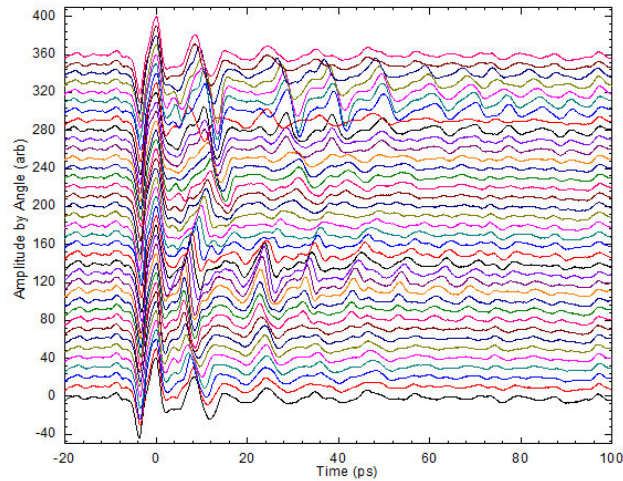
Figure IV.10: **Time-domain amplitude waveforms of pine specimen over 360 degree rotation.**

angular dependence of the fiber orientation with respect to the terahertz beam polarization. As the wood specimen is rotated from 0° through 360°, the separation of the reflections from the first and second interfaces varies cyclically, while the reflections from the subsequent layers are enhanced or attenuated accordingly. The diagonal, rather than either the fast or slow axes result in the best signal strength for reflections from more deeply embedded rings. There is sinusoidal change in optical delay
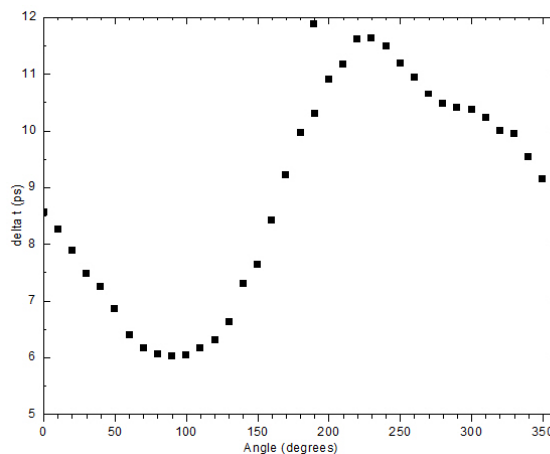
Figure IV.11: **Time delay between surface reflection and primary ring reflection as a function of the rotation angle.**

between the ring reflections as the specimen is rotated (Figure IV.11),. Therefore the orientation should be optimized for maximum interface reflections, with minimum time in between them. This method of measuring tree-rings may be a valuable method of extracting information about how carpenter or artist selects their cuts of wood, based on fiber orientation.

Section 4.05 - Tomographic Measurements of Tree Rings
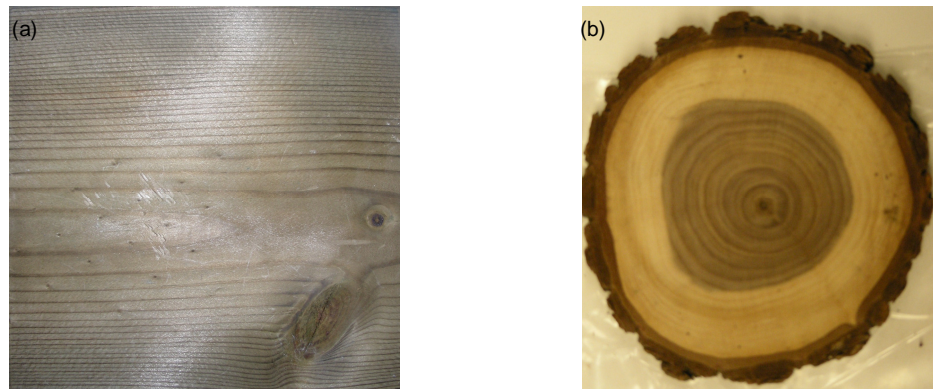
Figure IV.12: Optical photograph of the (a) pine 2 and (b) walnut wood specimen.

In addition to varnishing wood for frames, furnishings, aesthetic room structures, et cetera, it was not uncommon for artists to create paintings on thin wood panels instead of canvas. Hence there is a great deal of interest in determining the ring patterns that exist under the paint within these framed substrates without removing the frame or otherwise disturbing the integrity of the painting. As a result, three wood specimen

were studied to simulate these multilayer systems: 1) another pine specimen (Figure IV.12a) coated with 3 layers of acrylic varnish, 2) a walnut specimen (Figure IV.12b) coated with a layer of primer (calcium sulfate gesso and animal glue) and 3) another walnut specimen cut from the same region coated with a layer of primer and paint (lead white oil).
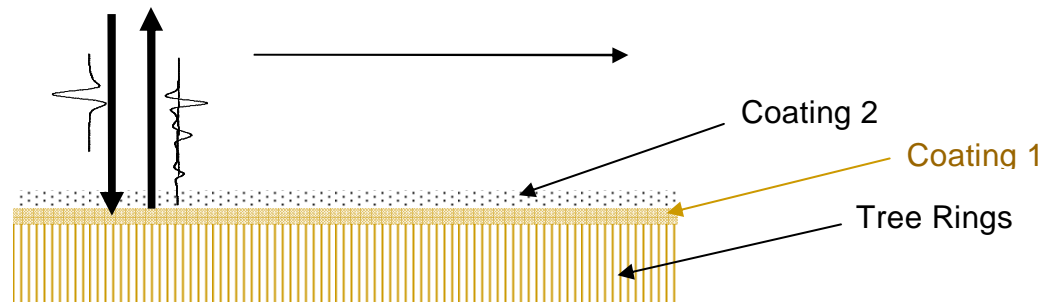
Figure IV.13: Schematic of the tomographic measurement of the walnut specimen beneath multiple coating layers.

For the tomographic measurements (Figure IV.13), the THz-beam probed the wood normal to the radial ring growth direction or parallel to the ring-plane as show in the figure below. Because of the difference in index of refraction for each coating layer, the information on the obscured wood layer can be extracted by analyzing only the terahertz-pulse reflected from the coating/wood interface.

Figure IV.14: THz image of section of unvarnished pine 2 wood specimen (100 mm x 10 mm dimensions, 0.25 mm x 1 mm pixel size).

Figure IV.15: THz image of varnished pine 2 wood specimen (100 mm x 10 mm dimensions, 0.25 mm x 1 mm pixel size).

Figure IV.14 and Figure IV.15 show images of the unvarnished (bottom) and varnished (top) pine 2 specimen sections. They were calculated by integrating the power spectra of the first reflections from the specimen from 0.5 - 0.8 THz and 0.5 – 1.0 THz, respectively, to optimize the spatial resolution. The tree-ring series were repeatedly measured from the left and right sides of the center pith—in order to both double the number of tree-ring series measured from a single specimen and to demonstrate the radial symmetry of the tree-ring growth—and aligned to each other by optimizing the GLK and overlap.

Figure IV.16 compares the mean of unvarnished and varnished specimen to their photographs, with the 35th ring corresponding to the last before the pith. The unvarnished image produces the most precise overall tree-ring series replication, since the more tightly spaced tree-rings were easier to resolve. However, for the THz image of the varnished specimen, several individual ring-width blocks within the series had strong correlation to both the photographic reference and the terahertz image of the unvarnished sample.
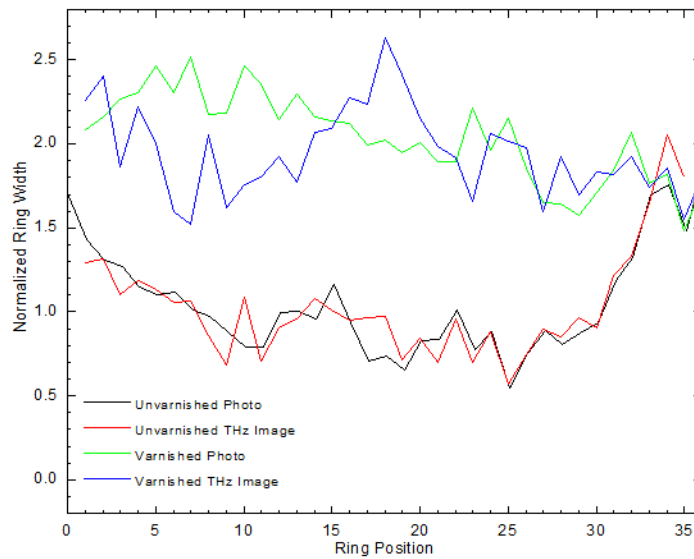
Figure IV.16: Comparison of mean tree-ring series of a photograph and a terahertz image of the pine 2 wood specimen.

For the unvarnished pine 2 specimen (Table IV.3), both the median c_{coeff} and t-test values were nearly identical to the threshold values of the photographic reference. For the varnished specimen (Table IV.4), the median t-test value was within the threshold range, however the correlation coefficient was slightly below it. It should also be feasible to use block analysis to correlate and cross-date other terahertz images of wood specimen believed to be from the same region, irrespective of the coating status because of the high correlation despite the limited number of overlapping contiguous segments.

Parameter	Mean	Minimum	Median	Maximum
c_{coeff}	0.72 ± 0.17	0.35	0.81	0.91
t-test	5.65 ± 2.5	1.9	5.8	11.9
overlap	24 ± 6	18	22	33

Table IV.3: Statistical parameters of unvarnished pine 2 specimen with respect to pine 2 reference chronology.

Parameter	Mean	Minimum	Median	Maximum
C_{coeff}	0.62 ± 0.22	0.26	0.69	0.97
t-test	3.8 ± 2.4	1.3	3.4	11.3
overlap	20 ± 9	6	19	31

Table IV.4: Statistical parameters of varnished pine 2 wood specimen with respect to pine 2 reference chronology.

The terahertz images of the unprimed and primed walnut 1 specimen, shown in Figure IV.17 were compared to the optical photograph of the unprimed walnut 1 specimen. Figure IV.17a was obtained using a peak-to-peak amplitude analysis of the 1st reflected time-domain pulse, while Figure IV.17b represents an amplitude analysis at 600 GHz of the pulse reflected from the primer/wood interface. Visually, the tree-rings were resolvable, despite their compactness. However, statistically they did not compare to their reference chronology as well as the pine 2 specimen did to its reference chronology. This could be attributed to the subtle variations in light and dark wood thicknesses during early growth being more significant when the sample length and diameter is small.

(a)   (b)
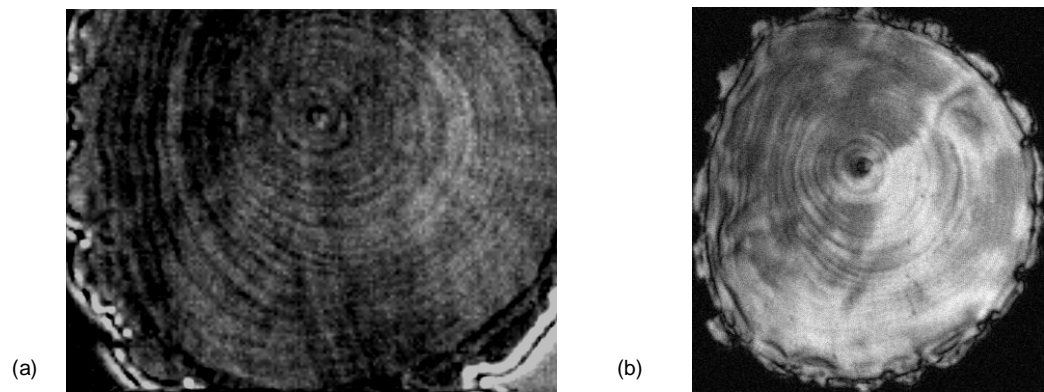
Figure IV.17: Terahertz images of walnut stem (a) uncovered and (b) primed cross-sections.

For the terahertz image of the unprimed walnut specimen (Table IV.5), the correlation coefficient was 6% below threshold, however the median t-test score was well within the threshold limit. The statistics for the primed walnut specimen (Table IV.6) were not as good. The t-test score was only out of range by 5%, however the c_{coeff} exceeded the threshold range by 28%. As such, it is questionable as to whether an adequate match would be made beneath the primer.

Parameter	Mean	Minimum	Median	Maximum
c_{coeff}	0.86 ± 0.05	0.82	0.85	0.93
t-test	6.6 ± 1.7	5.2	6.1	9.4
overlap	16 ± 1	15	16	17

Table IV.5: Statistical parameters of THz image of unprimed walnut specimen 1 with respect to walnut reference chronology.

Parameter	Mean	Minimum	Median	Maximum
c_{coeff}	0.51 ± 0.11	0.11	0.54	0.66
t-test	1.9 ± 0.56	1.1	2.0	2.6
overlap	12 ± 3	8	12	15

Table IV.6:Statistical Parameters of THz image of primed walnut specimen 1 with respect to walnut reference chronology.

For finer spacing between tree-rings, it is arguable that precise image resolution and ring measurement become imperative because of the possibility of missing rings or falsely measuring rings. Nonetheless, the quality of individual series' graphical matches and block GLK and c_{coeff} analyses suggest that comparing short blocks of longer (>50) tree-ring series to a reference chronology may actually provide higher t-test results and more precise cross-dating matches.

The terahertz image of the primed-and-painted walnut 2 specimen (Figure IV.18) was obtained by integrating the entire spectrum of the pulse reflected from the back surface of the specimen (i.e., the shadow). The measured tree-ring series were then compared to the original walnut 1 reference chronology.
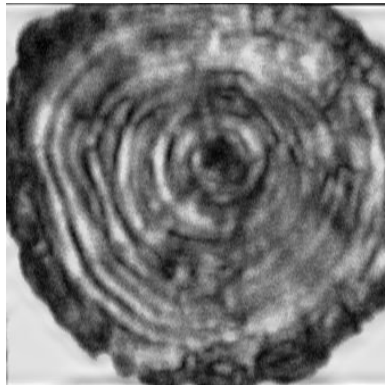
Figure IV.18: THz shadow image of walnut 2 specimen beneath primer and paint.

Parameter	Mean	Minimum	Median	Maximum
c_{coeff}	0.58 ± 0.13	0.42	0.56	0.80
t-test	2.0 ± 0.75	1.2	1.9	3.3
overlap	9 ± 2	7	10	11

Table IV.7: Statistical Parameters of THz image of primed and painted walnut specimen 1 with respect to walnut reference chronology.

Equivalent statistical results (Table IV.7) were obtained when matching the two different walnut specimen from the same region. This result both justifies the applicability of THz-pulse imaging of wood specimen and qualifies the importance of careful block selection.

Section 4.06 - Conclusion

Several wood specimen were investigated using terahertz time-domain reflectometry. Tree-rings measured parallel to growth using

ranging had limited penetration, but statistically consistent depth resolution. Tree-rings imaged perpendicular to growth were spatially resolvable using tomography. The statistical accuracy of the natural and varnished wood specimen was high in comparison to their reference chronologies. The correlation coefficients and t-test scores for primed and painted specimen were not adequately matched to their references, but were similarly matched to each other. There is still some promise that THz-TDR will be useful for the dendrochronological cross-dating of wood panel paintings.

CHAPTER V: TERAHERTZ TIME-DOMAIN REFLECTOMETRY OF ARTWORK

Section 5.01 - Introduction

Spectroscopy and imaging have become well-established tools in the evaluation and conservation of drawings, paintings, sculptures, and many other art forms. Electromagnetic radiation-based measurement techniques exploit the fact that materials reflect, absorb, and emit radiation in ways that depend on their molecular composition. For example, x-ray fluorescence spectroscopy [109], Raman spectroscopy [110], laser-induced breakdown spectroscopy (LIBS) [111] and infrared spectroscopy [112,113] have been used for the analysis of the chemical components of artist's media. However, unlike chemical analysis, they are non-invasive and rarely require specimen to be removed from the art sample—which is beneficial to the preservation of the work of art being studied. Spectroscopic methods can be limiting, however, in that the measurements tend to be single point (or localized). Therefore the information obtained from the specimen may not always correlate with the larger sample area.

Spectroscopic imaging is a way to obtain a work's spectral information over a large surface area of work. In recent years, multi-spectral imaging [114,115] acquisition systems have been developed—

collectively using x-ray, ultraviolet (UV) [109], visible, infrared (IR) [116,117] and microwave [118] radiation.   In addition to being used to analyze the chemical composition of art media, these imaging methods can, layer by layer, reveal superficial changes, hidden layers of paint, and sub-surface damage in art work, such as with Leonardo da Vinci's Adoration of the Magi (Figure V.1).
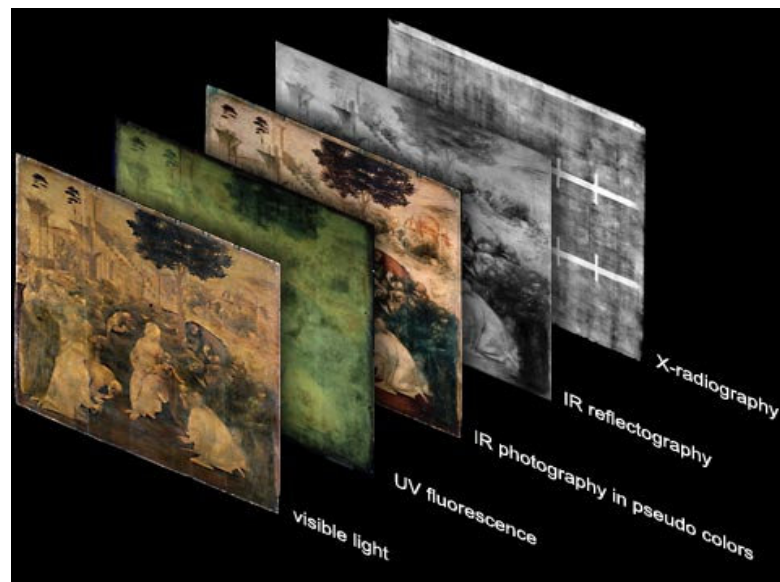
Figure V.1: Multispectral diagnostic imaging used to examine Leonardo da Vinci's Adoration of the Magi. *(Courtesy of Editech, M. Seracini)*
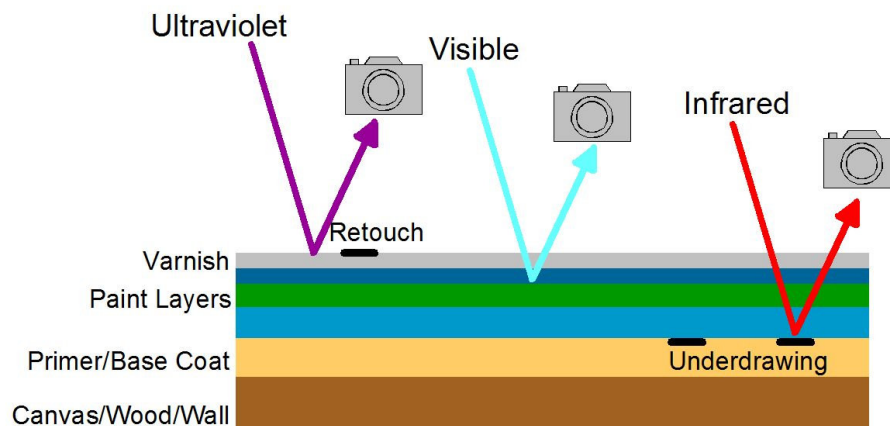
Figure V.2: Schematic of layers measurable by UV, visible, and IR reflectance spectroscopy (courtesy University of Pisa, Italy by Gianluca Farusi).

UV, Visible, and IR spectroscopic reflectance imaging methods, however, are limited by the number and thickness of layers that can be studied since the penetration depth of radiation is proportional to its wavelength. Figure V.2 shows the layers that are accessible by each technique. X-rays and microwaves can penetrate thick layers. However, x-rays yield no depth resolution, and therefore the information obtained from one layer is inseparably superimposed onto the information from another layer. On the other hand, microwaves (at frequencies below tens of gigahertz) have poor lateral spatial resolution, and therefore only features on the order of centimeters and larger can be clearly imaged.

Terahertz radiation can penetrate thick layers of many non-polar, non-metallic optically opaque materials. In reflection, THz-pulse separation between materials of suitable optical thickness and terahertz beam control can enable individual layers to be resolved. Aperture-less THz-imaging can obtain spatial resolutions on the order of tens of microns, while THz-imaging using apertures can obtain sub-diffraction limited resolution. Therefore, the use of terahertz time-domain spectroscopic imaging (THz-TDSI) [109,119] as a nondestructive, multispectral-imaging tool to supplement the current technology is being proposed.

In this chapter, the time delays and intensity signatures of terahertz pulses reflected from multilayer systems of sketch drawings, paint, and plaster and were investigated in order to demonstrate the feasibility of using terahertz techniques for inspecting and resolving artwork,

particularly frescoes embedded in subsurface layers within a wall or ceiling. It has been observed that it is possible to spectrally distinguish pigments and other artist's media, as well as to identify hidden layers— including sketches and paint patterns—through coats of paint and thick layers of plaster.

Section 5.02 -   Spectroscopic Measurements of Artist's Media

The first step to spectroscopic imaging of art is to establish a basic understanding of the optical properties of materials used in art.   A selection of pigments and sketch materials commonly used by historical and contemporary artists was obtained. A complete list and description of these media are found in Appendix I.

A. Time-domain Index Measurements of Pigments

Four of the pigments were densely packed into optical cuvets and measured in transmission. The time-domain transmission signals with and without the pigment samples present in their cuvets (Figure V.3) can be compared in order to obtain a bulk index of refraction calculation.
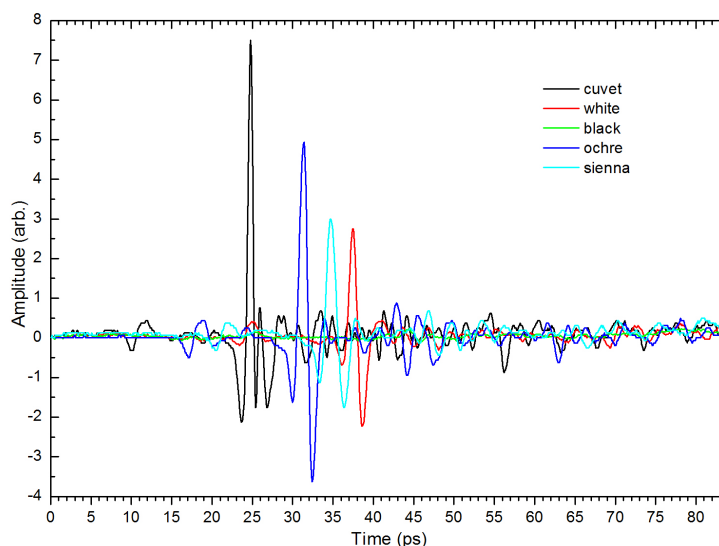
Figure V.3: Time-domain waveforms of THz-pulses propagating through same volume of four pigments compared to air reference.

Since the optical density (and thus the real index of refraction) of the pigment is proportional to the time it takes for the pulse to propagate through the same volume of pigment as in air, the bulk refractive index can be determined by:

$$n = n_{air} + \frac{c}{d} \Delta t \tag{33}$$

The results from the real part of the refractive index for the pigments are

Pigment	Bulk Index
Mixed Black	1.57
Titanium White	1.70
Yellow Ochre	1.35
Burnt Sienna	1.52

consolidated in

Table V.1: Bulk index of refraction of dry pigments computed from time-domain terahertz transmission measurements.

80

B. Frequency-domain Index Measurements of Artist's Media
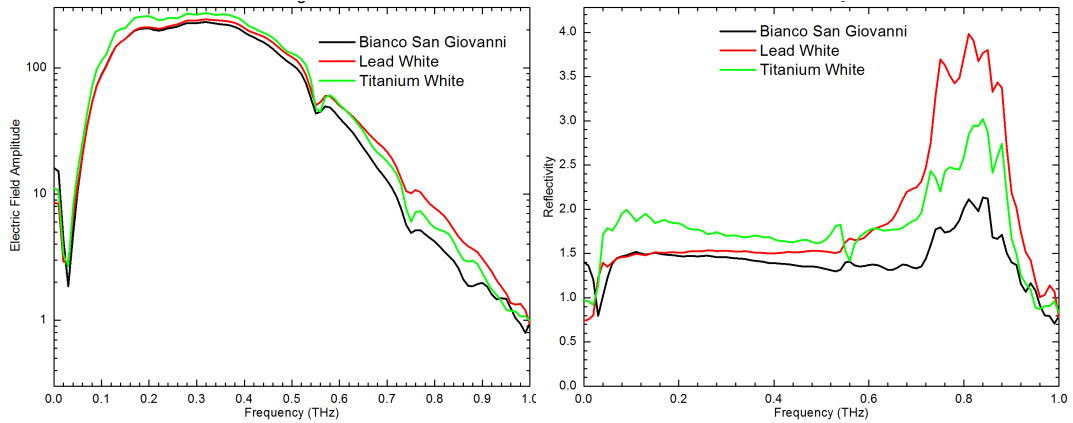
Figure V.4: Electric field amplitude and reflectivity spectra of white pigments.

The pigments were also studied using THz time-domain pulse reflectometry and the co-linear THz reflectometer described in section 1.02B. A pure pigment palette was prepared by binding the powders with water—which completely evaporated before measurement—and applying them to a cloth substrate. The spectral information on the entire palette can be found in Appendix II. Here, only Bianco San Giovanni (calcium hydroxide), lead (carbonate) white, and titanium (dioxide) white—which are metamers, or colors that visually appear the same—will be presented to show that they can be spectrally distinguished.

The reflected pulse was Fourier-transformed to obtain the complex electric field spectra (Figure V.4a) of the pigments, given by

$$\tilde{E}_{sample}(\nu) = \tilde{r}(\nu)\tilde{E}_{reference}(\nu) \tag{34}$$

where the complex reflectivity of the pigment is given by the relative field magnitude, $r(\nu)$, and relative phase, $\phi(\nu)$, of the pigment and cloth palette

81

The Fresnel definition of the reflectivity is defined in the complex form by:

$$\frac{\tilde{E}_{sample}(\nu)}{\tilde{E}_{reference}(\nu)} = \left|r(\nu)\right|e^{i\phi(\nu)} = \frac{n+i\kappa-1}{n+i\kappa+1} \qquad (35)$$

where $n(\nu)$ is the real index and $\kappa(\nu)$ is the extinction coefficient, related to the absorption coefficient by:

$$\kappa(\nu) = \frac{c}{4\pi\nu}\alpha(\nu) \qquad (36)$$

Equation 35 can be inverted and solved to obtain the frequency-dependent refractive index and absorption as a function of the relative amplitude and phase.

$$n(\nu) = \frac{1-\left|r(\nu)\right|^2}{1+\left|r(\nu)\right|^2 - 2\left|r(\nu)\right|\cos\phi(\nu)} \qquad (37)$$

$$\alpha(\nu) = \frac{4\pi\nu}{c}\frac{2\left|r(\nu)\right|\sin\phi(\nu)}{1+\left|r(\nu)\right|^2 - 2\left|r(\nu)\right|\cos\phi(\nu)} \qquad (38)$$
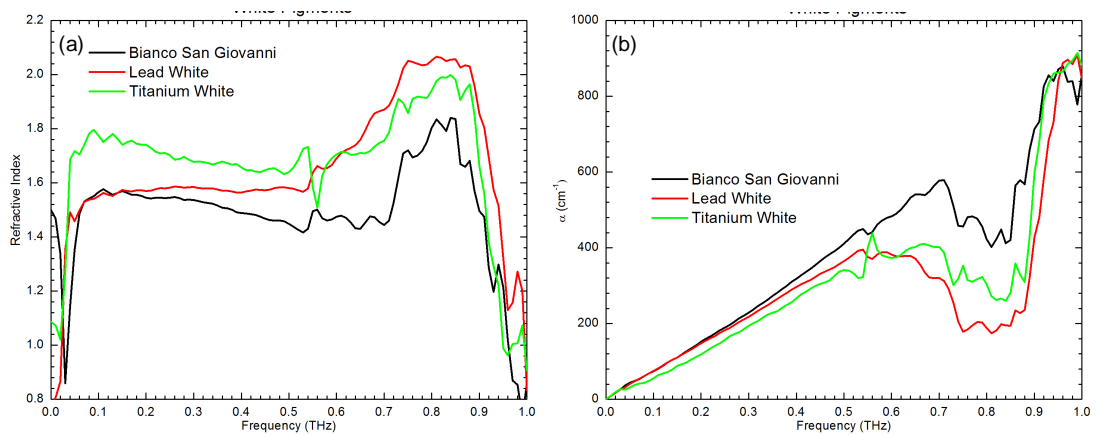
Figure V.5: (a) Refractive index and (b) absorption spectra of white pigments.

Atmospheric water-resonance features can be seen at 0.56, 0.75, and 0.99 THz in Figure V.4 and Figure V.5. Between 0.66 and 0.90 THz, there appear to be features characteristic only of the cloth substrate, which may be related to scattering of terahertz wavelengths on scale with the weave and thread of the cloth. Otherwise, the white pigments themselves have nearly spectrally-independent refractive indices and linearly-dependent absorption, which would be expected from a color that is defined by its broadband reflection of visible wavelengths.
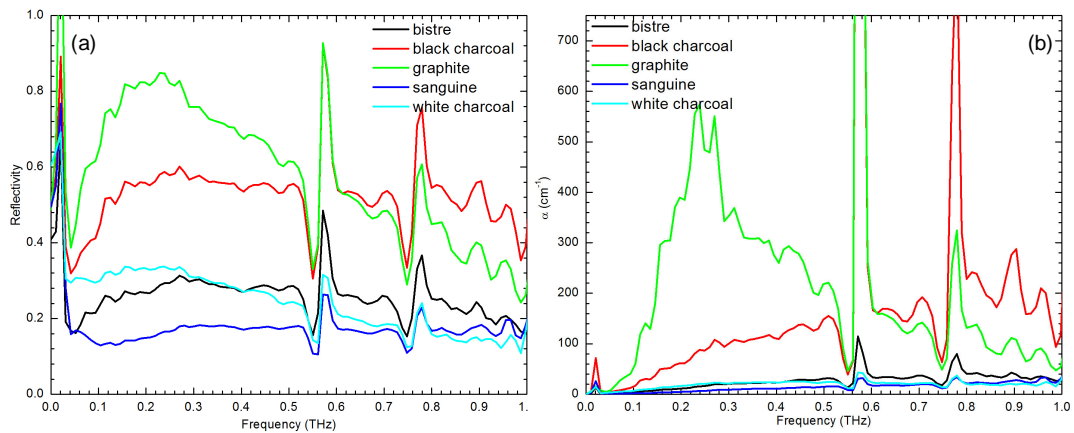
Figure V.6: (a) Reflectivity and (b) absorption spectra of five common sketch materials.

Figure V.6 shows the reflectivity and absorption spectra of pure, compressed bistre, black charcoal, graphite, sanguine, and white charcoal. All are carbon-based materials, except sanguine which is iron oxide-based, but are processed differently. Graphite has a dense, layered molecular structure that makes it a moderate quality semiconductor, which results in significantly higher reflectance and absorption compared to the other materials. Black charcoal has moderate reflectance and absorption— lower than graphite because of its amorphous structure, but higher than

bistre and white charcoal because of its molecular purity. Sanguine—a material popularly used by Renaissance artists for underdrawings—appears to be nearly transparent.

C. Spectroscopic Imaging of Artist's Media
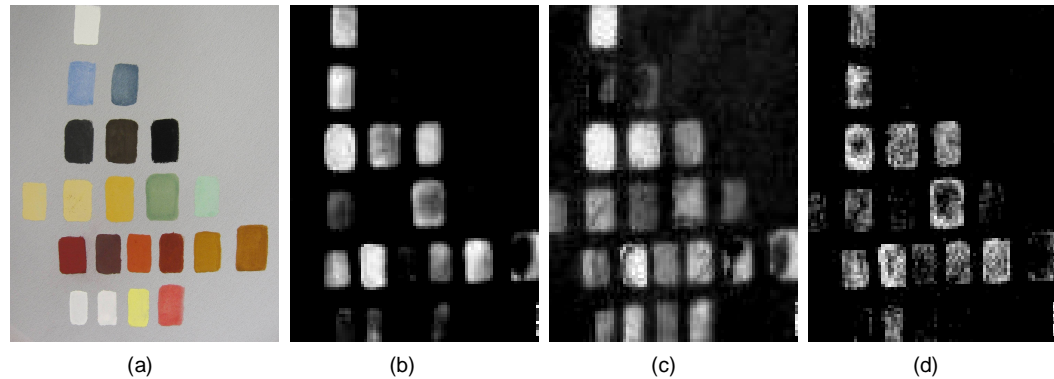
Figure V.7: (a) Optical photograph and terahertz images of paint palette at (b) 0.2 THz, (c) 0.5 THz, and (d) 0.8THz frequency bin.

Creating an image based on the reflected field amplitude from a monochromatic source is one of the simplest methods of spectroscopic imaging. Using a broadband THz source enables the creation of many images from a single acquisition, limited in number by the spectral resolution and bandwidth. Figure V.7a shows an optical photograph of the paint palette mentioned previously. The names and locations of each pigment can be found in Appendix I. Figure V.7b-d are spectroscopic images of the palette where the pixel value, M, is the spectrum amplitude at three terahertz frequency bins. The intensity signatures of the pigments vary with frequency. The most notable variation being the "appearance" and subsequence "disappearance"—at 0.5 and 0.8 THz, respectively—of the yellow pigments in the fourth row and the third red in the fifth row.

Despite the color difference, the three come from the same family of pigments, called ochres. The intensity signatures of the white metamers are also similar to their spectral behavior in Figure V.4.
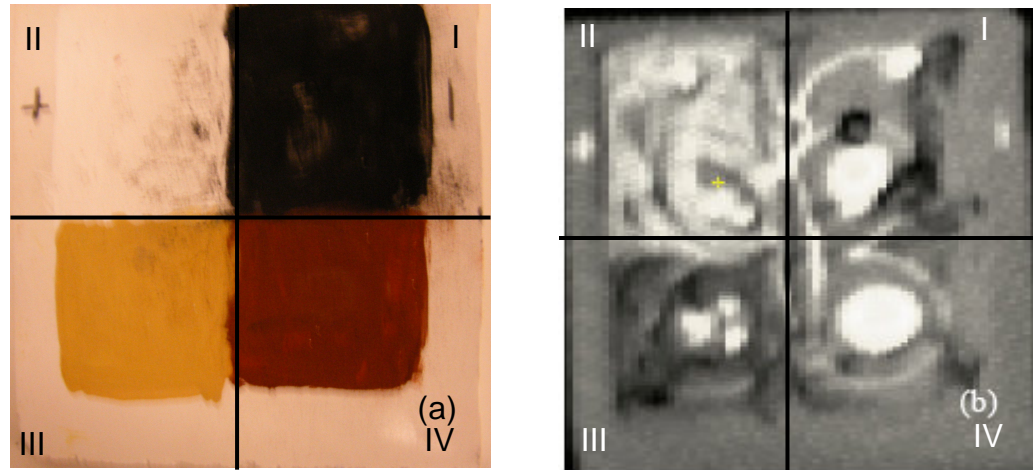
Figure V.8: (a) Optical photograph of the front surface of a multilayer painting. (b) THz-TDS image of the painting, with the subsurface butterfly underdrawing visible through the surface. The image was formed using a power integration of the spectral information between 0.28 -and 0.74 THz (60 mm x 60 mm dimensions and 0.5 mm x 0.5 mm pixel size).

Graphite sketches covered by an opaque layer of paint were also scanned. Figure V.8b shows the butterfly image emerging from under a paint layer consisting of four quadrants of white, black, burnt sienna, and yellow ochre pigment. Here, the spectral image was calculated using a power integration of the pulse spectrum between 0.28 and 0.74 THz, instead of a single frequency bin. The pixel value becomes:

$$M = \int_{\nu_b}^{\nu_b} |E(\nu)|^2 d\nu \qquad (39)$$

Note that changes in the thickness and composition of the paint in the four quadrants of Figure V.8 are discernible, and that the gray-scale can change depending on the refractive index of the adjacent media. The

relative index differences between the white and yellow ochre pigments and similarities between the black and burnt sienna pigments correspond to the apparent color domains in the THz image in Figure V.8b, as well as the reflected spectral amplitudes (which can be found in Appendix II).

Section 5.03 - Terahertz Time-Domain Imaging of Fresco Models

Frescoes are mural paintings constructed using pigments and a binding medium on a plaster surface.   For environmental and cultural/political reasons, it is common for these paintings to be obscured by pollution, additional paint, and/or addition layers of paneling or plaster. It is desirable for conservators to reveal these hidden works without risking any valuable surface work or support structure. As a spectral imaging tool, time-domain terahertz pulses have an advantage over other methods because the penetration depth of the terahertz beam is limited primarily by scattering and material absorption. Most materials that are opaque in the UV to near-infrared range of the EM spectrum are semi-transparent to terahertz radiation. Plaster is a notable example of this. While infrared light may penetrate a layer of plaster as thick as 500 μm, in this thesis reflected THz-signals were measured through layers as thick as 1 cm.

With the limitations of X-rays and microwaves that were presented in Section 4.01, THz-pulse reflectometry may be a unique spectroscopic tool for imaging drawings or paintings that have been obscured by plaster. THz-TDR was used to resolve distinct dielectric patterns through optically

thick layers of paint and plaster. The time delays and intensity signatures of the THz-pulses reflected from multilayer systems of plaster, painted surfaces, and graphite sketches were investigated in order to demonstrate the feasibility of using terahertz techniques for inspecting and resolving fresco artworks embedded in subsurface layers within a wall or ceiling.

Initially, a sample composed of a 60 mm x 35 mm x 4.35 mm thick plaster-of-Paris slab (Figure V.9) was prepared. One-dimensional dielectric and metallic vertical stripe paint patterns were first resolved through plaster and painted-plaster overlayers in this system by measuring the peak intensity of THz pulse reflections arising from refractive-index mismatches at the interfaces of different fresco layers.
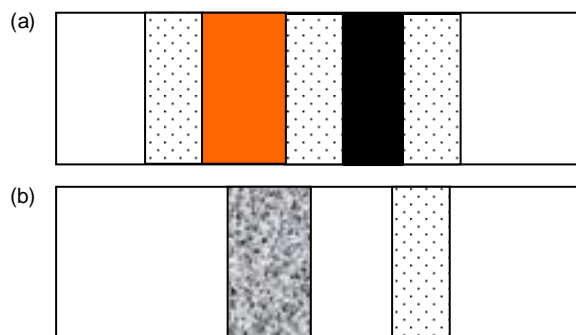
Figure V.9: (a) Front surface pattern, with strip widths: 5 mm titanium dioxide white (dotted region); 8 mm iron oxide burnt sienna and iron oxide black; 5 mm titanium dioxide white (dotted); 5 mm mixed carbon and iron oxide black; 4.5 mm titanium dioxide white paint (pigment with water as binding medium). (b) Back surface pattern: 8 mm silver paint and 5 mm titanium white paint, separated by a 6.5 mm blank region.
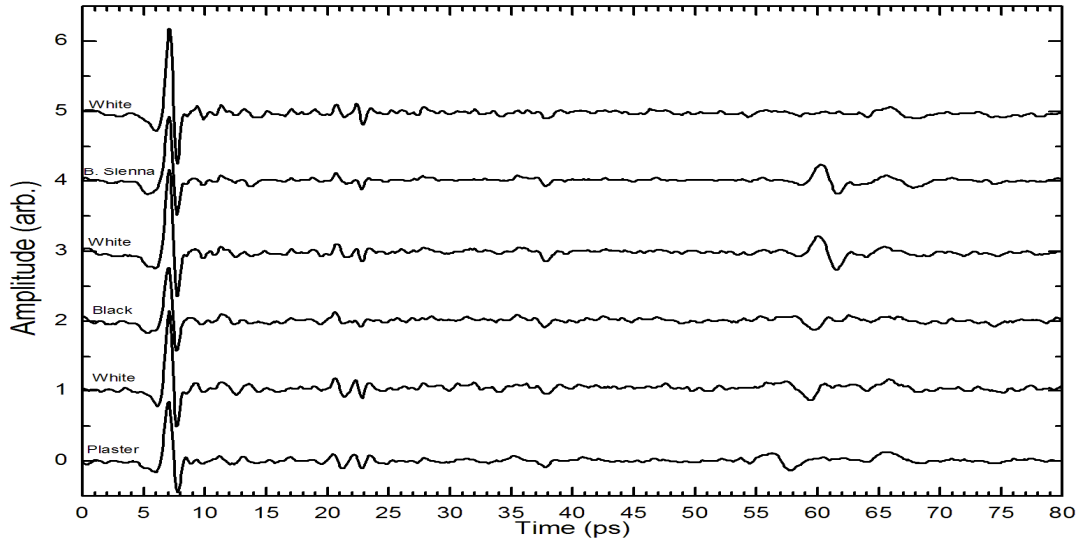
Figure V.10: Time-domain reflected THz pulses from six points along a line scan across the fresco painting depicted in Fig. 1. The waveform labels refer to the 1st surface, or front surface, pigment.

A typical set of time-domain data from a one-dimensional scan is shown in Figure V.10 where one observes independent pulsed-THz reflections from each side of a plaster substrate. The optical delay between the front and back surface reflections can be given by:

$$\Delta t = \frac{n_{pt}^2}{\sqrt{n_{pt}^2 - \sin^2\theta}} \frac{d_{pt}}{c} + \frac{n_{pl}^2}{\sqrt{n_{pl}^2 - \sin^2\theta}} \frac{d_{pl}}{c} \qquad (40)$$

where n_{pt}, d_{pt} and n_{pl}, d_{pl} are the indices of refraction and thicknesses of the paint and plaster layers, respectively, θ is the incidence angle of the terahertz beam at the air/front surface interface, and c is the speed of light in a vacuum. The front-surface returns—their electric-field peaks influenced by bands of paint of the colors noted on the figure (e.g., to first order, the white paint stripes reflect a larger peak signal than the other colors)—appear at the 7 ps time reference, while the back surface returns arrive about 55 ps later. As expected, it can be seen that the electrically-

conductive-paint reflection is also out of phase with the returns from the dielectric white paint/plaster and plaster/air back interfaces residing behind the other front-surface paints.
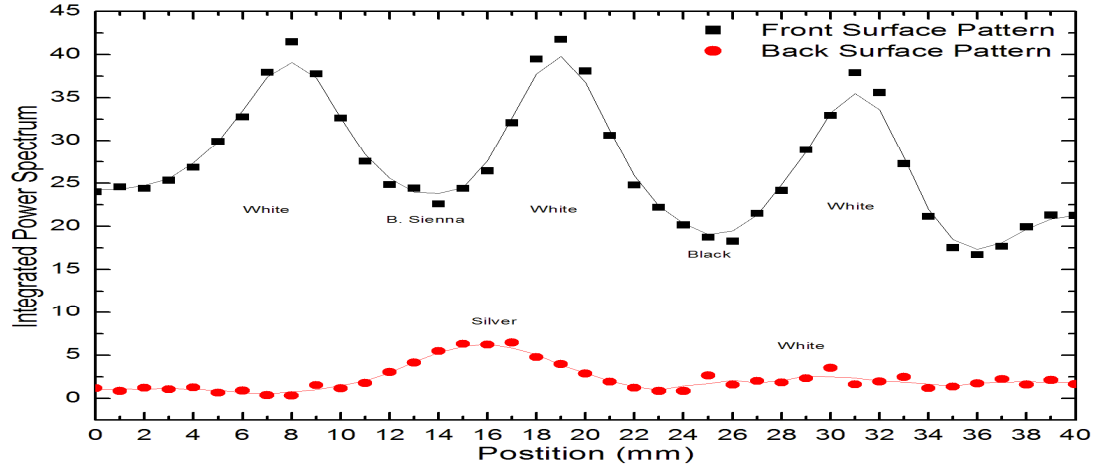
Figure V.11: Integrated power spectrum of front (square) and back (circle) surface reflections with solid-line smooth fit, measured in 1mm increments across fresco painting.

Figure V.11 shows the integrated spectral power of the reflected electric field peak, given by:

$$\int_{\epsilon\nu} \left| F\{E(t)|_{t_a}^{t_b}\} \right|^2 d\nu \tag{41}$$

where the integrand is the Fourier Transform of the time-domain electric field reflection in question with a single maximum peak between t_a and t_b picoseconds, and $\Delta\nu$ is the bandwidth of the incident terahertz pulse. On the front surface, the high contrast in reflectivity between the white, burnt sienna, and black paints easily distinguishes the color domains. The broadening of the measured color domains, as compared to their actual widths, may be attributed to a 6 mm $1/e$ THz spot size in this initial experiment. On the back surface—behind only the middle white and the

burnt sienna paint stripes—the silver paint stripe yielded a significantly larger reflection than the white paint stripe—situated partially behind another white paint stripe (which significantly filtered the amount of field propagating through the plaster).

Figure V.12: Time-domain power integration of THz-beam reflection from plaster/graphite/plaster interface. The graphite image of a butterfly, extracted from between plaster layers, is readily recognizable.

The graphite butterfly drawing in Figure V.8b was also measured through its 4 mm thick plaster substrate. After time-gating the portion of the THz signal that returned solely from the rear of the substrate, a pattern of 1-2 mm wide graphite lines from the far side of the plaster was imaged. Specifically, the images of a butterfly are clearly observed when the THz-transceiver focal plane is adjusted to the back of the plaster substrate. Images with air, wood, and additional plaster on the backside of the substrate were obtained, with the best contrast being seen with a plaster underlayer.

The next stage was to produce a two-dimensional image of a painting under plaster. The painting, consisting of five different pigments (Bianco San Giovanni, Glauconite, Hematite, Shungite and Yellow Ochre)—modeled after a section of a cathedral in Vif, France—was applied to the surface of 5 mm of wet, slaked-lime plaster on a wood panel and allowed to dry. Another 5 mm layer of the same plaster mixture was applied over the painting, then a face and background was painted over it.

Figure V.13: Optical photographs of (a) the base "Vif shapes" and (b) the top "Face" painted fresco layers (150 mm x 150 mm).

The initially uncovered "Vif shapes" fresco in Figure V.13a was imaged using the painted layer as the focal plane in order to set the maximum expectation for the covered image in Figure V.13b. Figure V.14a shows the image of the painting calculated only using the THz-pulse reflected from the air/paint interface, as per Equation 41. The boundaries of each color domain are well defined, although the red, yellow and green paints are not readily distinguished from each other.
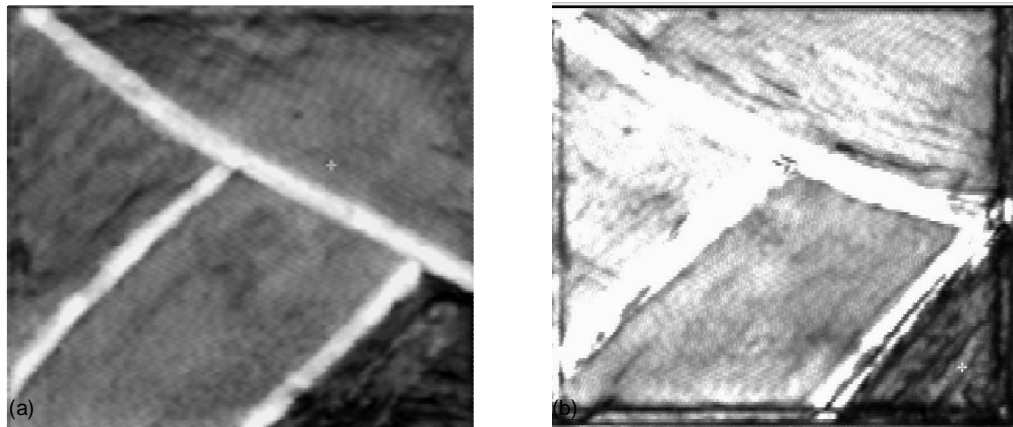
Figure V.14: Terahertz images of uncovered "Vif shapes" fresco: (a) calculated by integrating the entire spectrum of the reflected pulse and (b) calculated by integrating the spectrum between 0.15 THz and 0.50 THz (0.5 mm x 0.5 mm pixel size).

However, by integrating the spectrum of the entire time-domain signal between 0.15 and 0.50 THz (via Equation 39), it was possible to determine that at least the red domain was a different pigment from the yellow and green domains (Figure V.14b).
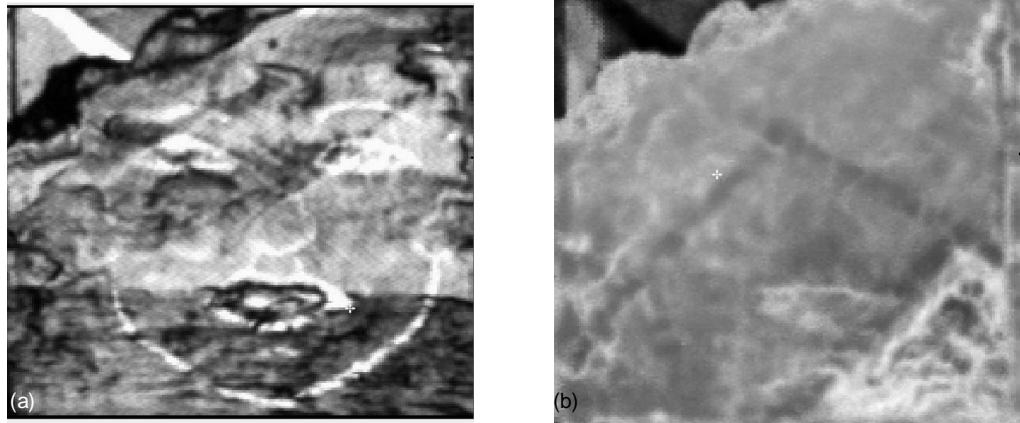
Figure V.15: Terahertz images of (a) "Face" fresco covering "Vif Shapes" and (b) "Vif Shapes" fresco beneath paint and plaster (0.5 mm x 0.5 mm pixel size).

Figure V.15b was taken after the "Vif Shapes" fresco was covered by the "Face" fresco and created by integrating the spectrum of the entire time-domain signal—which included reflections from the "Face," "Vif Shapes," and wood panel layers—between 0.17 and 0.84 THz for maximized contrast between the five pigments. Despite the image noise due to the superimposed layers, the features of the face, as well as several of the decorative color domains are distinguishable. In the upper left corner, part of the "Vif Shapes" fresco has been exposed and the red, green, and black color domains are distinctive there.

Figure V.15b reveals the true power of THz-pulse reflectometry. Because of the multiple layers of covering, it was necessary to isolate the THz-pulse reflected from the plaster interface with the embedded painting. More care was put into the signal processing to obtain the clearest THz image of "Vif Shapes," with the least influence from the "Face" layer. A centroid,

$$t_c = \frac{\int_{\Delta t} |E(t)|^2 t \, dt}{\int_{\Delta t} |E(t)|^2 \, dt} \qquad (42)$$

or weighted peak time, calculation of the pulse reflected from the plaster/paint/plaster interfaces better resolved the color domains of the painting, particularly the white and black pigments. The centroid takes advantage of the relative flatness of the top layer of plaster by using both the time-of-flight return of the reflected pulse and the pulse reflectivity and dispersion differences of each pigment. Since the mouth is the only feature of the face that was significantly thick (it had two layers of paint), it was the only pattern from the top layer to produce a "shadow" onto the second layer.

Figure V.16: Optical photograph of uncovered and covered sections of identical pairs of eyeglasses. Each section is 120 mm by 60 mm in dimension.

Another lab model consisted of two identical paintings of eyeglasses on a bi-color background—using white, black and yellow paints on a sand and plaster substrate (Figure V.16). The second pair of glasses was covered by a 6-mm-thick layer of the same plaster mixture. Figure V.17 shows the terahertz images of the painted layer obscured by

the plaster. They were each obtained from the gated time-domain signal such that only the pulse reflected from that layer was analyzed. In Figure V.17a, the peak-to-peak amplitude analysis revealed well-defined boundaries for the pigments, however, the two white sections do not have the same grey scale shading despite being the same pigment. This could be due to the paint for the lenses being applied more thickly than the paint below the glasses. Figure V.17b is an integration over the peak frequency of the spectrum +/-100 GHz. There is a higher contrast between the top and bottom pigments, as well as the black eyeglass frames. Again it is difficult to determine why the two white sections do not match. Figure V.17c utilizes a computation of the centroid time value of the pulse—which is dependent on the location, thickness and dispersive properties of the paint layer. In this case, there is better contrast between the black and lower white sections than between the black and yellow sections. The two white regions, however, are more closely matched than with the other two calculation methods. It may be useful to reconstruct calculated images after applying edge enhancing high pass FFT and wavelet filters, as in Figure V.17d. These filters help visually bring out the boundaries and textures of each section of the painting.
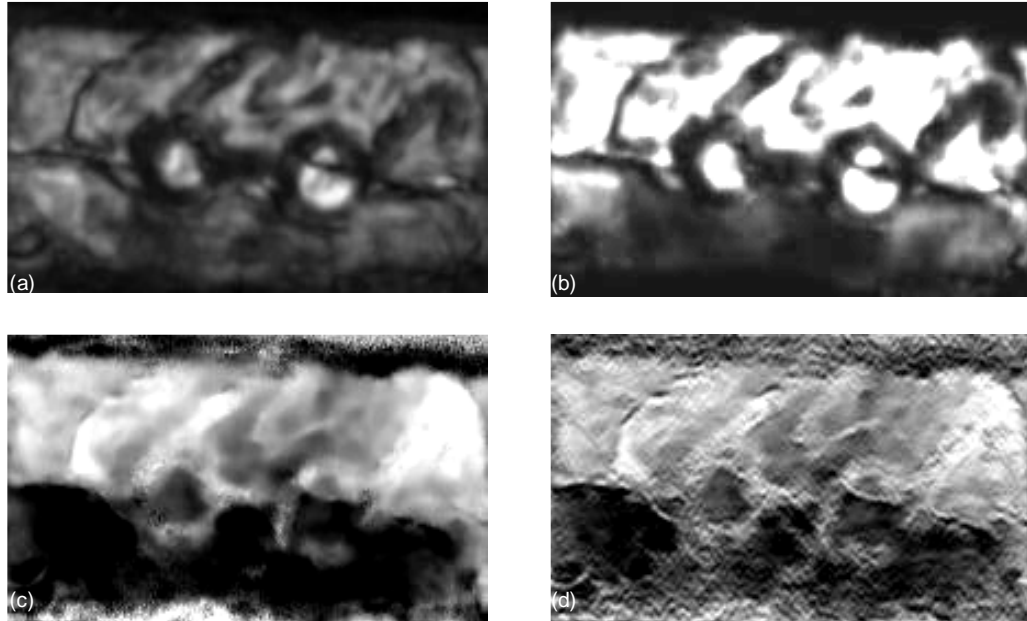
Figure V.17: THz images of the covered painting reveal the eyeglasses after processing the data via: (a) peak-to-peak amplitude comparison, (b) spectral integration, (c) time-domain centroid analysis and (d) spatial filtering and wavelet reconstruction of (c) (0.5 mm x 0.5 mm pixel size).

All three methods provide more information about the possible variety of pigments, however inconsistency in amplitudes between the two white domains suggests that absolute pigment identification may be prohibitive. Additional image-processing, such as the application of detail enhancing spatial filters and wavelet reconstruction—which removes noise from the image's high and low spatial frequencies—can visually enhance the color domain boundaries.

Section 5.04 - Terahertz Time-Domain Field Measurements of Wall Paintings

Figure V.18: Optical photographs of partially exposed fresco sections of L'Eglise de Saint Jean-Baptiste; (a) a wall in the nave between two archways and (b) wall section in the balcony area.
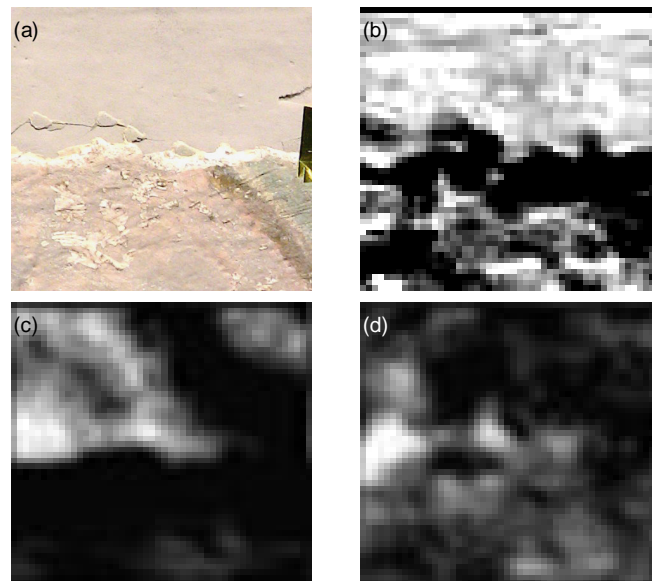
Figure V.19: Top: (a) optical photograph of Vif fresco section and THz images of covered section using (b) peak-to-peak amplitude; bottom: (c) time-domain centroid, and (d) spectral integration (Dimensions: 100 mm x 100 mm, 2 mm x 2 mm pixel size).

A portable THz-imaging system was then taken to L'Eglise de Saint Jean-Baptiste—a 9th century church in Vif, France—to inspect partially exposed frescoes (Figure V.18) and complete the investigation of frescoes

with pulsed THz technology. The frescoes had been covered with multiple layers of plaster and paint over the course of several centuries—as treatments for aging, weather and fire damage and one change of style. The pictured frescoes were discovered through cracks and crumbling of the wall. However, because of the uniqueness of each layer, it is desirable to nondestructively determine which obscured paintings are in the best conditions and most historically interesting before proceeding to remove plaster from unexposed areas of the church.

The section of fresco in the field study consisted of an exposed light grey semi-circle, and brown and green arcs—the shapes of which extended beneath multiple, non-uniform layers of coarse plaster, smooth plaster, and paint (Figure V.19a). Figure V.19b represents the largest peak-to-peak amplitude of the overall reflected signal. Hence, only the top-most paint layer of the plastered section is visible. The exposed grey color domain is clearly distinguishable, with the brown and green domains having less distinctive boundaries. Figure V.19c uses the centroid calculation of the pulse reflected from the fresco layer, revealing the extension of the semi-circle beneath the covering. It is uncertain whether the light region in the upper right corner represents a new color domain or a possible layer defect, since the centroid is dependent on both the dispersion of the pulse and location of the interface. In Figure V.19d, the spectral integration of the time window—expanded to include the reflection from the exposed fresco—reveals the continuation of the grey, semi-

circular pattern beneath and across the plaster boundary. No further information is revealed about the upper right corner.

Section 5.05 - Other Applications of Terahertz Reflection Imaging in Art
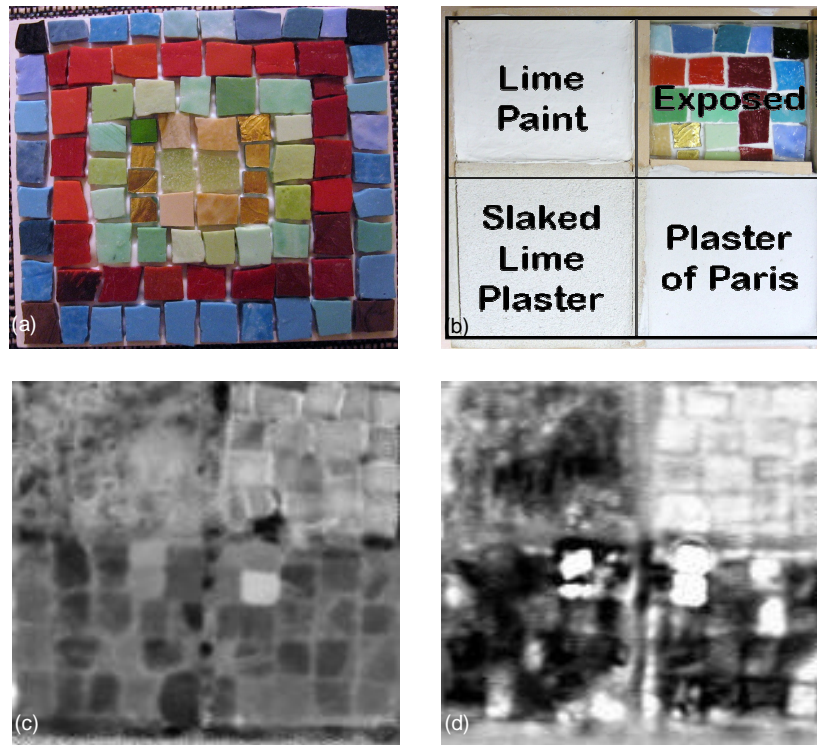
Figure V.20: Top: Optical photographs of (a) uncovered mosaic pattern and (b) sectioned and covered mosaic; Bottom: Terahertz images using (c) time-domain centroid and (d) 0.05-0.10 THz amplitude integration on pulse reflected from plaster/tile interface (Dimensions: 130 mm x 130 mm sample and 1 mm x 1 mm pixel size).

Preliminary experiments have been done to apply the knowledge gained from studying obscured paintings to studying mosaics, which like frescoes, have occasionally been covered to due degradation and changes in religion or politics. Mosaics consist of flat, colored tiles cemented to a substrate in a colorful pattern. A model was produced using traditionally colored Smalti glass tiles cemented to a wooden panel.

99

The spaces between the tiles were filled with calcium carbonate and silica-based grout. The mosaic (Figure V.20a) was then divided into four equal sections. One section was left empty, while the other three were covered with 5 mm of lime paint with sand, slake lime plaster with sand and plaster of Paris (Figure V.20b). Figure V.20c shows a time-domain centroid image of the pulse reflected from the tile/plaster interface. The lime paint mixture is highly absorbing and becomes nearly opaque at 5mm thickness. The slaked lime and plaster of Paris mixtures, however, are transparent and the tile can be clearly resolved (though not entirely consistently with tile color). The spectral image resolves many of the tiles, but it is not apparent that the tile colors can be spectrally distinguished from each other. It would be desirable to do a more systematic study of the tiles and the pigments used to color them.

Section 5.06 - Conclusion

A spectroscopic study of pigments, plasters and other artistic media, will provide art historians and conservators with a dramatic improvement in investigative techniques. The ability to isolate interface reflections propagating through optically dense or opaque media, as well as the ability to distinguish reflections from different color domains, demonstrates that Terahertz ranging and imaging have great potential for analysis of mural paintings in a completely non-invasive manner.

Terahertz-pulse reflectometry is found to have potential as a useful tool for the nondestructive imaging of obscured fresco paintings, although

complete image extraction may require multiple image-processing calculation methods. Spectral information may not be enough to identify individual pigments, increasingly sophisticated image-processing techniques (such as overlays or pattern recognition) may reveal the complete picture.

CHAPTER VI: CONCLUSIONS

Section 6.01 - Summary

Terahertz time-domain reflectometry was determined to be a robust tool for the nondestructive evaluation of multilayered systems of materials. It exploits the time-of-flight and material dependent spectral reflectivity of the pulsed terahertz electric field at material interfaces in order to obtain single point and image data that provide information about the thickness, composition and structure of the surface and hidden layers. THz-TDR has advantages over several other continuous wave and pulsed optical NDE techniques presented because of its penetration depth and lower absorption and scattering loss, in addition to wide spectral bandwidth. It has better axial and lateral spatial resolution than microwave radar imaging. Compared to x-ray NDE methods, THz-TDR has better depth resolution than scattering methods and does not require 360° access, unlike 3D tomography.

Thermal protection systems were investigated in order to develop systematic THz-TDR techniques to monitor the thicknesses and conditions of ceramic coatings and native and thermally grown oxides, in an effort to predict system failure. Terahertz properties of YSZ ceramic coatings were determined, including refractive index.   The YSZ thickness were resolvable within 10 μm of microscopically determined measurments.

Three methods for monitoring TGO growth were proposed. A 5 μm minimum thickness of TGO is required to be directly measurable using ranging, based on standard measurement error. However, the relative peak amplitude monitoring method shows a reliable decrease with increasing TGO growth. Spectral centroid imaging showed early promise for large area monitoring of TGO growth. Tomographic imaging can laterally resolve defect features of at least 50 μm

Several wood specimen were investigated using terahertz time-domain reflectometry. Tree-rings measured parallel to growth using ranging had limited penetration, but statistically consistent depth resolution. Tree-rings imaged perpendicular to growth were spatially resolvable using tomography, with statistically moderate accuracy, while fully exposed and under layers of varnish, paint and primer. There is promise that THz-TDR will be useful for the dendrochronological cross-dating of wood panel paintings.

Artist's media and multilayer drawings, fresco paintings, and mosaics were investigated using terahertz time-domain reflectometry. The spectral dielectric properties of several paint pigments and sketch materials were obtained and spectroscopic regions of interest were determined in order to aid in their identification in multi-spectral images of artworks. THz-pulse ranging and spectroscopic imaging techniques were utilized in order to resolve sketches, paintings and tiles embedded beneath both paint and plaster. The quality of the imaged art were

dependent on the contrast of the spectral responses of the media with respect to each other and the immediately adjacent layers, as well as absorption and scattering losses in the covering layers. Image quality can be enhanced with signal and image-processing methods, in addition to terahertz system improvements.

Section 6.02 - Future Work

Several improvements to the terahertz system are being considered in order to improve the quality of the terahertz time-domain reflectometry measurements. Modifications that would decrease the THz-pulse width and broaden the spectral bandwidth, while maintaining high terahertz probe power and signal to noise, are being considered. Among them include the development of a fiber-coupled electro-optic terahertz transceiver. This would possibly have wider spectral bandwidth, saturation-less power scaling, and compatibility with charge-coupled device (CCD) detection—which enables faster large-area measurements.

Future data acquisition and motion control advances would include faster rate variable optical delays to decrease acquisition time and increase pixel waveform averaging (for increased dynamic range). It is also necessary to optimize the measurement quality while measuring targets with non-uniform and curved surfaces. Three dimensional terahertz computed tomography in the reflection geometry—which is significantly more complex than in transmission—should be explored. However, intelligent motion control combined with real-time image-

processing would achieve adaptive automated data acquisition that would be more beneficial in situations where only planar measurements are possible.

Continued investigation of thermal barrier coatings using THz-TDR should evolve in two ways: material system conditions and measurement analysis techniques. More systematic measurements of APS and EBPVD thermal barrier systems should be performed after they are thermally-cycled until failure. The changes in the dielectric properties of the system should be studied as it is sintered—in order to determine temperature dependencies—and serviced—in order to determine contamination effects. A study of ceramic coatings other than YSZ, as well as the effects of bond coat preparation and surface curvature, should be performed. The analytical methods proposed in this thesis should be applied to these measurements, for comparison, and a reliable failure prediction algorithm should be developed taking these conditions into consideration.

The THz-TDR measurements of wood presented in this thesis were very preliminary, therefore there are many options for further exploration that include and go beyond dendrochronological applications. For tree-ring crossdating, a thorough study comparing b-scan and lateral image measurements to tree-ring databases must be performed. THz-TDR may be used to study stress and fatigue in wood as it ages or responds to external forces, by taking advantage of the polarization-dependent

birefringence of wood. It may also be used to assess water content or damage in artifacts and artwork.

Since the ultimate goal of nondestructive evaluation measurements in art conservation is to extract information that will aid in the contextualization, preservation, and restoration of artifacts, the door is wide open for further exploration. A complete database of the terahertz properties of pigments, dyes, binding media, varnishes, substrates and other commonly used art materials is necessary for the full terahertz spectral range. This will promote the identification of composition using principle component analysis. Multilayered systems that can be investigated include cave paintings and other environmentally-damaged archeological sites, oxidized metalwork, fragile objects (manuscripts, tapestries, etc.) and enclosed objects (coffins, pottery, etc.).

APPENDICES

Appendix I: Pigments Details [120]

Pigments combined with water applied on thin polyester cloth

Cinnabar
Lead Tin Yellow
Lead White
Bianco SanGiovanni

Goethite
Sienna
Burnt Sienna
Red Ochre
Cold Hematite
Hematite

Malachite
Glauconite
Yellow Ochre 1

Yellow Ochre 2

Carbon Black
Pyrolusite
Shungite

Vivianite
Lapis Lazuli
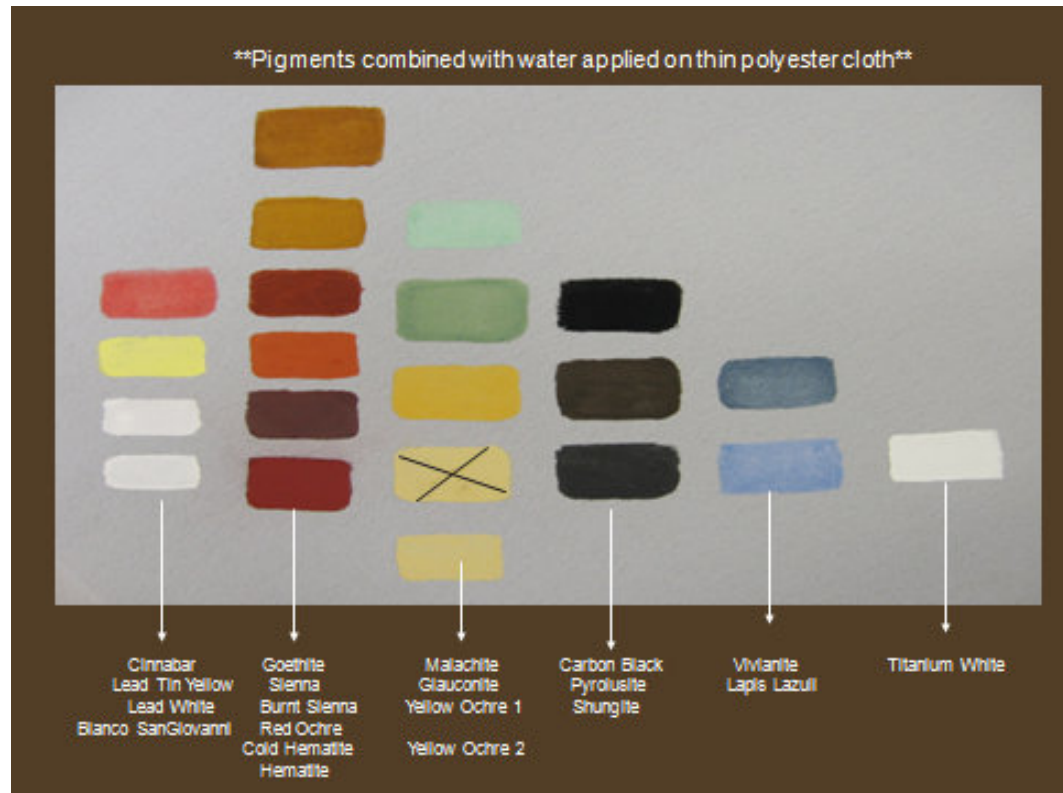
Titanium White

Titanium dioxide white pigments are developments of the 20th century, and because of their high hiding power, nontoxic nature, and reasonable cost, they have eclipsed other traditional white pigments. Anatase and rutile are naturally occurring mineral forms of titanium dioxide that synthesized as pigments.

Mixed black is a mixture of Lamp Black and Mars Black. Lamp Black was produced originally by burning vegetable oils, but these days by burning tar, creosote, naphthalene, or other petroleum products. Lamp Black is the oldest pigment made by a deliberate industrial process. It's origin presumably was after the development of oil lamps and by early Egyptian times was the black of choice as it was a more intense and pure black than charcoal, and is the black found in all Egyptian murals and tomb decorations. it is one of the slowest drying pigments in oil and should never be used underneath other colors unless mixed with a fast drier such as Umber. produces a very soft and brittle oil paint. While Lamp Black has a long and honorable history, most artists prefer either Ivory Black or the newer Mars Black for most purposes. It was the only black pigment that

could be used in Fresco at one time, but even for that purpose Mars Black is superior. Mars Black is an inorganic synthetic iron oxide. Closely related chemically to the coloring agents in the naturally occurring red and yellow earths, Mars Black is nevertheless recent in origin, being developed early in the 20th century. It is normally the only black available in acrylics ranges because Ivory Black is is less successful in acrylic than oils, however oil painters could benefit from using this excellent pigment. It is the only major black pigment that is considered non-toxic, the only one that is a good drier, the only one safe to over paint because it is the only one that produces a hard fairly flexible oil paint, and is the only one that can be used in all media without reservation. It is dense and opaque with a warmish brown undertone.

Malachite (azurite) is a carbonate mineral, copper(II) carbonate hydroxide $Cu_2CO_3(OH)_2$. It crystallizes in the monoclinic crystal system, and most often forms botryoidal, fibrous, or stalagmitic masses. Individual crystals are rare, but do occur as slender to acicular prisms. Pseudomorphs after more tabular or blocky azurite crystals also occur.

Lazurite is Sodium Calcium Aluminum Silicate Sulfate, a tectosilicate mineral with sulfate, sulfur and chloride with formula: $(Na,Ca)_8(AlSiO_4)_6(SO_4,S,Cl)_2$. It is a feldspathoid and a member of the sodalite group. Lazurite crystallizes in the isometric system although well formed crystals are rare. It is usually massive and forms the bulk of the gemstone lapis lazuli. Lazurite is a deep blue to greenish blue.

Glauconite is a phyllosilicate (mica group) mineral of formula: (K,Na)(Fe3+,Al,Mg)2(Si,Al)4O10(OH)2. It can also be referred to as a Hydrated Iron Potassium Silicate. It crystallizes with monoclinic geometry. The name is derived from the Greek glaucos (γλαυκος) meaning 'gleaming' or 'silvery', to describe the appearance of the blue-green color, presumably relating to the sheen and blue-green colour of the sea's surface. Its color ranges from olive green, black green to bluish green. It is probably the result of the iron content of the mineral. In the Mohs scale it has hardness of 2. The relative density range is 2.2 - 2.8. It is normally found in dark green rounded nodules of sand size dimension. It can be confused with chlorite or with some clays. Glauconite has long been used in Europe as an artistic oil paint, especially in Russian "icon paintings". It is rated as a highly permanent pigment, and often marketed by the names "terre verte" or "green earth".

Goethite (brown ochre), is Hydrated Iron Oxide mineral, $\alpha\text{-}FeO^{3+}(OH)$, found in soil and other low temperature environments. Goethite has been well known since prehistoric times for its use as a pigment. Evidence has been found of its use in paint pigment samples taken from the caves of Lascaux in France. It is an iron oxide-hydroxide with a chemical formula

FeOOH. The hydroxylation (heating to the point of dehydration) of goethite produces hematite. It forms prismatic needle-like crystals, but is more typically massive. Its main modern use is as an iron ore, being referred to as *brown iron ore*. It does have some use as a clay earth pigment.

Hematite is the mineral form of Iron(III) oxide, (Fe_2O_3), one of several iron oxides. Hematite crystallizes in the rhombohedral system, and it has the same crystal structure as limonite and as corundum. Hematite and limonite form a complete solid solution at temperatures above 950°C. Hematite is a very common mineral, colored black to steel or silver-gray, brown to reddish brown, or red. It is mined as the main ore of iron. Varieties include kidney ore, martite (pseudomorphs after magnetite), iron rose and *specularite* (specular hematite). While the forms of hematite vary, they all have a rust-red streak. Hematite is harder than pure iron, but much more brittle. Hematite is a ferric oxide native earth and the principle coloring agent in red ochre, such as Indian Red, Terra Pozzuoli, Venetian Red, etc. These pigments are basically hematite associated with varying proportions of mineral impurities such as clay, chalk and silica. They differ from yellow ochre and brown ochre in that they do not contain water. In other words, the iron to which they owe their color is iron oxide not hydrated iron oxide. The hematite pigment we make is a deep red hue.

Caput mortem (Cold Hematite) is the name given to a purple variety of iron oxide pigment, an "earth color". It is used in oil paints and paper dyes. The name for this pigment may have come from the alchemical usage, since iron oxide (rust) is the useless residue of oxidization. It is the name of a brownish paint that was originally made from the wrappings of mummies. It was most popular in the 1600s. It was suddenly discontinued in the early 19th century when its composition became generally known to artists [The Artist's Handbook, p. 52]. In recent years, it has been made with iron sulphate and impurities obtained from the residues of the distillation of scisti piritosi in the fabrication of sulphuric acid. Cold Hematite is a ferric oxide native earth and the principle coloring agent in red ochre, such as Indian Red, Terra Pozzuoli, Venetian Red, etc. These pigments are basically hematite associated with varying proportions of mineral impurities such as clay, chalk and silica. In the case of Caput Mortum, small amounts of iron sulfate and other impurities are usually associated with hematite, giving it the deep violet hue. The Cold Hematite pigment we make is a dark reddish purple.

Red ochre and **Gold ochre** are pigments made from naturally tinted clay. It has been used worldwide since prehistoric times. Chemically, it is hydrated iron (III) oxide. Ochre is a natural earth containing clay tinted by hydrated iron oxide and is composed of a naturally calcined form of limonite and goethite, and traces of gypsum or manganese carbonate. Limonite is a general term used to describe all forms of hydrated iron oxide minerals ($FeO(OH)$) that occur as natural clay or earth. Limonite includes the minerals goethite, akaganeite and lepidocrocite. To be considered an ochre, the content of iron oxide must not be less than 12%. Depending upon the content of hydrated iron oxide, the color of ochre varies from light yellow to orange-red. Most yellow ochre are normally not calcined as heat does relatively little to alter their color. Like red iron oxides (hematite), they are found around the world and have been used as pigments since prehistory. French ochre, historically one of the best grades of limonite, contains about 20% iron oxide and is high in silica.

Sienna is a form of limonite clay most famous in the production of oil paint pigments. Its yellow-brown colour comes from ferric oxides contained within. As a natural pigment, it (along with its chemical cousins ochre and umber) was one of the first pigments to be used by humans, and is found in many cave paintings. Limonite is an ore consisting in a mixture of hydrated iron(III) oxide-hydroxide of varying composition. The generic formula is frequently written as $FeO(OH) \cdot nH2O$, although this is not entirely accurate as limonite often contains a varying amount of oxide compared to hydroxide. Burnt sienna is an ochre with a high iron oxide content. Unlike yellow ochres, which generally are opaque, siennas are more translucent. When a limonite, like sienna, is calcined (roasted) at high temperatures, its water content (hydration) is eliminated and it becomes a hematite (anhydrous), or burnt sienna. However, our burnt sienna is naturally calcined, or rather it is composed of a greater amount of hematite. Sienna is hydrated iron oxide closely resembling yellow ochre (See Gold Ochre) by its composition.. The differences in color between ochre and sienna, is most likely due to the degree of hydration, or quantity of water bonded to its ferric oxide content. These pigments are basically composed of the minerals goethite and hematite associated with varying proportions of mineral impurities such as clay, chalk and silica. The roasting or calcination of raw sienna produces a very great change in its hue as well as in the depth of its color. The iron oxide becomes converted to iron oxide, this change being accompanied by a great increase in the translucency and depth of the color. Our burnt sienna is

naturally calcined or rather composed of a greater quantity of hematite (iron oxide) rather than goethite (hydrated iron oxide) like raw sienna.

Vivianite $Fe_3(PO_4)_2 \cdot 8(H_2O)$, hydrated iron phosphate, is a secondary mineral found in a number of geological environments. Usually found as deep blue to deep bluish green prismatic to flattened crystals, most crystals rather small to microscopic, larger ones are rare. Our vivianite comes from bogs around the Moscow region, and has a dark blue masstone, similar to indigo, with a reddish blue undertone.

Shungite is an amorphous variety of graphite of intense black color, which outwardly resembles anthracite. Shungite is unique in its composition, structure and properties. It is a natural composite with a homogeneous distribution of crystalline silicate particles in a carbon matrix.

Bianco di San Giovanni is lime white pigment first described in literature by Cennino Cennini. He does not explain the name used for this lime white, and it is probable therefore, this important white pigment was in use by artists before Cennini's time. D. V. Thompson says it gets its name after the patron saint of Florence. Bianco di San Giovanni is a pigment of inorganic, natural mineral origin from limestone (*calcium carbonate*) deposits. Not to be confused with simple lime white or chalk, Bianco di San Giovanni, as Cennino Cennini reports, is dried lime which is reduced to powder and then *immersed in the water* for eight days that is changed each day. It is then made into small cakes that are left to dry in the sun. It is then grounded finely. Bianco di San Giovanni is considered the white pigment par excellence for fresco painting. It is used also in tempera and grounds while it is not advised in oil and encaustic painting techniques.

Cinnabar is a red crystalline form of mercuric sulfide (HgS), a red mineral of secondary origin, occurring in the oxidized zones of copper veins. Cinnabar has the highest refractive index of any other known mineral, its mean index for sodium light being 3.256, while the index for diamond—a substance of remarkable refraction—is only 2.42. It was mined by the Romans for its mercury content and it has been the main ore of mercury throughout the centuries. Some mines used by the Romans are still being mined today. Cinnabar is found in all localities which yield mercury notably Almaden, Spain; Idrija, Slovenia; Landsberg, near Ober-Moschel in the Palatinate; Ripa, at the foot of the Apuan Alps, Tuscany; the mountain Avala, Serbia; Huancavelica, Peru; Kweichow and Hunan Provinces, China; Doneckaia region, Ukraine; and California, Oregon, Texas, and Arkansas, USA.

White lead is the most important of all the lead pigments; it is basic carbonate of lead, $2PbCO_3 Pb(OH)_2$, and usually contains about 70 percent of lead carbonate and 30 percent of lead hydrate. Although lead carbonate occurs in nature as the mineral, cerussite, it has not been an important source of white pigment. Lead white is the most important of all lead pigments and, not overlooking special uses of lime white in wall painting, it is safe to say that, historically, it is the most important of all white pigments. It was the only white pigment used in European easel painting until the 19th century. It has been produced since early historical times. Theophrastus, Pliny, and Vitruvius all described its preparation from metallic lead and vinegar. It is one of the oldest synthetically produced pigments. It can also be used in encaustic (wax) technique, but does not appear to perform well in true fresco technique.

Appendix II: Terahertz Spectra of Pigments
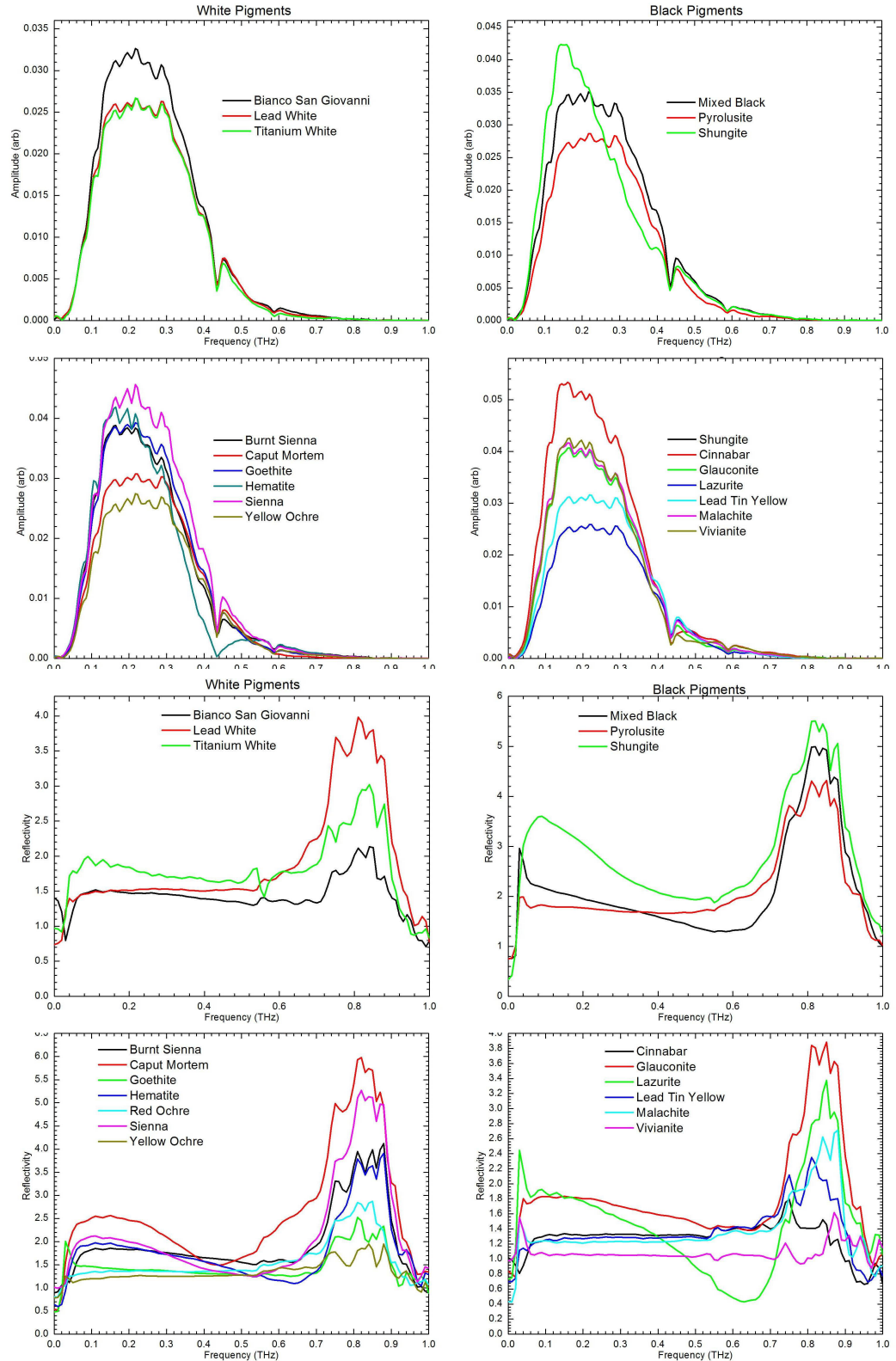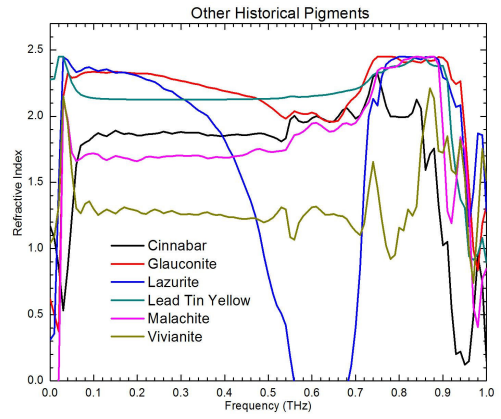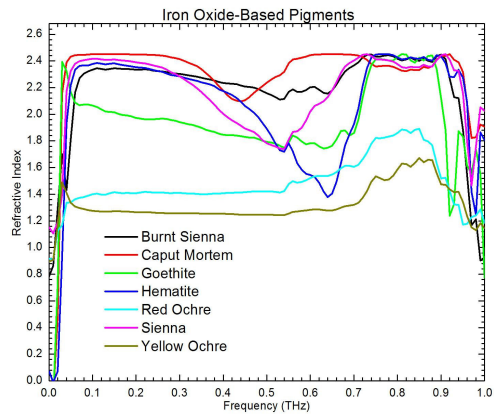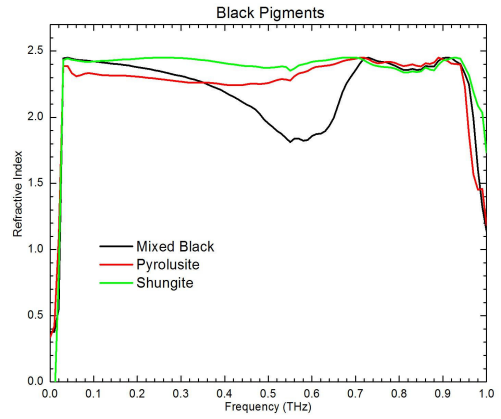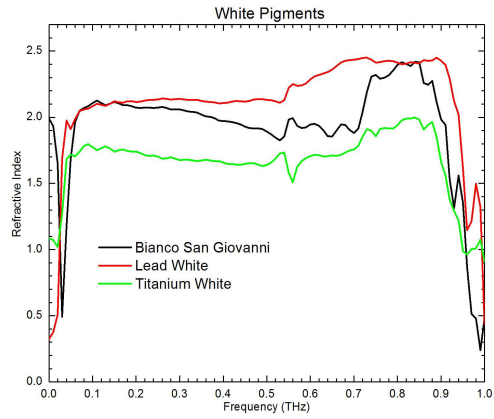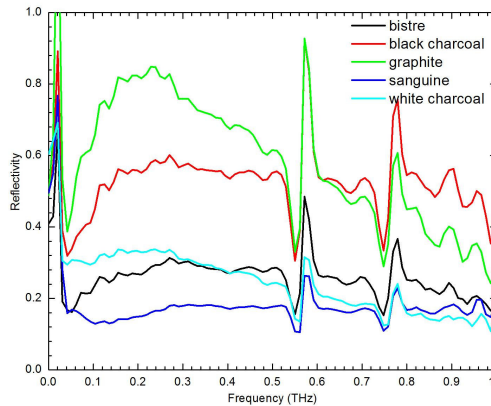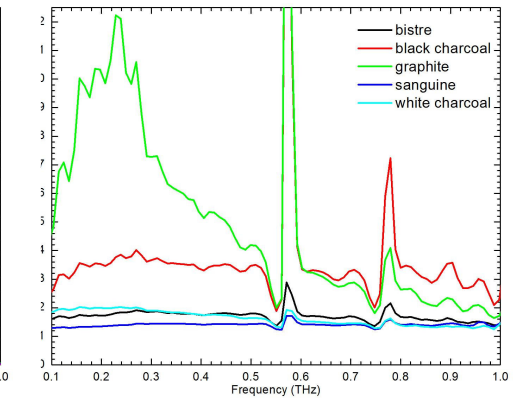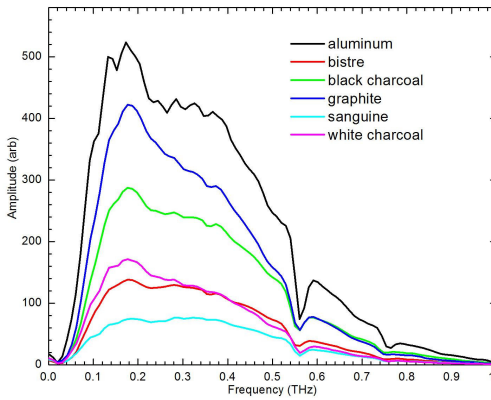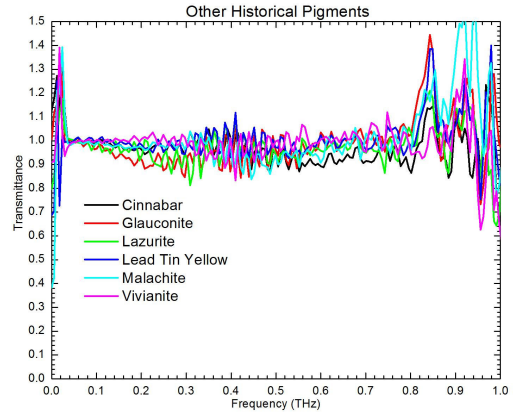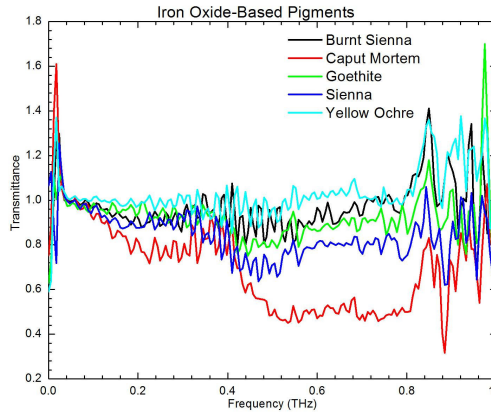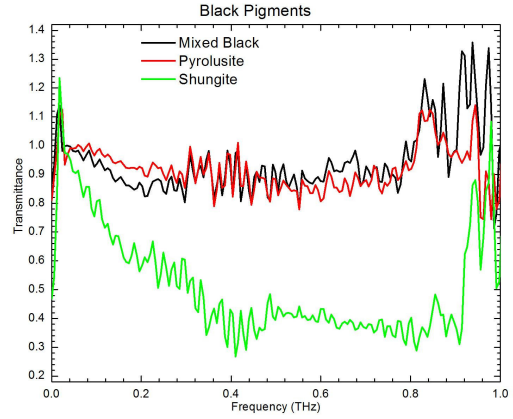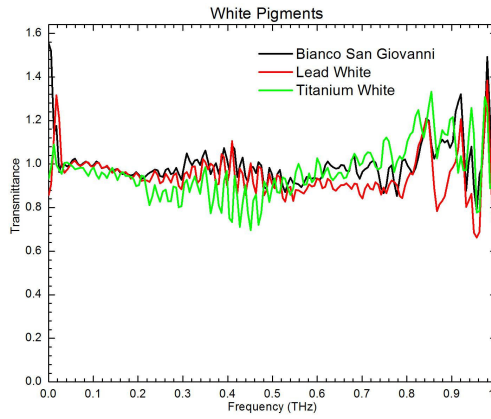
Appendix III: Labview™ Code
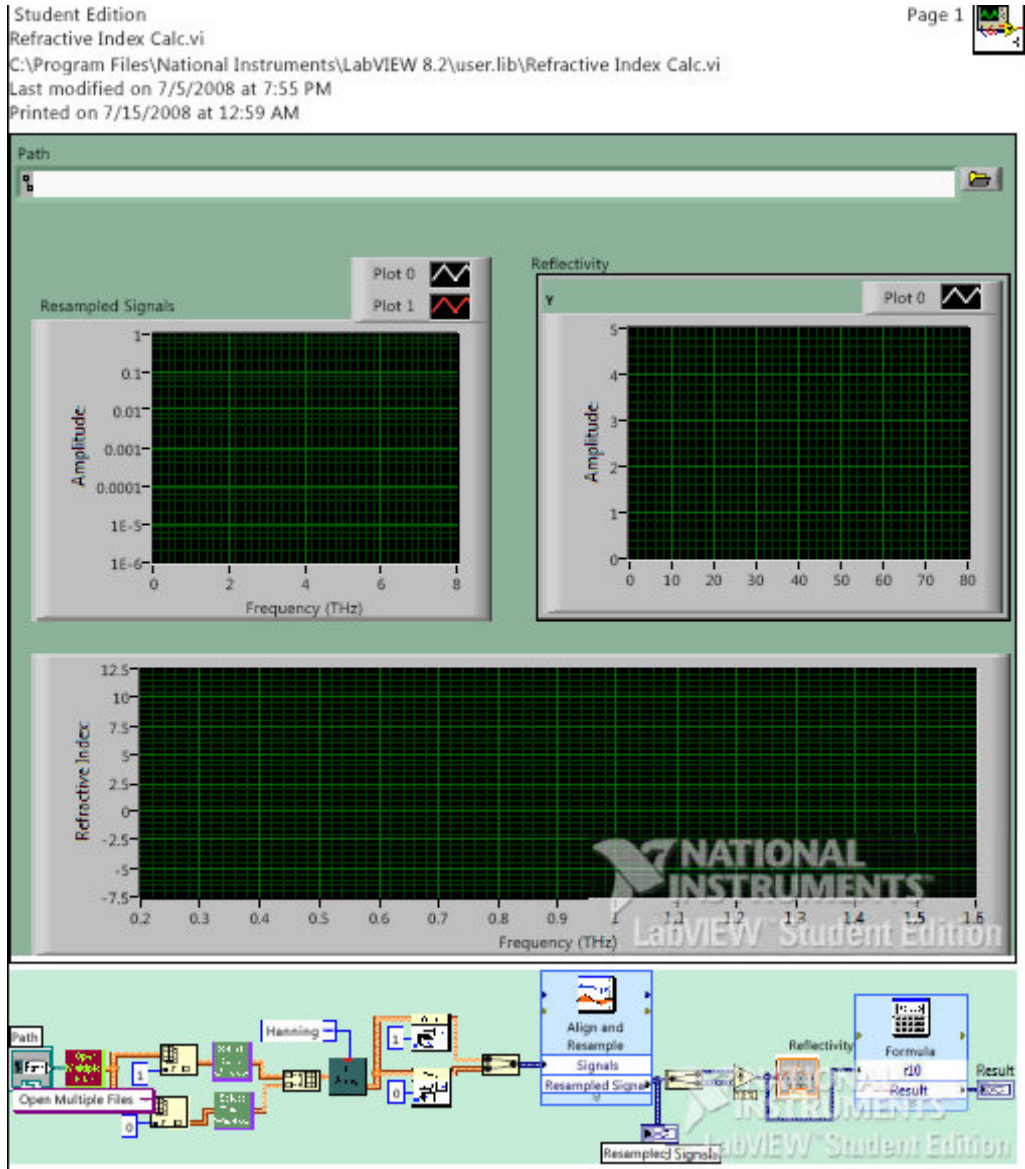
Student Edition   Page 1
Refractive Index Calc.vi
C:\Program Files\National Instruments\LabVIEW 8.2\user.lib\Refractive Index Calc.vi
Last modified on 7/5/2008 at 7:55 PM
Printed on 7/15/2008 at 12:59 AM

Student Edition
Refractive Index Calc.vi
C:\Program Files\National Instruments\LabVIEW 8.2\user.lib\Refractive Index Calc.vi
Last modified on 7/5/2008 at 7:55 PM
Printed on 7/15/2008 at 12:59 AM

Page 2

Formula

Formula

Uses a calculator interface to create mathematical formulas. You can use this Express VI to perform most math functions that a basic scientific calculator can compute.

This Express VI is configured as follows:

Formula: (r10+1)/(1-r10)

Open Multiple Files.vi

C:\Program Files\National Instruments\LabVIEW 8.2\user.lib\Open Multiple Files.vi

Open Multiple Files (Poly).vi

C:\Program Files\National Instruments\LabVIEW 8.2\user.lib\Open Multiple Files (Poly).vi

Select Time Window.vi

C:\Program Files\National Instruments\LabVIEW 8.2\user.lib\Select Time Window.vi

Select Time Window Single.vi

C:\Program Files\National Instruments\LabVIEW 8.2\user.lib\Select Time Window Single.vi

Align and Resample

Align and Resample

Performs an alignment of signals by changing the start time or performs a resampling of signals by changing the time delta. This Express VI returns the adjusted signals.

This Express VI is configured as follows:

Acquisition Type: Single segment
Alignment Interval: Common
Resample: Lowest dt
Resampling Interplation Mode: Linear
Open Interval: Open Interval

WDT Index Channel DBL.vi

C:\Program Files\National Instruments\LabVIEW 8.2\vi.lib\Waveform\WDTOps.llb\WDT Index Channel DBL.vi

Index Waveform Array.vi

C:\Program Files\National Instruments\LabVIEW 8.2\vi.lib\Waveform\WDTOps.llb\Index Waveform Array.vi

FD Waveform Array.vi

C:\Program Files\National Instruments\LabVIEW 8.2\user.lib\FD Waveform Array.vi

Student Edition
Open Multiple Files.vi
C:\Program Files\National Instruments\LabVIEW 8.2\user.lib\Open Multiple Files.vi
Last modified on 7/5/2008 at 8:41 PM
Printed on 7/15/2008 at 12:59 AM

Page 1

Path

pattern label

*.txt

selected paths

0

Array

54

Y

Pict 0

Amplitude

60 —
50 —
40 —
30 —
20 —
10 —
0 —
-10 —
-20 —
-30 —
-40 —
-50 —
-60 —

0   100   200   300   400   500   600   700   800   900   1000

Student Edition
Open Multiple Files (Poly).vi
C:\Program Files\National Instruments\LabVIEW 8.2\user.lib\Open Multiple Files (Poly).vi
Last modified on 4/9/2008 at 3:08 PM
Printed on 7/15/2008 at 12:59 AM

Page 1

Open Multiple Files.vi
C:\Program Files\National Instruments\LabVIEW 8.2\user.lib\Open Multiple Files.vi

Open Multiple NASA Files.vi
C:\Program Files\National Instruments\LabVIEW 8.2\user.lib\Open Multiple NASA Files.vi

Student Edition
Open Multiple Files.vi
C:\Program Files\National Instruments\LabVIEW 8.2\user.lib\Open Multiple Files.vi
Last modified on 7/5/2008 at 8:41 PM
Printed on 7/15/2008 at 12:59 AM

Page 2

File Dialog

File Dialog

Displays a dialog box with which you can specify the path to a file or directory.

This Express VI is configured as follows:

Selection Mode:
Multi-select

Read From Spreadsheet File (DBL).vi

C:\Program Files\National Instruments\LabVIEW 8.2\vi.lib\Utility\file.llb\Read From Spreadsheet File (DBL).vi

Read From Spreadsheet File.vi

C:\Program Files\National Instruments\LabVIEW 8.2\vi.lib\Utility\file.llb\Read From Spreadsheet File.vi

Student Edition
Open Multiple Files (Poly).vi
C:\Program Files\National Instruments\LabVIEW 8.2\user.lib\Open Multiple Files (Poly).vi
Last modified on 4/9/2008 at 3:08 PM
Printed on 7/15/2008 at 12:59 AM

Page 1

Open Multiple Files.vi

C:\Program Files\National Instruments\LabVIEW 8.2\user.lib\Open Multiple Files.vi

Open Multiple NASA Files.vi

C:\Program Files\National Instruments\LabVIEW 8.2\user.lib\Open Multiple NASA Files.vi

Student Edition
Open Multiple NASA Files.vi
C:\Program Files\National Instruments\LabVIEW 8.2\user.lib\Open Multiple NASA Files.vi
Last modified on 4/29/2008 at 11:13 PM
Printed on 7/15/2008 at 12:59 AM

Page 1

Student Edition
Open Multiple NASA Files.vi
C:\Program Files\National Instruments\LabVIEW 8.2\user.lib\Open Multiple NASA Files.vi
Last modified on 4/29/2008 at 11:13 PM
Printed on 7/15/2008 at 12:59 AM

Page 2

File Dialog
File Dialog
Displays a dialog box with which you can specify the path to a file or directory.

This Express VI is configured as follows:

Selection Mode:
Multi-select

Open NASA File.vi
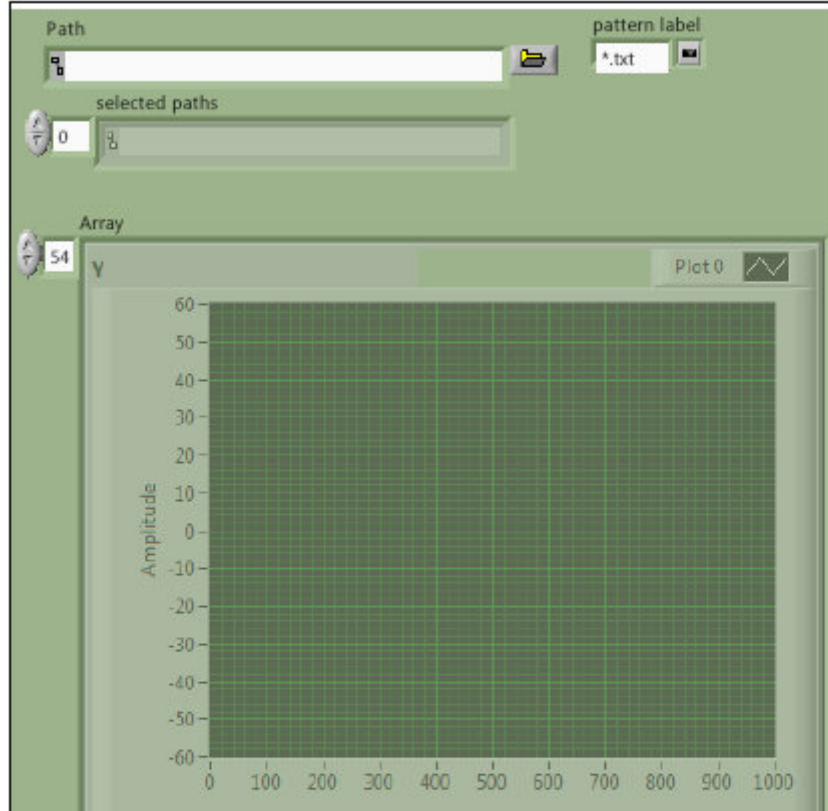C:\Program Files\National Instruments\LabVIEW 8.2\user.lib\Open NASA File.vi

Student Edition
Open NASA File.vi
C:\Program Files\National Instruments\LabVIEW 8.2\user.lib\Open NASA File.vi
Last modified on 4/29/2008 at 11:11 PM
Printed on 7/15/2008 at 12:59 AM
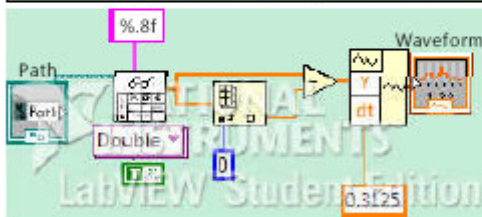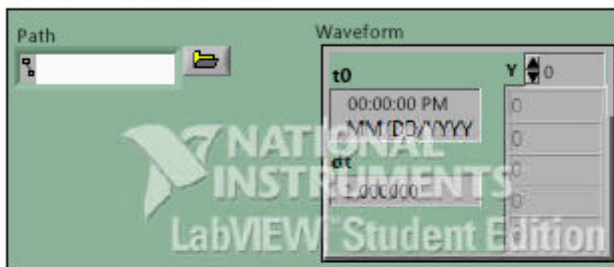
Page 1

Read From Spreadsheet File.vi
C:\Program Files\National Instruments\LabVIEW 8.2\vi.lib\Utility\file.llb\Read From Spreadsheet File.vi

Read From Spreadsheet File (DBL).vi
C:\Program Files\National Instruments\LabVIEW 8.2\vi.lib\Utility\file.llb\Read From Spreadsheet File (DBL).vi

Select Time Window.vi
C:\Program Files\National Instruments\LabVIEW 8.2\user.lib\Select Time Window.vi
Last modified on 7/3/2008 at 3:59 PM
Printed on 7/15/2008 at 12:59 AM

Select Time Window Array.vi
C:\Program Files\National Instruments\LabVIEW 8.2\user.lib\Select Time Window Array.vi

Select Time Window Single.vi
C:\Program Files\National Instruments\LabVIEW 8.2\user.lib\Select Time Window Single.vi

Select Time Window Array.vi
C:\Program Files\National Instruments\LabVIEW 8.2\user.lib\Select Time Window Array.vi
Last modified on 7/5/2008 at 9:32 PM
Printed on 7/15/2008 at 12:59 AM

Student Edition
Select Time Window Array.vi
C:\Program Files\National Instruments\LabVIEW 8.2\user.lib\Select Time Window Array.vi
Last modified on 7/5/2008 at 9:32 PM
Printed on 7/15/2008 at 12:59 AM

Page 2
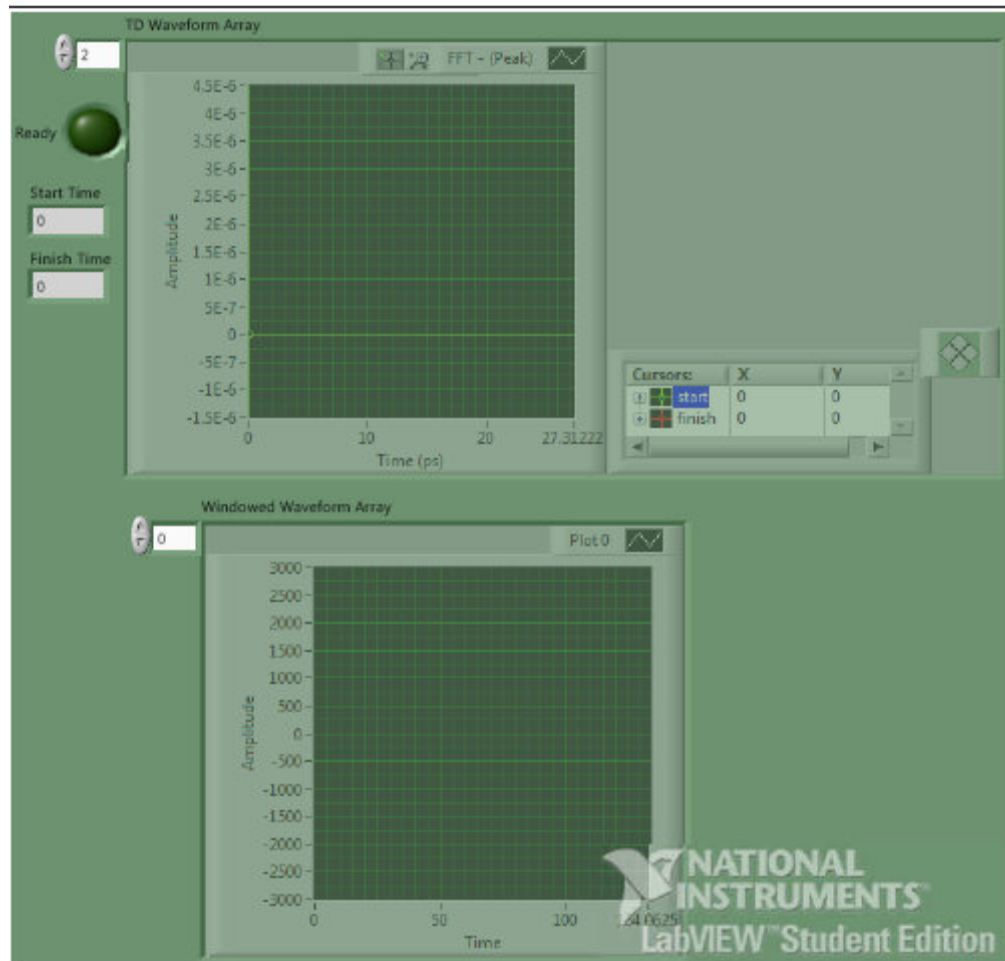
WDT Get Waveform Subset DBL.vi
C:\Program Files\National Instruments\LabVIEW 8.2\vi.lib\Waveform\WDTOps.llb\WDT Get Waveform Subset DBL.vi

Get Waveform Subset.vi
C:\Program Files\National Instruments\LabVIEW 8.2\vi.lib\Waveform\WDTOps.llb\Get Waveform Subset.vi

Play Sound File.vi
C:\Program Files\National Instruments\LabVIEW 8.2\vi.lib\sound2\lvsound2.llb\Play Sound File.vi

124

Select Time Window Single.vi
C:\Program Files\National Instruments\LabVIEW 8.2\user.lib\Select Time Window Single.vi
Last modified on 7/5/2008 at 8:48 PM
Printed on 7/15/2008 at 12:59 AM

Play Sound File.vi
C:\Program Files\National Instruments\LabVIEW 8.2\vi.lib\sound2\lvsound2.llb\Play Sound File.vi

Select Time Window Single.vi
C:\Program Files\National Instruments\LabVIEW 8.2\user.lib\Select Time Window Single.vi
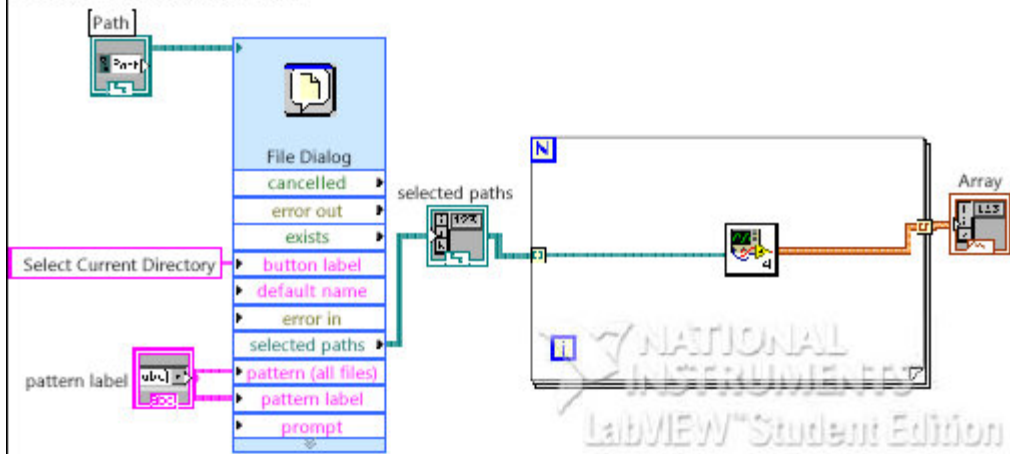Last modified on 7/5/2008 at 8:48 PM
Printed on 7/15/2008 at 12:59 AM

Get Waveform Subset.vi
C:\Program Files\National Instruments\LabVIEW 8.2\vi.lib\Waveform\WDTOps.llb\Get Waveform Subset.vi

WDT Get Waveform Subset DBL.vi
C:\Program Files\National Instruments\LabVIEW 8.2\vi.lib\Waveform\WDTOps.llb\WDT Get Waveform Subset DBL.vi

125

Student Edition
FD Waveform Array.vi
C:\Program Files\National Instruments\LabVIEW 8.2\user.lib\FD Waveform Array.vi
Last modified on 7/7/2008 at 9:23 AM
Printed on 7/15/2008 at 12:59 AM

Page 1

Student Edition
FD Waveform Array.vi
C:\Program Files\National Instruments\LabVIEW 8.2\user.lib\FD Waveform Array.vi
Last modified on 7/7/2008 at 9:23 AM
Printed on 7/15/2008 at 12:59 AM

Page 2
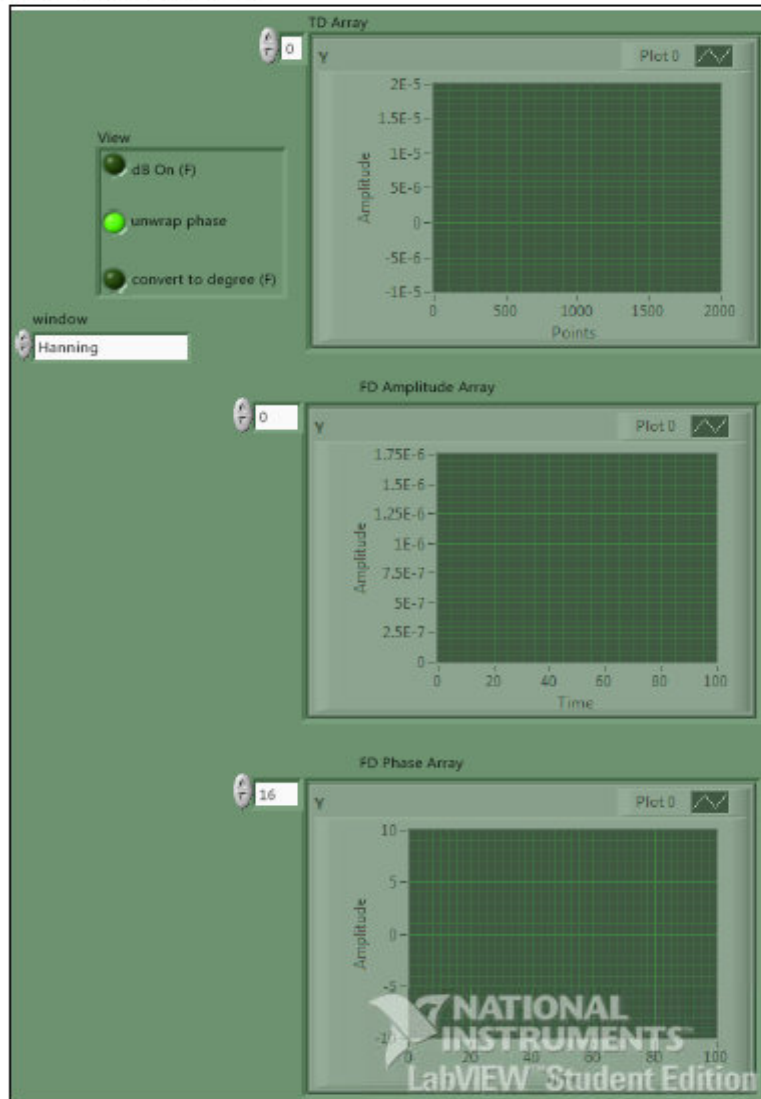
FFT single.vi
C:\Program Files\National Instruments\LabVIEW 8.2\user.lib\FFT single.vi

NI_AALPro.lvlib:windowTd.ctl
C:\Program Files\National Instruments\LabVIEW 8.2\vi.lib\Analysis\4window.llb\windowTd.ctl

126

Student Edition
FFT single.vi
C:\Program Files\National Instruments\LabVIEW 8.2\user.lib\FFT single.vi
Last modified on 4/29/2008 at 10:21 PM
Printed on 7/15/2008 at 12:59 AM

Page 1   FFT
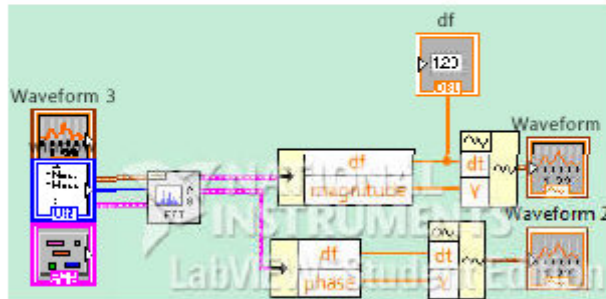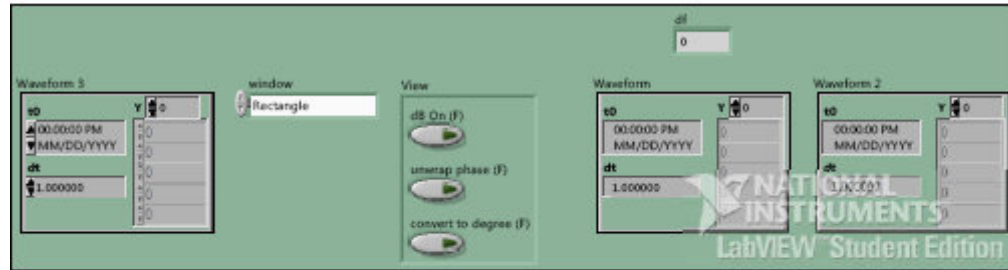
NI_MAPro.lvlib:FFT Spectrum (Mag-Phase) for 1 Chan.vi
C:\Program Files\National Instruments\LabVIEW 8.2\vi.lib\measure\maspectr.llb\FFT Spectrum (Mag-Phase) for 1 Chan.vi

NI_AALPro.lvlib:windowTd.ctl
C:\Program Files\National Instruments\LabVIEW 8.2\vi.lib\Analysis\4window.llb\windowTd.ctl

NI_MAPro.lvlib:FFT Spectrum (Mag-Phase).vi
C:\Program Files\National Instruments\LabVIEW 8.2\vi.lib\Measure\maspectr.llb\FFT Spectrum (Mag-Phase).vi

Student Edition
Profile Calc.vi
C:\Program Files\National Instruments\LabVIEW 8.2\user.lib\Profile Calc.vi
Last modified on 7/3/2008 at 4:33 PM
Printed on 7/15/2008 at 1:03 AM

Page 1

128

Profile Calc.vi
C:\Program Files\National Instruments\LabVIEW 8.2\user.lib\Profile Calc.vi
Last modified on 7/3/2008 at 4:33 PM
Printed on 7/15/2008 at 1:03 AM
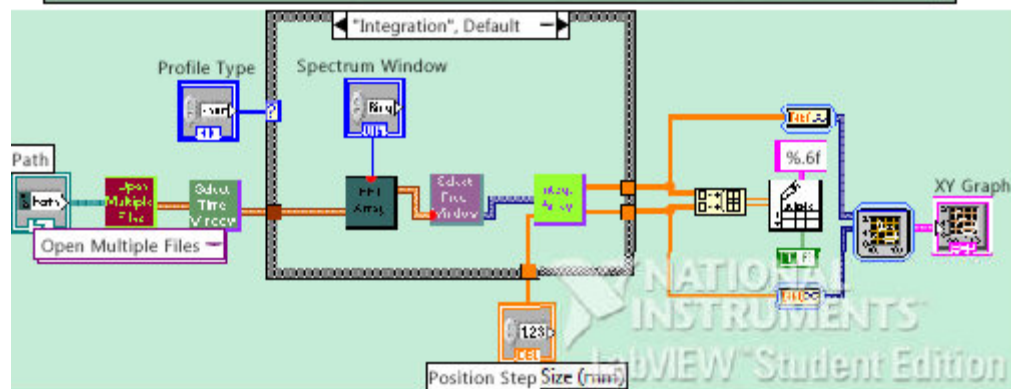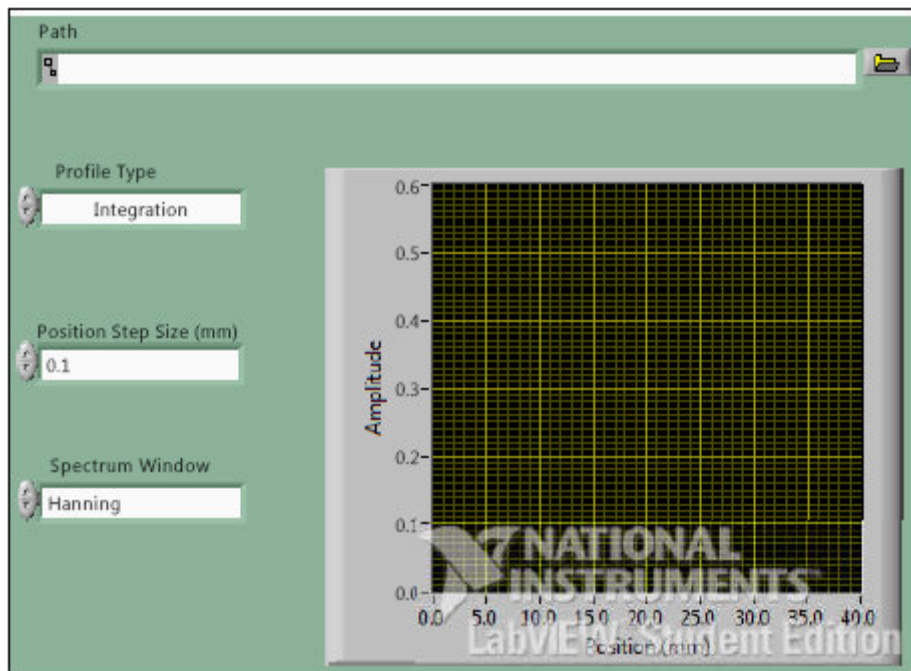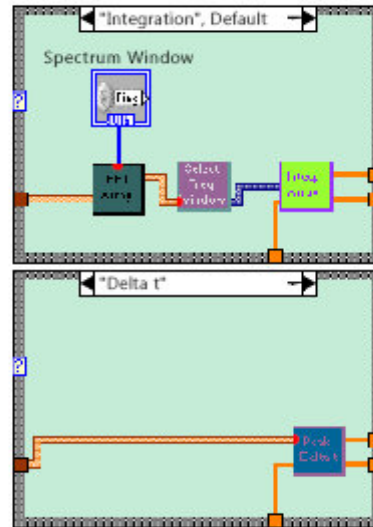
Open Multiple Files (Poly).vi
C:\Program Files\National Instruments\LabVIEW 8.2\user.lib\Open Multiple Files (Poly).vi

Open Multiple Files.vi
C:\Program Files\National Instruments\LabVIEW 8.2\user.lib\Open Multiple Files.vi

Select Time Window.vi
C:\Program Files\National Instruments\LabVIEW 8.2\user.lib\Select Time Window.vi

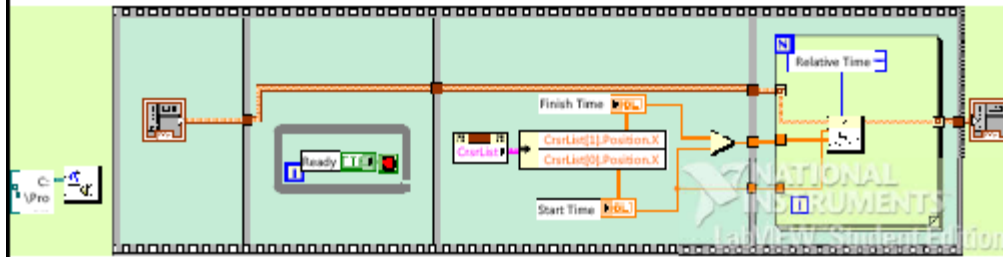**Select Time Window Array.vi**
C:\Program Files\National Instruments\LabVIEW 8.2\user.lib\Select Time Window Array.vi

FD Waveform Array.vi
C:\Program Files\National Instruments\LabVIEW 8.2\user.lib\FD Waveform Array.vi

Convert to Dynamic Data2
Convert to Dynamic Data
Converts numeric, Boolean, waveform and array data types to the dynamic data type for use with Express VIs.

Multi Peak Detect.vi
C:\Program Files\National Instruments\LabVIEW 8.2\user.lib\Multi Peak Detect.vi

Integrate 1D Array.vi
C:\Program Files\National Instruments\LabVIEW 8.2\user.lib\Integrate 1D Array.vi

Select Frequency Window.vi
C:\Program Files\National Instruments\LabVIEW 8.2\user.lib\Select Frequency Window.vi

Profile Calc.vi
C:\Program Files\National Instruments\LabVIEW 8.2\user.lib\Profile Calc.vi
Last modified on 7/3/2008 at 4:33 PM
Printed on 7/15/2008 at 1:03 AM

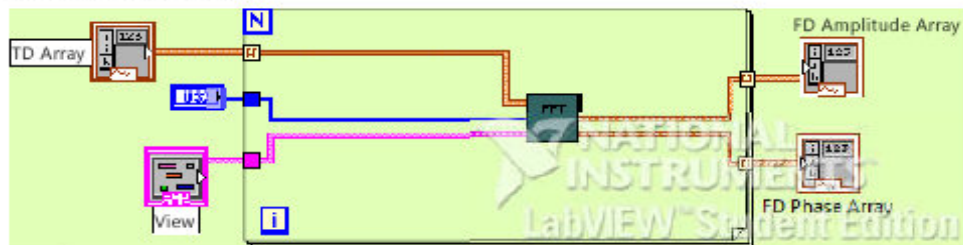**Write To Spreadsheet File (DBL).vi**
C:\Program Files\National Instruments\LabVIEW 8.2\vi.lib\Utility\file.llb\Write To Spreadsheet File (DBL).vi

Write To Spreadsheet File.vi
C:\Program Files\National Instruments\LabVIEW 8.2\vi.lib\Utility\file.llb\Write To Spreadsheet File.vi

Convert to Dynamic Data
Convert to Dynamic Data
Converts numeric, Boolean, waveform and array data types to the dynamic data type for use with Express VIs.

Build XY Graph
Build XY Graph
formats the data displayed on an X-Y Graph.

Student Edition
Multi Peak Detect.vi
C:\Program Files\National Instruments\LabVIEW 8.2\user.lib\Multi Peak Detect.vi
Last modified on 6/13/2008 at 6:56 PM
Printed on 7/15/2008 at 1:03 AM

Page 1

Convert from Dynamic Data

Convert from Dynamic Data

Converts the dynamic data type to numeric, Boolean, waveform, and array data types for use with other VIs and functions.

Student Edition
Multi Peak Detect.vi
C:\Program Files\National Instruments\LabVIEW 8.2\user.lib\Multi Peak Detect.vi
Last modified on 6/13/2008 at 6:56 PM
Printed on 7/15/2008 at 1:03 AM

Page 2
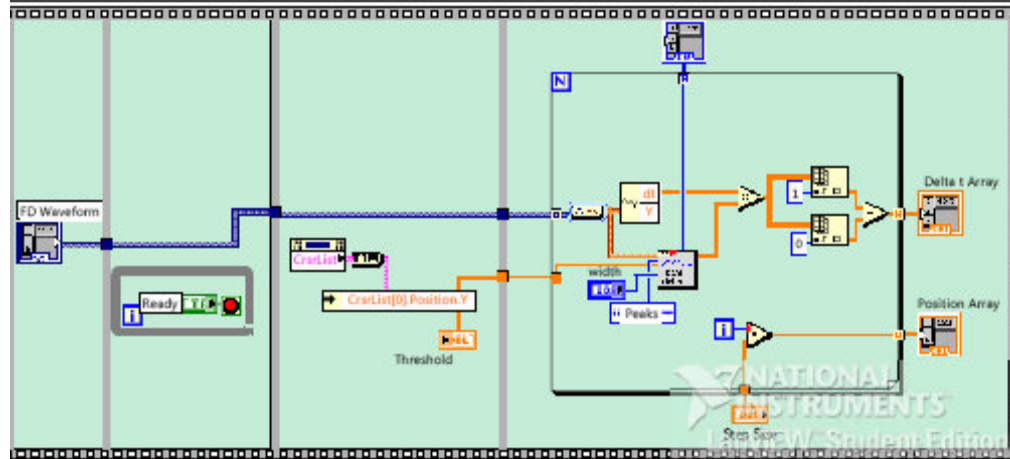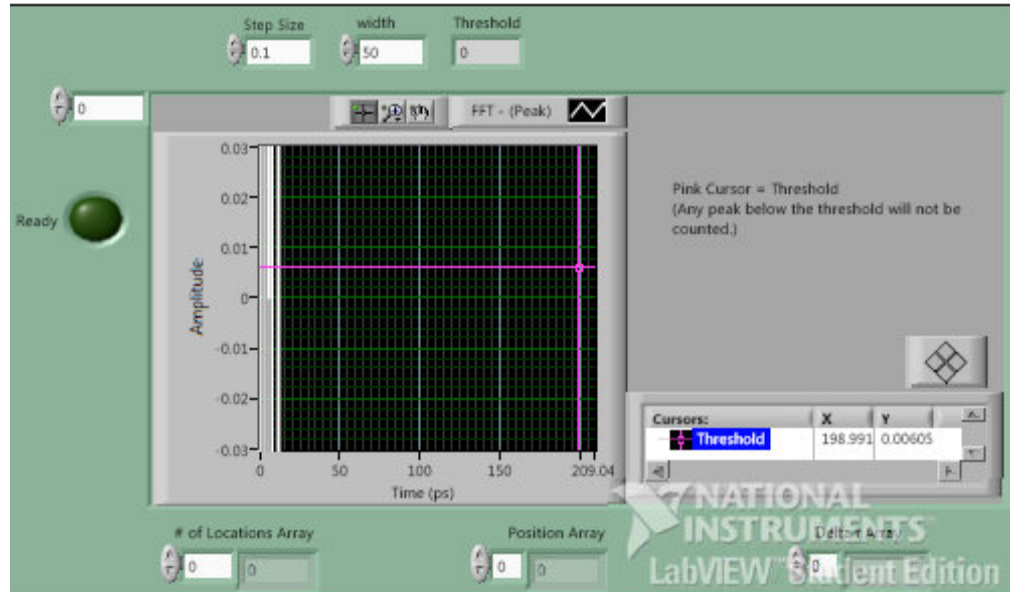
NI_MAPro.lvlib:Waveform Peak Detection for 1 Chan.vi

C:\Program Files\National Instruments\LabVIEW 8.2\vi.lib\measure\mamon.llb\Waveform Peak Detection for 1 Chan.vi

NI_MAPro.lvlib:Waveform Peak Detection.vi

C:\Program Files\National Instruments\LabVIEW 8.2\vi.lib\measure\mamon.llb\Waveform Peak Detection.vi
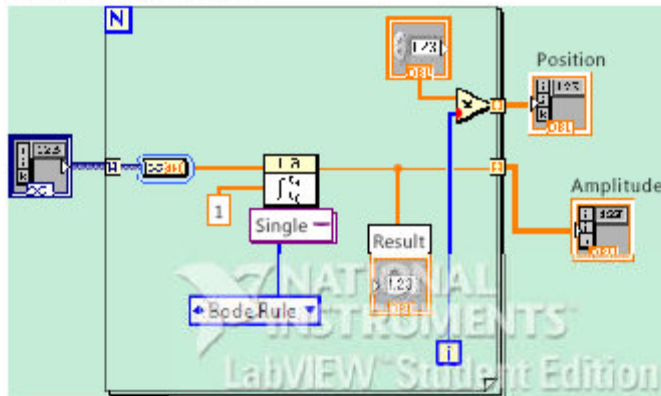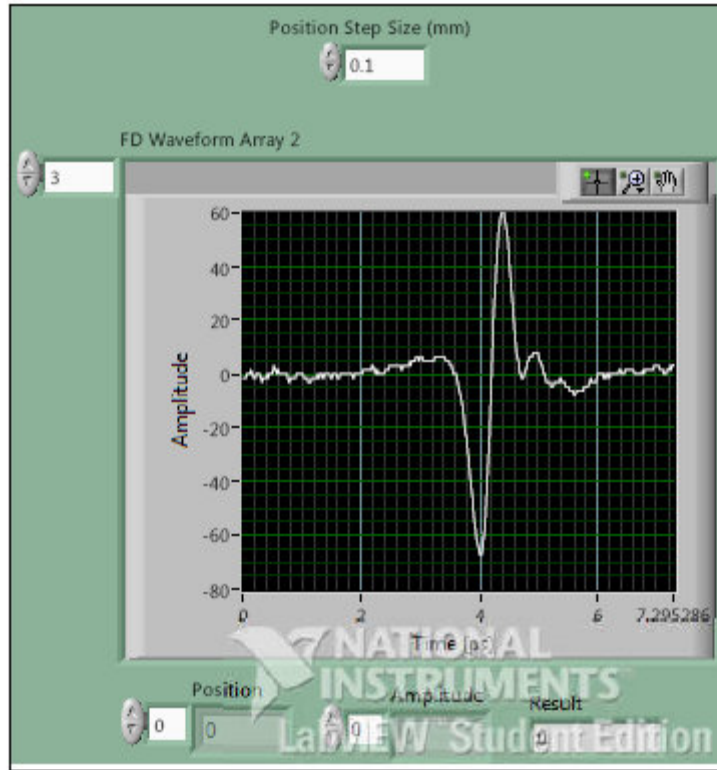
Student Edition
Integrate 1D Array.vi
C:\Program Files\National Instruments\LabVIEW 8.2\user.lib\Integrate 1D Array.vi
Last modified on 7/3/2008 at 4:19 PM
Printed on 7/15/2008 at 1:03 AM

Page 1

Position Step Size (mm)

0.1

FD Waveform Array 2

3

Student Edition
Integrate 1D Array.vi
C:\Program Files\National Instruments\LabVIEW 8.2\user.lib\Integrate 1D Array.vi
Last modified on 7/3/2008 at 4:19 PM
Printed on 7/15/2008 at 1:03 AM

Page 2

Convert from Dynamic Data
Convert from Dynamic Data
Converts the dynamic data type to numeric, Boolean, waveform, and array data types for use with other VIs and functions.

NI_AALPro.lvlib:1D Numeric Integration.vi
C:\Program Files\National Instruments\LabVIEW 8.2\vi.lib\Analysis\8numeric.llb\1D Numeric Integration.vi
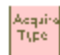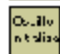
NI_AALPro.lvlib:Numeric Integration.vi
C:\Program Files\National Instruments\LabVIEW 8.2\vi.lib\Analysis\8numeric.llb\Numeric Integration.vi

ScanMama 2007.vi
I:\Sexy Scan Mama.llb\ScanMama 2007.vi
Last modified on 11/12/2007 at 8:43 PM
Printed on 7/15/2008 at 10:44 PM
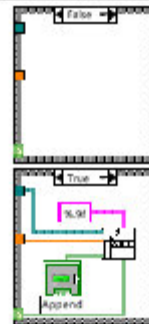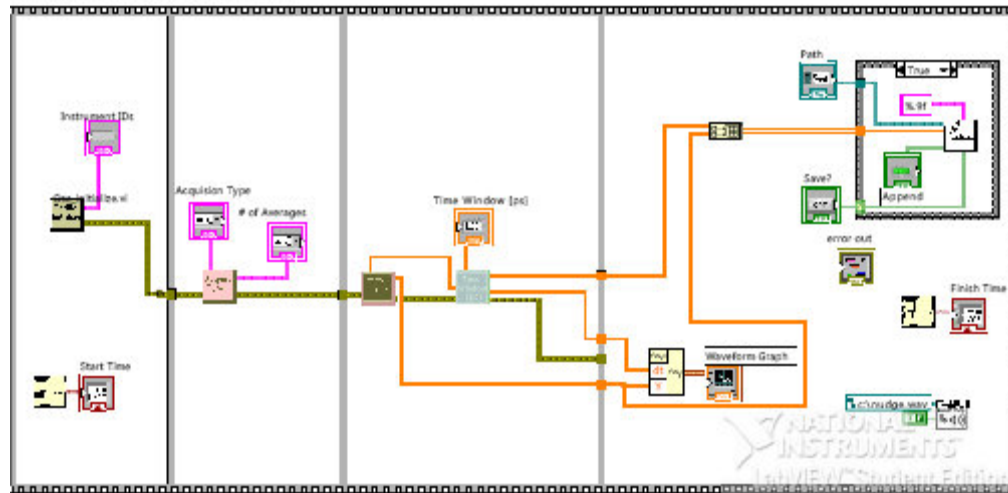
Write To Spreadsheet File.vi
C:\Program Files\National Instruments\LabVIEW 8.2\vi.lib\Utility\file.llb\Write To Spreadsheet File.vi

Write To Spreadsheet File (DBL).vi
C:\Program Files\National Instruments\LabVIEW 8.2\vi.lib\Utility\file.llb\Write To Spreadsheet File (DBL).vi

Snd Play Wave File.vi
C:\Program Files\National Instruments\LabVIEW 8.2\vi.lib\sound\lvsound.llb\Snd Play Wave File.vi

RS_time window.vi
I:\Sexy Scan Mama.llb\RS_time window.vi

Osc_acq_data.vi
I:\Sexy Scan Mama.llb\Osc_acq_data.vi

ScanMama 2007.vi
I:\Sexy Scan Mama.llb\ScanMama 2007.vi
Last modified on 11/12/2007 at 8:43 PM
Printed on 7/15/2008 at 10:44 PM

Osc_acq_type.vi
I:\Sexy Scan Mama.llb\Osc_acq_type.vi

Osc_initialize.vi
I:\Sexy Scan Mama.llb\Osc_initialize.vi

REFERENCES

[1] Cheville, R.A., Reiten, M.T., O'Hara, J. and Grischowsky, D.R., "THz time domain sensing and imaging," Proceedings of SPIE 5411 (2004) 196-206.

[2] Mittleman, D.M., Jacobsen, R.H., Nuss, M.C., "T-ray imaging," IEEE Selected Topics in Quantum Electronics 2 (1996) 679-692.

[3] Mittleman, D.M., Hunsche, S., Boivin, L. and Nuss, M, "T-ray tomography," Optics Letters, 22 (1997) 904-906.

[4] Cheville, R.A. and Grischowsky, D., "Time domain terahertz impulse ranging," Applied Physics Letters 67 (1995) 1960-1963.

[5] Reiten, M.T., Hess, L. and Cheville, R.A., "Nondestructive evaluation of ceramic materials using terahertz impulse ranging," Proceedings of SPIE 6179 (2006) 617905-1-8.

[6] National Materials Advisory Board/National Research Council, "Coatings for high-temperature structural materials," National Academy Press, Washington, DC (1996).

[7] Advisory Group for Aerospace Research and Development (AGARD/NATO), "Thermal barrier coatings," AGARD report 423, North Atlantic Treaty Organization (1997).

[8] Nicholds, E.F. and Tear, J.D., "Short Electric Waves," Physical Review 21 (19233) 587.

[9] Kimmitt, M.F., "Restrahlen to t-Rays – 100 years of terahertz radiation," Journal of Biological Physics 29 (2003) 77-83.

[10] Gebbie, H.A., Stone, N.W.B., and Findlay, F.D.A. "A stimulated emission source at 0.34 millimeter wavelength," Nature 202 (1964) 685.

[11] Yang, K.H., Richards, P.L., and Shen, Y.R., "Generation of far infrared radiation by picosecond light pulses in $LiNbO_3$," Applied Physics Letters19 (1971) 320-323.

[12] Auston, D.H., Glass, A.M. and LeFur, P., "Tunable far-infrared generation by difference frequency mixing of dye lasers in reduced (black) lithium niobate," Applied Physics Letters 23 (1973) 47–8.

[13] Hartwick, T.S., Hodges, D.T., Baker, D.H., and Foote F. B., "Far infrared imagery," Applied Optics 15 (1976) 1919–22.

[14] Auston, D.H., "Picosecond optoelectronic switching and gating in silicon," Applied Physics Letters 26 (1975) 101-103.

[15] Lee, C.H., "Picosecond electronic switching in GaAs," Applied Physics Letters 20 (1977) 84-6.

[16] Mourou, G., Stancampiano, C.V., Antonetti, A. and Orsag, A., "Picosecond microwave pulses generated with a sub-picosecond laser-driven semiconductor switch," Applied Physics Letters, 39 (1981) 295-7.

[17] Kawase, K., Ogawa, Y., Minamide, H., and Ito, H. "Terahertz parametric sources and imaging applications," Semiconductor Science and Technology 20 (2005) 258-265.

[18] Minamide, H., "Differential imaging using a THz-wave parametric oscillator," 2002 IEEE Tenth International Conference on Terahertz Electronics Proceedings (2002) 152-156.

[19] Shao-Wei, W., *et al.*, "Two-dimensional photonic crystal at THz frequencies constructed by metal-coated cylinders," Journal of Applied Physics 93(2003): p. 9401-3.

[20] Cook, D.J..j. and Hochstasser, R.M., "Intense terahertz pulses by four-wave rectification in air," Optics Letters 25 (2000) 1210-1212.

[21] Allen, S.J., Scott, J.S., Wanke, M.C., Maranowski, K., Gossard, A.C., Rodwell, M.J.W., Chow, D.H., "Terahertz dynamics in quantum structures: towards a fundamental terahertz oscillator," Terahertz Sources and Systems: Proceedings of the NATO Advanced Research Workshop (2001) 2-14.

[22] Ryzhii, V., M. Ryzhii, *et al.*. "Resonant terahertz photomixing in integrated high-electron-mobility transistor and quantum-well infrared photodetector device." Japanese Journal of Applied Physics--Part 1 45 (2006) 3648-51.

[23] Alekseev, K.N., "New approaches to THZ Bloch oscillator," Conference Digest of the 2004 Joint 29th International Conference on Infrared and Millimeter Waves and 12th International Conference on Terahertz Electronics (2004) 163-4.

[24] Robertazzi, R.P. and Buhrman, R.A., "Josephson terahertz local oscillator," IEEE Transactions on Magnetics 25 (1989) 1384-7.

[25] Kohler, R., *et al*. "Terahertz semiconductor heterostructure laser," Nature 417 (2002) 156-159.

[26] Belkin, M.A., Capasso, F., Xie, F., Belyanin, A., Fischer, M., Wittmann, A. and Faist, J., "Room temperature terahertz quantum cascade laser source based on intracavity difference-frequency generation." Applied Physics Letters 92 (2008) 201101.

[27] Schade, U., Holldack, K., Kuske, P., Wüstefeld, G., and Hübers, H.-W., "THz near-field imaging employing synchrotron radiation," Applied Physics Letters 84 (2004) 1422-1424.

[28] Schmuttenmaer, C., "Exploring dynamics in the far-infrared with terahertz spectroscopy," Chemical Review 104 (2004) 1759-1779.

[29] Nichols, E.F., "Heat rays of great wave length," Physical Review 4 (1897) 314.

[30] Kreisler, A.J. and Gaugue, A., "Recent progress in high-temperature superconductor bolometric detectors: from the mid-infrared to the far-infrared (THz) range," Superconductor Science and Technology 13 (2000) 1235-1245.

[31] Phillips, T.G., Keene, J., "Submillimeter astronomy [heterodyne spectroscopy]," *Proceedings of the IEEE*, 80 (1992) 1662-1678.

[32] Siegel, P., "Terahertz technology," IEEE Transactions on Microwave Theory and Techniques 50 (2002) 210-229.

[33] Mittleman, D.M., Jacobsen, R.H., Neelamani, R., Baraniuk, R.G., Nuss, M.C., "Gas sensing using terahertz time-domain spectroscopy," Applied Physics B 67 (1998) 379-390.

[34] Kawase, K., Ogawa, Y., Watanabe, Y. and Inoue, H., "Non-destructive terahertz imaging of illicit drugs using spectral fingerprint," Optics Express, 11 (2003) 2549-2554

[35] Mittleman, D.M., Jacobsen, R.H., Nuss, M.C., "T-ray imaging," IEEE Selected Topics in Quantum Electronics 2 (1995) 679-92.

[36] Thomas, G.H., "Overview of nondestructive evaluation technologies," Proceedings in SPIE 2455 (2005) 6-9.

[37] Ellingson, W.A., Visher, R.J., Lipanovich, R.S., and Deemer, C.M., "Optical NDE methods for ceramic thermal barrier coatings," Materials Evaluation Nov (2005).

[38] Maev, R. G., Green Jr., R. E., and Siddiolo, A. M., "Review of Advanced Acoustical Imaging Techniques for Nondestructive Evaluation of Art Objects," Research in Nondestructive Evaluation 17 (2006) 191–204.

[39] Gurov, I., Karpets, A., Margariants, N., and Vorobeva, E.,"Full-field high-speed optical coherence tomography system for evaluating multilayer and random tissues," Proceeding of SPIE 6618 (2007) 661807+8.

[40] Fontana, R., Bellini, M., Corsi, C., Mastroianni, M., Materazzi, M., Pezzati, L, and Tortora, A., "Optical coherence diagnostics for painting conservation," Proceedings of SPIE 6618 (2007) 661808+7.

[41] Rao, D.V., Hubbell, J.H., Zeniyah, T., Akastuda, T., Caesario, R., Breinetti, A, and Gigante, G.E., "Computed tomographyic imaging using tube source of x-rays – interior properties of the materials," Proceedings of SPIE 4503 (2002) 62-70.

[42] Uhd Jepsen, P., Jacobsen, R.H., Keiding, S.R., "Generation and detection of terahertz pulses from biased semiconductor antennas," J. Optical Society of America B 13 (1996) 2424-2433.

[43] Rudd, J.V., Zimdars, D., and Warmuth, M., "Compact, fiber-pigtailed, THz imaging system," Proceedings of SPIE: In Commercial and Biomedical Applications of Ultrafast Lasers II 3934 (2000) 27-35.

[44] Tani, Mashikio, Matsuura, S., Sakai, K., and Nakashima, S., "Emission characteristics of photoconductive antennas based on low-temperature grown GaAs and semi-insulating GaAs," Applied Optics 36 (1997) 7853-7859.

[45] Darrow, J.T., Zhang, X.C., Auston, D.H., "Saturation properties of large-aperture photoconducting antennas," IEEE Journal of Quantum Electronics 28 (1992) 1607-1615.

[46] Taylor, A.J., Benicewicz, P.K., Young, S.M., "Modeling of femtosecond electromagnetic pulses from large-aperture photoconductors," Optics Letters 18 (1993) 1340-1342.

[47] Piao, Z., Tani, M., Sakai, K., "Carrier dynamics and terahertz radiation in photoconductive antennas," Japanese Journal of Applied Physics 39 (2000) 96-100.

[48] Tani, M., Herrmann, M. and Sakai, K., "Generation and detection of terahertz pulsed radiation with photoconductive antennas and its applications to imaging," Measurement Science and Technology 83 (2002) 1739-1745.

[49] Auston, D.H., Cheung, K.P., Smith, P.R., "Picosecond photoconducting Hertzian dipoles," Applied Physics Letters 45 (1984) 284-286.

[50] Bethe, H.A., "Theory of Diffraction by Small Holes", Physical Review 66, 163-82.

[51] Xu, J.Z. and Zhang, X.C., "Optical rectification in an area with a diameter comparable to or smaller than the center wavelength of terahertz radiation," Optics Letters 27 (2002) 1067-1069.

[52] Dreyhaupt, A., Winnerl, S., Dekorsy, T, and Helm, M., "High-intensity terahertz radiation from a microstructured large-area photoconductor," Applied Physics Letters 86 (2005) 121114

[53] Smith, F.A., Le, H.Q., Dieadiuk, V., Hollis, M.A., Calawa, A.R., Gupta, S., Frankel, M, Dykaar, D.R., Mourou, G.A., Hsiang, T.Y., "Picosecond GaAs-based photoconductive optoelectronic detectors," Applied Physics Letters 54 (1989) 890-892.

[54] Valdmanis, J.A. and Mourou, G."Electro-optic sampling: testing picosecond electronics. II. Applications," Laser Focus/Electro-Optics, 22 (1986) 96-106.

[55] Goodman, J. W., Introduction of Fourier Optics, McGraw-Hill International Editions (1996) Ch. 2.

[56] Zimdars, D., "High speed terahertz reflection imaging," Progress in Biomedical Optics and Imaging - Proceedings of SPIE, 5692, Advanced Biomedical and Clinical Diagnostic Systems III. (2005) 255-259.

[57] Cheville, R.A. and Grischowsky, D., "Time domain terahertz impulse ranging," Applied Physics Letters 67 (1995) 1960-1963.

[58] Reiten, M.T., Hess, L. and Cheville, R.A., "Nondestructive evaluation of ceramic materials using terahertz impulse ranging," Proceedings of SPIE 6179 (2006) 617905-1-8.

[59] Zhong, H., Xu, J., Xie, X., Yuan, T., Reightler, R., Madaras, E., and Zhang, X.C, "Nondestructive defect identification with terahertz time-of-flight tomography," IEEE Sensors Journal 5 (2005) 203-208.

[60] Whitaker, J.F., Gao, F., Liu, Y, "Terahertz bandwidth pulses for coherent time-domain spectroscopy, " SPIE 2145 (1994) 168.

[61] van Exter, M., Fattinger, C., Grischowsky, D., "Terahertz time-domain spectroscopy of water vapor," Optics Letters 14 (1989) 1128-1130.
2005) S266-S280.

[62] Mittleman, D.M., Jacobsen, R.H., Neelamani, R., Baraniuk, R.G., Nuss, M.C., "Gas sensing using terahertz time-domain spectroscopy," Applied Physics B 67 (1998) 379-390.

[63] Beard, M.C., Turner, G.M., and Schuttemanaer, C.A., "THz spectroscopy," Journal of Physical Chemistry B 106 (2002) 7146-7158.

[64] Mittleman, D.M., Jacobsen, R.H., Nuss, M.C., "T-ray imaging," IEEE Selected Topics in Quantum Electronics 2 (1995) 679-92.

[65] Hu, B.B. and Nuss, M.C., "Imaging with terahertz waves," Optics Letters 20 (1995) 1716-1718.

[66] Chan, W.L., Diebel, J., Mittleman, D., "Imaging with terahertz radiation," Reports on Progress in Physics 70 (2007) 1325-1379.

[67] Federici, J.F., Schulkin, B., Huang, F., Gary, D., Barat, R., Oliveira, F., and Zimdars, D., "THz imaging and sensing for security applications—explosives, weapons and drugs," Semiconductor Science and Technology 20
[68] den Dekker, A.J., and van den Bos, A., "Resolution: a survey," Journal of the Optical Society of America A 14 (1997) 547.

[69] Shen, Y.C., Lo, T., Taday, P.F., Cole, B.E., Tribe, W.R., Kemp, M.C., Applied Physics Letters 86 (2006) 831-833.

[70] Yu, B.L., Yang, Y., Zeng, F., Xin, X., and Alfano, R.R., "Terahertz absorption spectrum of D_2O vapor," Optics Communications 258 (2006) 256-263.

[71]. Xin, X., Altan, H., Saint, A., Matten, D. and Alfano R. R., "Terahertz absorption spectrum of *para* and *ortho* water vapors at different humidities at room temperature, "Journal of Applied Physics 100 (2006) 094905+4.

[72] Libon, I.H., Hempel, M., Sietz, S., Hecker, N.E., Feldman, J., Hayd, A., Zundel, G., Mittleman, D., and Koch, M., "THz spectroscopy of polar liquids," SPIE Conference Proceedings 3617 (1999) 24-28.

[73] Zhang, C, Lee, K.S., Zhang, X.C., Wei, X., and Shen, Y.R., "Optical constants of ice 1h crystal at terahertz frequencies," Applied Physics Letters 79 (2001) 491-493.

[74] Ogawn, Y., Shindo, K, Mizuno, M., Otani, C., and Kawase, K., "Monitoring of water/ice state using millimeter waves for the agricultural field," 2005 Joint 29th International Conference on Infrared and Millimeter Waves and 12th International Conference on Terahertz Electronics (2004) 451-452.

[75] Mickan,S., Xu, J., Munch, J., Zhang, X.C., and Abbott, D., "The limit of spectral resolution in THz time-domain spectroscopy," Proceedings of SPIE 5277 (2004) 54-63.

[76] Tian, Z., Dudley, R., Jayes, L., and Hutton, R., "Evaluation of 3D spatial resolution for terahertz pulsed imaging systems," 2007 Joint 32nd International Conference on Infrared and Millimeter Waves and the 15th International Conference on Terahertz Electronics (2008) 1014-15.

[77] Roth, D., NDE Wave & Image Processor User's Manual, NASA (2008).

[78] Shon, C.-H., Chong, W.-Y., Jeon, S.-G., Kim, G.-J., Kim, J.-I., Jin, Y.-S., "High speed terahertz pulse imaging in reflection geometry and image quality enhancement by digital image-processing," International Journal of Millimeter Waves (2007).

[79] Hillery, R., ed. Coatings for high temperature structural materials, NRC Report, National Academy Press, 1996.

[80] Miller, R.A. , "Thermal Barrier Coatings for Aircraft Engines: History and Directions," J. Therm. Spray Technol. 6 (1997) 35.

[81] Wright, P.K. and Evans, A.G., "Mechanisms governing the performance of thermal barrier coatings," Current Opinion in Solid State & Material Science,"4 (1999) 255-265.

[82] Trunova, O., Beck, T., Herzog, R., Steinbrech, R.W. and Singheiser, L., "Damage mechanisms and lifetime behavior of plasma sprayed thermal barrier coating systems for gas turbines--Part I: Experiments", Surface and Coatings Technology, 202 (2008) 5027-5032.

[83] A. M. Karlsson, J. W. Hutchinson, A. G. Evans, The displacement of the thermally grown oxide in thermal barrier systems upon temperature cycling, Materials Science and Engineering A, 351 (2003)244-257.

[84] Tolpygo, V.K., Clarke, D.R., Murphy, K.S., "Oxidation-induced failure of EB-PVD thermal barrier coatings," Surface and Coating Technology 146-147 (2001) 124-131.

[85] Gell, M., Sridharan, S., Wen, M., and Eric H. Jordan, "Photoluminescence Piezospectroscopy: A Multi-Purpose Quality Control and NDI Technique for Thermal Barrier Coatings," International Journal of Applied Ceramic Technology 1 (2004)316-329.

[86] Song, S., Xiao, P., "An impedance spectroscopy study of high-temperature oxidation of thermal barrier coatings", Materials Science and Engineering B, 97 (2003) 46-53.

[87] Byeon, J.W., Jayaraj, B., Vishweswaraiah, S., Rhee, S., Desai, V.H., Sohn, Y.H., "Non-destructive evaluation of degradation in multi-layered thermal barrier coatings by electrochemical impedance spectroscopy", Materials Science and Engineering: A, 407 (2005) 213-225.

[88] Almond, D., Moghisi, M., Reiter, H., "The acoustic emission testing of plasma-sprayed coatings", Thin Solid Films, 108 (1983) 439-447.

[89] Eldridge, J.I., Spuckler, C.M. and Martin, R., "Monitoring delamination progression in thermal barrier coatings by mid-infrared reflectance image," International Journal of Ceramics Technology 3 (2006) 94-104.

[90] Bison, P.G., Marinetti, S., Grinzato, E., Vavilov, V., Cernuschic, F., and Robba, D., "Inspecting thermal barrier coatings by IR thermography," Proceedings of SPIE Vol. 5073 (2003) 318-328.

[91] Del Grande, N.K. and Durbin, P., "Mapping hidden aircrafts with dual-band infrared computed tomography," Proceeding of SPIE 2455 () 82-93.

[92] Christensen, J.R.,. Lipkin, D.M, Clarke, D.R., Murphy, K., "Nondestructive evaluation of the oxidation stresses through thermal barrier coatings using Cr31 piezospectroscopy" Appl. Phys. Lett. 69 (1996) 3745.

[93] Tolpygo, V.K., Clarke, D.R., Murphy, K.S., "Evaluation of interface degradation during cyclic oxidation of EB-PVD thermal barrier coatings and correlation with TGO luminescence," Surface & Coatings Technology 188–189 (2004) 62–70.

[94] Bolivar, P.H.; Brucherseifer, M.; Rivas, J.G.; Gonzalo, R.; Ederra, I.; Reynolds, A.L.; Holker, M.; de Maagt, P., "Measurement of the dielectric constant and loss tangent of high dielectric-constant materials at terahertz frequencies," *IEEE Transactions on Microwave Theory and Techniques*, 51 (2003) 1062-1066.

[95] Rutz, F., Koch, M., Micele, L., and de Portu, G., "Ceramic dielectric mirrors for the terahertz range," Applied Optics 45 (2006).8070-8073.

[96] Warnes, B.M., Punola, D.C., "Clean diffusion coatings by chemical vapor deposition," Surface & Coatings Technology, 94-95 (1997) 1.

[97] Nash, S., "Archaeological Tree-Ring Dating at the Millennium, "Journal of Archaeological Research, 10 (2002) 243-276.

[98] Bauch, J., Eckstein, D., "Dendrochronlogical Dating of Oak Panels of Dutch Seventeenth-Century Paintings," Studies in Conservation 15 (1970) 45-50.

[99] Grissino-Mayer, Henri, "Tree-ring Dating of Oak Panels from the Painting 'Gray-bearded Man Holding Shell'" Final Report published by the Laboratory of Tree-Ring Science, The University of Tennesee (2006).

[100] Kuniholm, P.I., ""Dendrochronology and Other Applications of Tree-ring Studies in Archeology," in The Handbook of Archeological Sciences, D.R. Brothwell and A.M. Pollard, eds, London, John Wiley & Sons, ltd (2001).

[101] Koch, M., Hunsche, S., Schuacher, P., Nuss, M., C., Feldmann, J., Fromm, J., "THz-Imaging: a new method for density mapping of wood," Wood Science and Technology 32 (1998) 421-427.

[102]Koch, M., "THz-Imaging: fundamentals and biological applications," Part of the EUROPTO Conference on Terahertz Spectroscopy and Applications II Munich, Germany . SPIE Vol. 3828 (1999) 202-208.

[103] Mittleman, D.,M. , Jacobsen, R.H., Nuss, M.C., "T-Ray Imaging," IEEE Journal of Selected Topics in Quantum Electronics, 2 (1996) 679.

[104] Thrane, I., Jacobsen, R.H., Uhd Jepsen, P., Keiding, S.R., "THz reflection spectroscopy of liquid water," Chemical Physics Letters, 240 (1995) 330-333.

[105] Reid, M. and Fedosejevs, R., "Terahertz birefringence and attenuation properties of wood and paper," Applied Optics, 45 (2006) 2766-2772.
[106] Knibbe, Bernhard, Personal Analysis System for Tree-ring Research 4, Instruction Manual, SCIEM, Chapter 14 (2004).

[107] Haneca, K, Wazny, T., Van Acker, J., Beeckman, H., "Provenancing Baltic timber for art historical objects: success and limitations," Journal of Archeological Science 32 (2005) 261-271

[108] Zimdars, D., "High speed terahertz reflection imaging," Progress in Biomedical Optics and Imaging - Proceedings of SPIE, 5692, Advanced Biomedical and Clinical Diagnostic Systems III. (2005) 255-259.

[109] Köhler, W., Panzer, M., Klotzach, U., Winner, S., Helm, M., Rutz, F., Jördens, C., Koch, M., Leitner, H. "Non-destructive Investigation of Paintings with THz-Radiation," European Conference of Non-Destructive Testing 2006 Proceedings (2006) Poster 181.

[110] Burrafato; G., Calabrese, M., Guieli, A.M., Troja, S.O., Ziccarello, A., "ColoRaman Project: Raman and fluorescence spectroscopy of oil, tempera and fresco paint pigments," Journal of Raman Spectroscopy 56 (2004) 879-886.

[111] Giakoumaki, A., Osticioli, I., Anglos,D., "Spectroscopic analysis using a hybrid LIB-Raman system," Applied Physics A 83 (2006) 537-542.

[112] Barilaro, D., Crupi, V., Majolio, D., Barone, G., Ponterio, R., "A detailed spectroscopic study of an Italian fresco," Journal of Applied Physics 97 (2005) 044907.

[113] Bruni, S., Cariati, F., Consolandi, L., Galli, A., Guglielmi, V., Ludwig, N., Milazzo, M., "Field and laboratory spectroscopic methods for the

identification of pigments in a northern Italian eleventh century fresco cycle," Applied Spectroscopy 56 (2002) 827-833.

[114] Baronti, S. Casini, Lotti, F., and Porcinal, "Multispectral imaging system for the mapping of pigments in works of art by use of principal-component analysis," Applied Optics, 37 (1998) 1299-1309.

[115] Pelagotti, A. Del Mastio, A., De Rosa, A., Piva, A., "Multispectral imaging of paintings," IEEE Signal Processing Magazine July (2008) 27-36.

[116] Casini, A., Lotti, F., Picollo, M., Stefani, L., and Buzzegoli, E., "Image spectroscopy mapping technique for non-invasive analysis of paintings", Studies in Conservation 44 (1999) 39-48.

[117] Underdrawings in Renaissance paintings, Art in the Making (2002) National Gallery Company limited, London, GB.

[118] Pieraccini, M., Mecatti, D., Luzi, G., Seracini, M., Pinelli, G. and Atzeni, C., "Non-contact intrawall penetrating radar for Heritage survey: the search of the 'Battle of Anghiari' by Leonardo da Vinci", NDT&E International 38 (2005) 151–157.

[119] Mittleman, D., Gupta, M., Neelamani, R., Baraniuk, R.G., Rudd, J.V., Koch, M., "Recent advances in terahertz imaging" Applied Physics B: Lasers and Optics 68 (1999) 1085-94.

[120] Sinopia Pigments, Inc., "Sinopia catalog" San Francisco, CA (2007).